Study of GLAD coatings for the optical smoothing of high-power lasers

Solène Bertet

Solène Bertet. Study of GLAD coatings for the optical smoothing of high-power lasers. Optics [physics.optics]. Sorbonne Université, 2025. English. ⟨NNT : 2025SORUS471⟩. ⟨tel-05579897⟩

HAL Id: tel-05579897
https://theses.hal.science/tel-05579897v1

Submitted on 3 Apr 2026

Sorbonne Université

Ecole doctorale de Physique et Chimie des Matériaux

Study of GLAD coatings for the optical smoothing of high-power lasers

Par Solène Bertet

Thèse de doctorat de Physique et Chimie des Matériaux

Dirigée par Bruno Gallas et Corinne Marcel

Soutenue publiquement le 12 décembre 2025

Devant un jury composé de :

David Babonneau	Directeur de Recherche, Université de Poitiers, Poitiers	Président
Pierre Bourdon	Directeur de Recherche, ONERA, Paris	Rapporteur
Aotmane En Naciri	Professeur, Université de Lorraine, Metz	Rapporteur
Marcela Mireles	Research Engineer, Rochester University, USA	Examinatrice
Tomas Tolenis	Associate Scientist, ELI Beamlines, Czech Republic	Examinateur
Bruno Gallas	Directeur de Recherche, Sorbonne Université, Paris	Directeur
Corinne Marcel	Ingénieure Chercheure, CEA, Tours	Directrice
Marine Chorel	Ingénieure Chercheure, CEA, Bordeaux	Invitée
Eric Lavastre	Ingénieur Chercheur, CEA, Bordeaux	Invité

Remerciements

Je tiens tout d'abord à remercier les membres du jury pour le temps et l'attention qu'ils ont consacrés à mes résultats.

Je tiens également à remercier mes cinq encadrants, Bruno, Marine, Éric, Corinne et Marcela. Vous avoir tous les 5 a été une véritable force pour moi !
Bruno, merci pour ta grande disponibilité malgré la distance, et pour l'exigence avec laquelle tu as suivi ce travail dans ses moindres détails. Merci de m'avoir poussée et encouragée quand il le fallait. J'ai beaucoup appris à tes côtés et j'ai surtout beaucoup apprécié travailler avec toi. Enfin, merci de m'avoir si bien accueillie à Paris. Marine et Éric, je suis contente que vous m'ayez fait confiance pour le stage, puis pour la thèse. C'est une belle expérience de travailler avec vous. Merci pour votre bienveillance et votre grande disponibilité. J'ai beaucoup apprécié nos discussions scientifiques (et non scientifiques) régulières. Corinne, merci pour la confiance que tu m'as accordée tout au long de cette thèse et pour ton suivi attentif. Finally, I would like to thank Marcela. Thank you for making my visits happen and I know that everything went well, mostly thanks to you. Thank you for your thorough supervision, even though we had 6 hours of jet lag. I learned a lot working with you, and I really enjoyed it. Thank you for everything!

I would like to thank the members of the LLE that I worked with in Rochester: Sara MacNally, Amy Rigatti, Daniel Sadowski, Brittany Hoffman, Stavros Demos, and Marek Stehlik. Thank you for your warm welcome, your availability, and the quality of our interactions, which made this collaboration both enriching and stimulating.
Je remercie également Estelle R., dont l'efficacité redoutable a grandement facilité la logistique de ma thèse et de mes nombreux déplacements. Je tiens à remercier chaleureusement l'ensemble des membres du laboratoire. L'ambiance joyeuse et d'entraide a, j'en suis certaine, beaucoup contribué à ma réussite. Je tiens à remercier tout particulièrement Olivier S. pour son aide précieuse dans la réalisation de mes travaux CréO, ainsi qu'Isabelle L. G. pour la logistique et la très bonne ambiance dans le bureau. Merci à Estelle L.G. et Martin pour les sessions pilates du mercredi. J'ai beaucoup apprécié ces moments et notamment nos traditionnels piques-niques. Enfin, un grand merci au comité des fêtes pour l'organisation de ces super événements !

Je remercie Thierry, Charles, Laurent, Sophie, Yvan et Isabelle L., pour leur aide précieuse dans la réalisation des caractérisations et pour l'accompagnement dans l'analyse et l'interprétation des données, cela m'a grandement aidée. Je remercie également mes collègues doctorants Arthur, Océane et Sylvain. Les conférences et les JDD étaient très agréables en votre compagnie. Merci encore, Arthur, pour ton temps et ta pédagogie ; nos conversations scientifiques m'ont beaucoup appris. Je remercie le CEA-CESTA pour les moyens et le soutien accordés et je remercie en particulier Jérôme N., Geneviève, Anne Pascale, Coralie, Erwan et Pascal pour leur aide durant cette thèse. Je remercie également les laboratoires avec lesquels j'ai travaillé : l'INSP, Le Ripault et PLACAMAT, qui m'ont si bien accueillie. Je tiens à remercier tout particulièrement Willy Daney de Marcillac, Olivier, Christophe, Christine Labrugère, Philippe Legros, Fabienne Ibalot et Jean-Paul Salvetat. Je remercie aussi Christelle Dublanche Tixier de m'avoir poussée à faire une thèse et de m'avoir encouragé tout au long de celle-ci.

Je tiens également à adresser un immense merci à ma famille : à ma maman, à mon papa, ainsi qu'à mes sœurs, Chloé et Émilie, qui sont aussi mes meilleures amies. Je vous remercie pour votre soutien indéfectible, sans lequel cette thèse n'aurait pu voir le jour. Je mesure la chance que j'ai de vous avoir à mes côtés. Ma maman, je te remercie pour ton écoute, tes conseils et ton aide au quotidien (coucou les covoits). Merci Matéo d'avoir tout fait pour que je sois dans les meilleures conditions pour réussir ma thèse. Merci d'avoir préparé tous mes gâteaux pour les évènements du comité des fêtes. Ils te remercient !! Merci d'avoir écouté, sans râler (ou presque), mes présentations pendant ces trois années. J'ai beaucoup de chance de t'avoir à mes côtés. Encore merci pour tout. Je remercie également mes amis : Roxane, Juliette, Margot, Carla, Ethel, Julianna, Maëlle, Paul, Élodie, Clément, Baptiste, Alexis B., Emmie, Vincent, Corentin C., Corentin N., Lylian, Florian, Quentin, Alexis M., Emma Z., Louise, Théo, Thibault et Julien H. Merci de m'avoir autant soutenue au quotidien. Merci de m'avoir rassurée quand j'en avais besoin (souvent), et surtout d'avoir su me faire rire dans les moments difficiles. Merci d'être venus si nombreux le jour de ma thèse, cela m'a beaucoup touchée et je suis ravie d'avoir partagé ce moment si important avec vous. Pour finir, je remercie Jul de m'avoir accompagnée en décorant magnifiquement ma porte de bureau, et également en tant que bande-son officielle de ma thèse.

Table of content

Chapter 1. Introduction

The objective of this chapter is to introduce the topic of this thesis in its global context.
The first part will present the high-power laser application, with the architecture of the Laser MégaJoule (LMJ) and the ignition confinement fusion experiments that led to the LMJ design. In a second part, the problematic of optical smoothing will be presented, with the solution studied for this thesis: the Polarization Smoothing (PS). This solution will be discussed in the complex environment of the LMJ. The latter would require a quarter-wave plate (QWP) component that could be fabricated with the GLancing Angle Deposition (GLAD) technique, operating at normal incidence in transmission at 351 nm either in ambient air or in contaminated vacuum. The choice of design and material will be developed in accordance with the needs of the application. Then, as required by the LMJ application, the laser damage resistance will be detailed. Lastly, a summary of the problematic will be provided and the plan of the manuscript will be listed.

1. The Laser MégaJoule

There are several high-power lasers worldwide, such as the Laser Megajoule (LMJ) in France, the National Ignition Facility (NIF) in the US, the Extreme Light Infrastructures in Czech Republic (ELI Beamlines), Hungary (ELI-ALPS), and Romania (ELI-NP), or the SG-III in China, etc. They all function differently, but they share the same goal of increasing laser energy levels to trigger laser-matter interaction experiments. Although my thesis was conducted in the LMJ framework, challenges encountered by all those facilities are often common issues.

More precisely, the aim of the LMJ is to experimentally study Inertial Confinement Fusion (ICF) to reproduce a fusion reaction as operating in the nuclear weapons or in the core of the sun. Nuclear fusion involves the collision and combination of two hydrogen isotopes: deuterium (D), which is composed of one proton, one neutron, and one electron; and tritium (T), which is composed of one proton, two neutrons, and one electron. Because the isotopes are lightweight, the reaction creates heavier atoms, such as helium, and releases the rest in energy with neutrons.

For the isotopes to combine, extreme temperatures and pressures must be provided. The energy is deposited by the 176 laser beams of the LMJ. The isotopes are in a centimeter-sized target (Figure 1). For the LMJ, this target is a cylindrical gold structure, called a hohlraum, which contains a capsule with the hydrogen isotopes. The isotopes are, in reality, in the form of a liquid combustible at -250 °C.

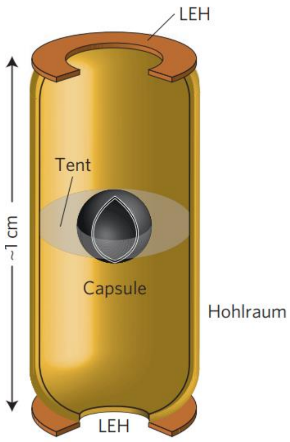

Figure 1. Target used for indirect drive internal confinement fusion [1]. LEH is for Laser Entrance Hole.

When the lasers are focused to the inner wall of the hohlraum through the Laser Entrance Holes (Figure 1 and Figure 2(a)), the wall produces X-rays (b) that heat and compress the capsule until implosion of the target (Figure 2). This implosion creates an extremely high temperature that enables the fusion of D-T. As the lasers are not focused directly to the D-T capsule, this process is called indirect drive inertial confinement fusion (ICF).

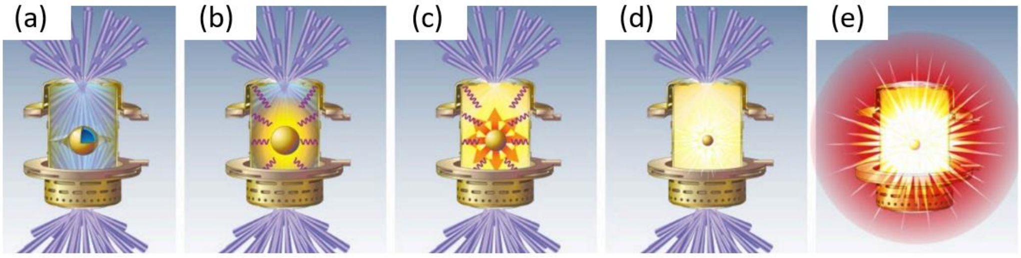

Figure 2. Steps happening in the target to form energy [2].

To enable these experiments, the laser energy must reach at least 1.3 MJ in the UltraViolet (UV). The design of the LMJ building was driven by specific requirement. The LMJ is a large building that is 300 meters long and 150 meters wide. It consists of one 10-meter-diameter experiment room in secondary vacuum and surrounded by four laser halls (Figure 3). Each of those laser halls contains five or six laser bundles, for a total of 22. Each laser bundle is equipped with eight laser beams, for a total of 176 beamlines.

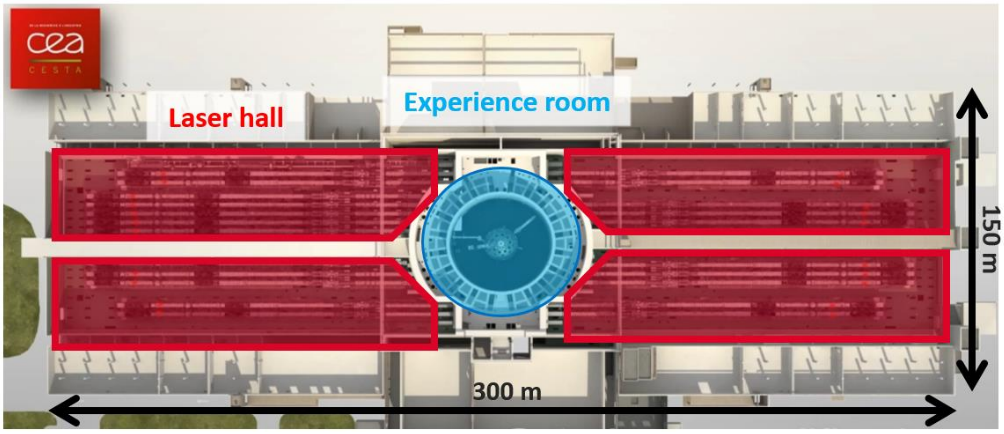

Figure 3. Top view of the LMJ with in red the laser halls and the experimental room in blue.

Figure 4 shows the architecture of one of the LMJ's laser beamline. In the front-end, a 3-ns InfraRed (IR) laser beam (1053 nm) is generated by a fiber source (1) which is temporally and spatially adjusted and amplified to 0.5 J by the pre-amplifier module (MPA) (2). The beam is then injected in the amplification section (3) with a square section of 40 x 40 cm². Increasing the size of the laser beam allows the components to withstand high laser energy. Indeed, one critical parameter for optical components for such high energy lasers is their capability to withstand high laser energy densities, designated as fluence.

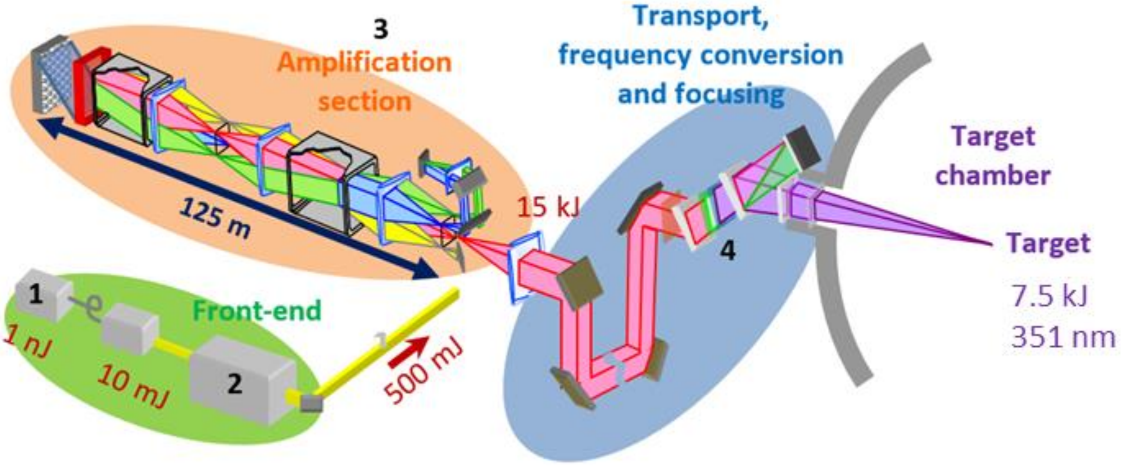

Figure 4. One laser beamline of the LMJ.

For example, the optical components, such as the polarizer presented in Figure 5, are large. The polarizers of the amplifier section measure 41.5 x 71 cm² because of the use at Brewster incidence.

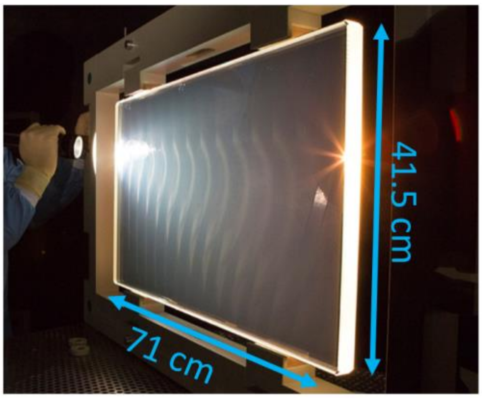

Figure 5. Photo of a polarizer from the amplifier section of the LMJ. It is illuminated from the side.

In the amplification section, the laser beam passes through amplifier slabs (phosphate glass doped with neodymium and pumped by flash lamps) four times to increase its energy up to 15,000 J. Then, mirrors transport and direct the beam to the frequency conversion section, where it is converted from IR to UV wavelength (4), from 1053 nm to 351 nm. The mirrors are also essential for ensuring the uniform distribution of laser beams all around the chamber. Finally, each laser beam is focused on the target with an energy of 7.5 kJ in the UV. However, the laser-matter interaction on the target can be reduced by laser-plasma instabilities [3]. To mitigate these instabilities, various techniques have been developed for smoothing the laser beams; one of these is the Polarization Smoothing (PS).

2. Optical smoothing for high-power laser

2.1. Polarization smoothing

High-energy-density laser beams require large focal spots (circular or elliptical) to provide homogeneous enlightenment to the target and ease the laser/target interaction. These large focal spots are created by phase plates that define the envelope of the focal spots. Inside this envelope, the focal spots exhibit speckle grains that result from the laser coherence and the random nature of the phase plate [4]. Figure 6 illustrates a typical speckle pattern of a high energy laser focal spot inside a super gaussian circular envelope. Speckle in the focused beam modulate laser intensity and bring heterogeneities of laser intensity around the target that can induce laser plasma instabilities and spoil energy from the target [5].

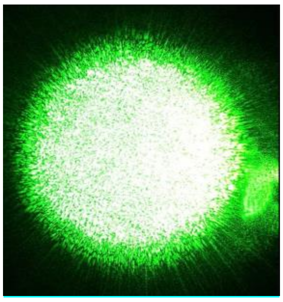

Figure 6. Illustration of the speckle grains of the laser in a circular supergaussian focal spot [6].

To overcome this issue, optical smoothing techniques could be implemented, as they allow us to manipulate the spatial and temporal coherence properties of the laser. In the LMJ, one technique is already used: Smoothing by Spectral Dispersion (SSD) [7], [8]. However, this technique doesn't allow to have a perfectly optically smoothed beam with low contrast. To bring an additional contrast reduction, another technique could be added to the LMJ. For this thesis work, Polarization Smoothing (PS) [9] - [11] is investigated. It consists of overlapping two incoherent speckle patterns. The incoherent speckle patterns are generated by two orthogonally polarized lights, since they don't interfere with each other. When the laser intensity patterns are added at the same time to the target, the contrast is lowered by an amount of √2. PS provides instantaneous smoothing, thanks to the independent nature of the two polarizations.

In summary, the goal of this technique is to overlap focal spots with two orthogonal polarization states, thereby reducing beam contrast within the focal point.

2.2. Utilization of GLAD quarter-wave plates as part of the smoothing strategy

Due to the engineering complexity of the LMJ, the smoothing component that changes the polarization can only be positioned at the end of the laser beamlines of the LMJ as presented in Figure 7. Specifically, after the frequency conversion from IR to UV, from 1053 nm to 351 nm; and after the 3ω focusing grating, which requires a linear polarization to operate.

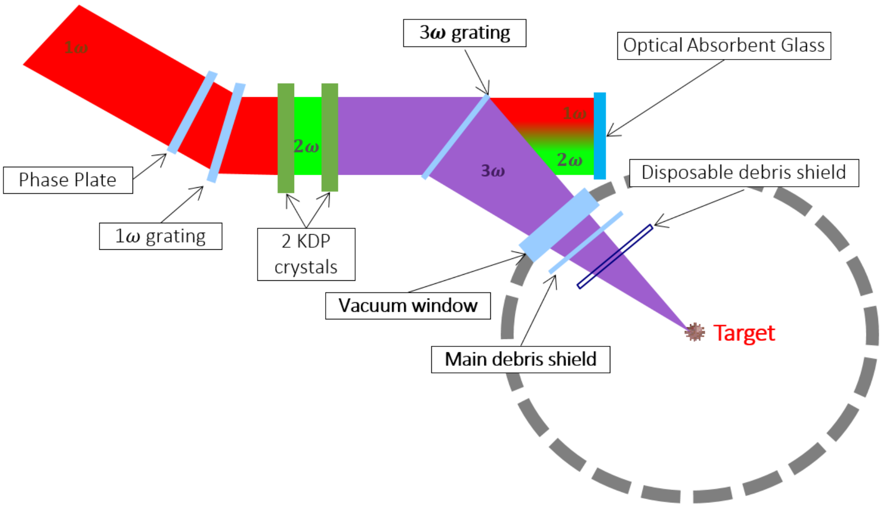

Figure 7. Schematic of the frequency conversion and focusing section

The precise position of the component has yet to be determined. The results of this thesis will be essential for ascertaining its location.

As just stated, the polarization is linear and vertical at the end of the laser beamlines and for PS, two orthogonal polarizations are required. In the case of the LMJ, the orthogonal polarizations could be two linear polarizations (vertical and horizontal, for instance) obtained with one half-wave plate placed on the path of one of the two beams, or two circular polarizations (right and left) thanks to quarter-wave plates on both beams.

For the contrast reduction to be efficient, the phase difference must be within the $\left[\frac{\pi}{2};\pi\right]$ range. Moreover, it has been demonstrated that using a circular polarization instead of a linear polarization reduces the Kerr effect in thick optics, such as the chamber window, which has a thickness of 34 mm [12]. The Kerr effect is a nonlinear effect that is characterized by a change in the refractive index during the propagation of a laser beam. In the case of an increase of the refractive index, it causes the beam to self-focus, which ultimately could result in laser-induced damage once the damage threshold is reached at the focal spot. The reduced Kerr effect, justify the preference for QWPs.

To summarize, the smoothing technique selected for this study is the use of a quarter-wave plate, capable of transforming the linear incident polarization into circular polarization. The two crossed polarizations are obtained by playing with the right and left circular polarizations in a quadruplet.

For this thesis, we considered inter-beam smoothing. However, exploring an intra-beam smoothing technique could be a viable option. This approach would require either a divided component that induces different phase differences [13] or a component with random retardance [14].

Additionally, the space constraints of the LMJ require the component to function in transmission and not in reflection.

There are several techniques for fabricating UV QWPs, including liquid crystals [15], [16], birefringent crystals [17], and transmission gratings [18]. In the LMJ facility, the dimensions of the optical components at the end of the beamlines are 40 x 40 cm² (at normal incidence). Fabricating a phase retarder of this size with a high laser damage resistance at 351 nm presents a significant challenge. For instance, transverse Raman scattering is observed with birefringent crystals [19], and, to date, quarter-wave transmission gratings have not been transposable for full-size laser components. This thesis will concentrate exclusively on GLAD coatings, which, in light of the following developments, appear to be a promising method.

In summary, the specifications for the GLAD coating are as follows: it is required to have a phase difference between $\left[\frac{\pi}{2};\pi\right]$ at 351 nm with a more efficient smoothing for a QWP (phase difference of $\frac{\pi}{2}$), a transmission higher than 99 %, and a laser damage resistance higher than 14 J/cm² for a pulse length of 3 ns.

2.3. Literature review of the fabrication of QWPs using the GLAD technique

With regard to state-of-the-art; GLAD QWPs can be fabricated using a variety of designs. Considering the potential use in optical smoothing for the LMJ, this literature review will focus exclusively on quarter-wave plates in transmission fabricated by e-beam GLAD.

First, they can be fabricated through a single tilted columnar layer. This approach has been proposed with a Ta_2O_5 QWP at 546 nm deposited at 70° [20] and a TiO_2 QWP at 465 nm deposited at 60° [21]. Additionally, a slanted structure deposited at an angle of 70°, made of Nb_2O_5, with a birefringence of 0.045 at 550 nm (33° of retardance phase) could be used as a QWP by adjusting the thickness of the coating [22]. Therefore, QWPs can be fabricated using a single tilted structure, however, the birefringence of the obliquely deposited film shows strong anisotropy, which is not favorable for the use of such coatings with normally incident light [20].

Alternatively, QWPs can be fabricated with a chevron-like design. This design has been explored for QWPs at 545 nm and 546 nm, with, as for example, a TiO_2 coating deposited at ± 60° [23] and a Ta_2O_5 film coated at ± 70° [20]. The Ta_2O_5 chevron-like design was compared to the film obtained with single columns deposited at 70°, and the chevron-like design exhibited a better spatial homogeneous retardance and transmission.
Additionally, an Al_2O_3 QWP at 351 nm designed with ± 75° chevron-like structures has also been fabricated [13]. It had uniform retardance and a laser damage resistance of 11.31 ± 0.31 J/cm^2 was measured at 351 nm, with a pulse length of 0.7 ns and a 1:1 testing protocol.

A comparison between tilted, chevron and helical designs made of TiO_2 and MgF_2 deposited at several angles (30°, 45°, 60°, 70°, 80°) has been done [21]. TiO_2 was determined to be a more suitable candidate than MgF_2 for the formation of retarder coatings due to its higher refractive index. Between the three structures deposited at 60°, TiO_2 exhibits the highest degree of birefringence when coated as a single tilted structure, followed by a chevron structure.

A more complex design can be used to fabricate QWPs. A series of MgO QWP coatings at 351 nm were designed for use in vacuum environments. These coatings were developed using the Serial BiDeposition (SBD) substrate motion, with angles ranging from 55° to 75° [24]. This method will be detailed in Chapter 2. For the samples deposited at 58°, 71° and 75°, the laser damage resistance at 351 nm, for 1:1 and N:1 tests, and a pulse length of approximatively 5 ns, with a small spot (300-µm $\frac{1}{e^2}$ diameter) was reported to be higher than 20 J/cm^2. SBD films are limited in their ability to produce QWPs due to the coalescence of the columns when exceeding a 400 nm thickness [25]. This can result in unwanted optical phenomena, such as scattering.

To overcome this issue, researchers, such as L. Grinevičiūtė *et al.* or Sara MacNally *et al.,* developed QWPs as multilayers composed of anisotropic GLAD layers and isotropic denser layers [25], [26]. Denser isotropic layers were also incorporated to enhance the mechanical strength of the multilayer structure.

L. Grinevičiūtė *et al.* worked on zero order wave plates at 355 nm, fabricated by e-beam GLAD and made of SiO_2 [25]. The samples consisted of alternating anisotropic layers, fabricated using the SBD substrate motion at ± 70°, and denser layers. The transmission was measured around 98.5 % and 99 % at 351 nm, with a retardance of 90°. Laser damage resistance; for 1-on-1 test at 355 nm; was measured at 11.5 J/cm^2 and 24.4 J/cm^2 using a laser beam of 220 µm diameter and 59 µm diameter, respectively.

In Sara MacNally *et al.* work, a silica coating QWP at 351 nm was described as an alternation of 10 layers, deposited at ± 73°, using SBD, and 10 isotropic denser layers, deposited at 0° [26]. On top of the 20-layer coating, a last SBD layer at ± 82° was incorporated to achieve an antireflective (AR) effect. The coating exhibited a transmission of 95.8 % and a reflectance of 3.9 % (including uncoated back surface of the substrate). The laser resistance was measured with a 400-µm diameter laser, with a 1-ns laser length at 351 nm; at 12.51 ± 0.51 J/cm^2 for a 1:1 testing protocol, and at 36.31 ± 3.74 J/cm^2 for a N:1 testing protocol (increasing fluence for multiple shots on one site). Retardance was measured and found uniform across the surface of 50-mm and 100-mm diameter samples.

In summary, from a design standpoint, GLAD enables the fabrication of QWPs in various ways. For some materials, such as Ta_2O_5 and Al_2O_3, the chevron structures seem to present, respectively, more transmission homogeneity and more retardance uniformity than the tilted structures. However, higher birefringence is created in TiO_2 using tilted structures rather than helical or zigzag ones. Ultimately, Al_20_3 chevron structures demonstrate notable laser resistance. SBD structures are ideal for fabricating high-birefringence films. However, it should be noted that the optical performance may decrease as the thickness of the layers increases. These layers can also be used in more complex designs made of smaller SBD anisotropic layers and isotropic layers. The structures exhibit a substantial Laser Induced Damage Threshold (LIDT), whether they are used alone or with isotropic denser layers. The multilayer coatings offer a uniform retardance distribution across the films and a high transmission. Adding isotropic denser layers between the anisotropic layers is an effective method for preserving optical properties. SBD offers the benefit of being less sensitive to the fabrication conditions because the structures are the average of multiple chevrons forming columns.

Two pairs of chevrons, on the other hand, are more sensitive. Additionally, studies have shown that nanostructured evaporated silica layers exhibit higher LIDT values due to increasing porosity during the evaporation process at glancing angles [27]. Porous structures are less restricted in density when material is expanding in volume due to the thermal effects. Therefore, the advantage of the multilayer QWP is that the E-field intensity peaks may be located in the highest resistant layers. **Given the various factors involved, the use of multilayers fabricated with SBD appears to be a promising solution for the QWPs in the LMJ.**

3. Review of materials allowing the fabrication of quarter-wave plates for the LMJ application

The commonly used coating materials in the high-power UV laser field are oxides and fluorides. Table 1, summarizes the refractive index and extinction coefficient of commonly used materials in high-power laser applications.

Table 1. Refractive index and extinction coefficient of the most commonly used materials in high-power laser applications

Material	Refractive index (n) at 351 nm	Extinction coefficient (k) at 351 nm	
Ta_2O_5	2.31	3×10^{-4}	[28]
TiO_2	2.58 - 3.18	$2.5 \times 10^{-2} – 6.2 \times 10^{-2}$	[29], [30]
MgF_2	1.39 - 1.43	$2.3 \times 10^{-5} – 1 \times 10^{-3}$	[31], [32]
MgO	1.75	1×10^{-7}	[33]
Nb_2O_5	2.75	2×10^{-2}	[34]
Al_2O_3	1.62 - 1.72	8×10^{-5} - Ø	[35], [36]
LaF_3	1.54 (400 nm) - 1.60	Ø - 1.2×10^{-3}	[31], [37]
SiO_2	1.49	9.7×10^{-5} - Ø	[34]

From a materials perspective, the required parameters are as follows:

- Materials with a high bulk refractive index, as this indicates larger phase delay differences in columnar structures [38].
- To avoid oscillations in the UV spectral transmittance, the average refractive index of the coating should be equivalent to that of the fused-silica substrate (1.49 at 351 nm) [24]. Due to the porosity of GLAD coatings, the ideal material requires a bulk refractive index between 1.6 and 1.8 [24].
- Materials with high laser resistance and no absorption.
- Materials that are stable in ambient air.

Based on Table 1, Ta_2O_5, TiO_2, or Nb_2O_5, have high refractive indices and may be suitable candidates. However, TiO_2 [39] and Nb_2O_5 are incompatible with UV due to their absorption band in that region. Furthermore, among the materials listed above, MgO, LaF_3, and Al_2O_3 are of particular interest, as their indices range from 1.6 to 1.9. However, fluorides are unstable in the ambient air. Finally, SiO_2 is known to be the most laser-resistant material.

Among the three selected materials (MgO, Al_2O_3 and SiO_2), **we made the choice of starting this project by studying the highest laser resistant material which is silica.**
As a reminder, the component's location remains to be determined. It could be before the vacuum window, which is in a controlled ambient air environment, or after the vacuum window, which is in a vacuum environment (Figure 7). Furthermore, contaminants have been detected in the surrounding environment near the LMJ target.

Among the contaminants, phthalates were most commonly found. They are often used as plasticizers to increase the elasticity, softness, and flexibility of plastics. Some usual uses are lacquers, plastics, safety glasses, rubber coating agents, molding powders [40]. Its origin is not entirely certain. However, we believe it could come from the seals used in the vacuum chamber, the lubricant used with the vacuum pump, the target itself, or potentially the wires used for characterization devices. Since they are not chemically bound to the polymer, they can migrate to the surface of the polymer matrix [41], [42]. Once they are on the surface, heat and/or void can facilitate their leaching into the environment [41] - [43], particularly into QWPs.

There are several types of phthalates, including dimethyl phthalate (DMP), di-n-butyl phthalate (DBP), and di-2-ethylhexyl phthalate (DEHP). We chose dimethyl phthalate (DMP) as the reference phthalate contaminant. DMP is an organic compound, with chemical formula $CH_{10}H_{10}O_4$ (Figure 8). It is an aromatic compound consisting of a benzene ring and two ester groups. In ambient air, DMP is a transparent liquid that is denser than water.

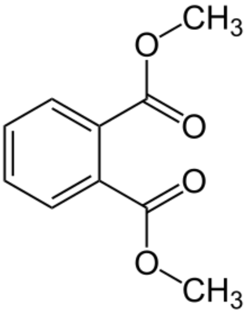

Figure 8. Chemical formula of dimethyl phthalate (DMP)

The presence of contamination in the target chamber, while it is in the same environment as the GLAD device, raises concerns about potential degradation of the optical performance. Moreover, silica is known to be sensitive to relative humidity (RH) [44] - [47] and to contaminations [48]. **For that reason, we chose to study another material in a second time. This material is alumina.** Its chemical properties indicate enhanced resistance to aging and environmental effects. Indeed, alumina is recognized for its chemical inertness [49] and alumina thin films are employed as humidity barriers [50] - [53].

4. Major problematic of laser induced damage resistance

The transparency of a material to a laser depends on its band gap. If the material has a higher band gap than the energy of the laser, the material is transparent to this photon. For instance, fused silica has a band gap of 8.8 eV, and the photon energy of the laser at 351 nm is 3.5 eV. However, elements (impurities, defects, etc.) can induce local energy levels in the band gap, thereby increasing the absorption of laser photons and potentially leading to laser damage [54]. Damage sites can occur on the entry side, within the sample, or on the exit side. For a fused silica substrate, in nanosecond regime, the damage sites occur on the back side of the component (the exit side of the laser) [55], [56].

Laser resistance depends on three parameters: the quality of the optical component [57], [58], the cleanliness of the environment [7], [8], and the quality of the beam, since hot spots can induce nonlinear effects, such as Kerr effects [61]. In our case of application, the quality of the optical component will be studied through the development of the GLAD coating. The cleanliness of the environment will be discussed in the particular case of chemical contamination. Finally, the quality of the beam is only brought up by the final application.

Coatings defects that can lower the LIDT can be intrinsic or extrinsic [62]. Intrinsic defects are defects from the film growth mechanism such as pores, cracks, incomplete stoichiometry, and columnar microstructure of multiple crystalline phases within the material. Extrinsic contaminants are typically associated with foreign defect seeds arising during the coating process or surface contamination resulting from incomplete substrate cleaning [62].

For this thesis, several elements can represent a challenge for the laser resistance of the QWPs films: defaults in the fabrication/microstructure, such as the non-stoichiometry, the presence of aggregates, or the non-robustness of the multilayer, etc. These elements can be studied by analyzing the internal structure of the coatings and their morphology. Additionally, the use of a porous coating in the contaminated vacuum of the LMJ could present a concern.

5. Problematic and plan of the manuscript

The LMJ requires smoothing the intensity profile of its 176 beams. Polarization smoothing is the considered optical smoothing technique in this present work. For that, circular crossed polarizations must be generated. The vertical linear polarization of the LMJ imposes the fabrication of QWPs. Among the techniques allowing the fabrication of QWPs, GLAD SBD was selected. This review of the context revealed several major challenges regarding the optical functions of the GLAD component, such as the homogeneity and obtaining the specified values of transmission and retardance. The material of the coating must ensure a stability over time, a non-environmental sensitivity, and a high laser resistance. The objective of the thesis was to assess the feasibility, in the future, of a full-scale GLAD coating that would ensure consistent optical performance for the optical smoothing of the LMJ laser beams.

This thesis mainly took place at CEA-CESTA near Bordeaux, France. However, some of the work was conducted at the Laboratory for Laser Energetics (LLE) in Rochester, USA, for samples fabrication and characterizations; at the Institut des NanoSciences de Paris (INSP) for optical modeling and characterizations; and at the CEA-Le Ripault near Tours, France, for contamination experiments.

Thanks to a collaboration with the Optical Manufacturing Group at LLE, which is managed by Amy Rigatti, I could work there three times. During the first two-week visit, the focus was on understanding the coating method and measuring the samples using various retardance characterization methods. The second visit, which was a month-long, focused on developing a new design with alumina. In collaboration with Sara MacNally and Marcela Mireles, we developed the design, and I measured the fabricated samples. The third visit lasted one month and was intended to accelerate the aging of the silica samples immediately after fabrication. This was achieved by exposing the samples to controlled conditions in a climate chamber. I created the aging plan and I tracked the samples for the month. The fabrication of all the samples was made possible thanks to Sara MacNally, Daniel Sadowski, Marcela Mireles and Amy Rigatti.

The manuscript is organized into five chapters, a final paragraph summarizing the conclusions brought up by this thesis work and presents the perspectives arising from those, and finally, the appendices.

This **Introduction** chapter has presented the context of the thesis, a review of the state of the art, and the organization of the manuscript.

Chapter 2 will explain the scientific concepts that are discussed throughout this manuscript. It will begin with the optical knowledge behind the anisotropy and its characterization techniques. In a second part, the GLAD Serial BiDeposition technique, that allows the formation of anisotropic coatings, is described. Then, a third and fourth part will review the characterization techniques of the laser damage resistance, the chemical composition, the morphology, and the transmission.

Chapter 3 will comprehensively study the silica QWPs in ambient air because silica has been identified as the most suitable material for the LMJ's specific application. To better understand the origin of the optical properties of the GLAD coatings, I thought it was important to study the elementary layers that make the multilayer QWP. Therefore, I asked the LLE for single layers and bilayers. This chapter will analyze the multilayer's composition profile and detail the silica matrix using IR spectroscopy. The following sections will study the relationship between microstructure and anisotropy using ellipsometry. Finally, this chapter will analyze the homogeneity, transmission, and laser damage resistance.

Chapter 4 will address the stability of the optical performance of GLAD components. First, it will examine stability in the presence of forced phthalate contamination in order to investigate the location of the components next to the LMJ target. Second, it will address the issue of stability in ambient air. Since GLAD devices are evolving over time, an accelerated aging method will be proposed. This method involves exposing the devices to a heated humidified environment in a climate chamber. Both cases will be studied in terms of their impact on optical performance and internal structure.

Finally, **Chapter 5** will present a new alumina design. First, the highest anisotropic single layer will be created depending on the coating angle. Then, a bilayer and a multilayer will be fabricated and analyzed. Lastly, the stability of the alumina will be discussed.

Chapter 2. Materials and methods

The purpose of this second chapter is to present the background knowledge used throughout this thesis.

First, the optical knowledge will be detailed, beginning with the definition of the polarization of light. To continue, refractive indices for isotropic materials and anisotropic ones will be explained including the index ellipsoid and the different types of anisotropy. The formalisms of Jones and Stokes, which describe the polarization and anisotropy of materials, will be detailed, along with the theory used to study the fabricated thin films. This first part will end with the two techniques used to characterize the optical anisotropy of the QWP samples. The second part will present the GLAD technique as the coating method for the fabrication of anisotropic materials, along with an overview of the serial bideposition process to increase the anisotropy. Lastly, a technical description of the fabrication of the coatings will be given. The third section will briefly review the testing method to assess the laser resistance. Finally, the fourth and last section will introduce complementary characterization techniques that allowed for a comprehensive understanding of the performances of the GLAD samples.

1. Review of the optical knowledge behind the anisotropy of the studied materials

1.1. Light and polarization

The Maxwell equations describe the basic principles of electromagnetics: the interactions between the electric charges, the electric current, the electric field and the magnetic field. In the absence of sources, the Maxwell equations can be cast in the 4 following equations:

Maxwell-Gauss	$\vec{\nabla} \cdot \vec{\mathrm{D}} = 0$
Maxwell-Thomson	$\vec{\nabla} \cdot \vec{\mathrm{B}} = 0$
Maxwell-Faraday	$\vec{\nabla} \times \vec{\mathrm{E}} = -\frac{\partial \vec{B}}{\partial \mathrm{t}}$
Maxwell-Ampère	$\vec{\nabla} \times \vec{\mathrm{H}} = \frac{\partial \vec{D}}{\partial t}$

With the additional constitutive relations $\vec{\mathrm{D}} = \varepsilon_r \varepsilon_o \, \vec{\mathrm{E}}$ and $\vec{\mathrm{B}} = \mu_r \mu_o \, \vec{\mathrm{H}}$.

ε_r is relative permittivity. ε_o is vacuum permittivity. μ_r is relative permeability. μ_o is vacuum permeability.

The harmonic solutions of the Maxwell equations can be used to describe light as an **electromagnetic (EM) wave** that propagates in a given direction (Figure 9). The EM wave contains an electric ($\vec{E}$) and a magnetic ($\vec{B}$) component that oscillate perpendicularly between them and the propagation direction, according to the Maxwell Gauss and Maxwell-Thomson relations. In a material, the constitutive relations contain the description of the effect of matter on light through the complex relative permittivity ε_r and the complex relative permeability μ_r.

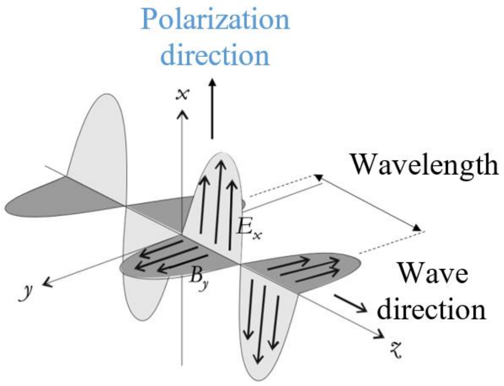

Figure 9. Light as an electromagnetic wave (Electric field E + Magnetic induction B) that propagates in the z direction [63].

At optical wavelengths, it is generally admitted that most materials are non-magnetic and μ_r = 1, therefore one considers only the electric field to describe the interaction of light with matter. The **polarization is a quantity that describes the oscillations and the direction of the electric vector $\vec{E}$**. In the direction of propagation, z, Equation (1) defines the electric field:

$$\mathrm{E(z,t) = E_0 e^{-i(\omega t - kz)}} \qquad (1)$$

t is the time, E_o is the amplitude of the wave, ω = 2πf is the angular frequency, k = $^{2\pi}/_{\lambda}$ is the wavevector's magnitude.

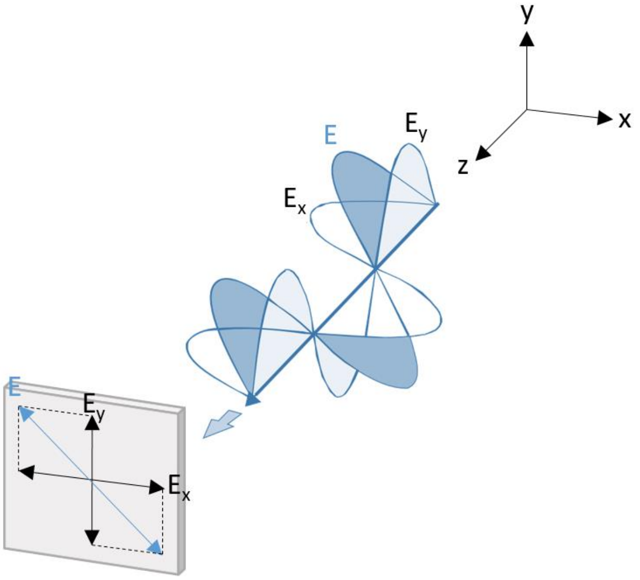

Figure 10. Two components of the electric field, E$_x$ and E$_y$ [64]. The geometric evolution of the total field (in blue) in the wave front defines the polarization (linear here).

For an EM wave propagating along z through time, the total electric field in the xy plane is the sum of two components (Figure 10), $E = E_x + E_y$ with:

$$E_x(\mathrm{z},\mathrm{t}) = E_{0\mathrm{x}}\mathrm{e}^{-\mathrm{i}(\omega\mathrm{t} - \mathrm{kz} + \varphi_\mathrm{x})} \quad (2)$$

$$E_y(\mathrm{z},\mathrm{t}) = E_{0\mathrm{y}}\mathrm{e}^{-\mathrm{i}(\omega\mathrm{t} - \mathrm{kz} + \varphi_\mathrm{y})} \quad (3)$$

E_{0x} and E_{0y} are the maximum amplitudes of the x and y components of the field and φ_y and φ_x are phases. By convention, the physical solutions are the real parts of the fields. The combination of the two components, i.e., the combination of Equations (2) and (3) yields Equation (4); which is the equation of an ellipse.

$$\left(\frac{E_x}{E_{0\mathrm{x}}}\right)^2 + \left(\frac{E_y^2}{E_{0\mathrm{y}}}\right) - 2\frac{E_x}{E_{0\mathrm{x}}}\frac{E_y}{E_{0\mathrm{y}}}\cos\varphi = \sin^2\varphi \quad (4)$$

With $\varphi = \varphi_y - \varphi_x$

Therefore, for **unspecified amplitudes and phase difference, the end of the $\vec{E}$ vector oscillates on an ellipse: the polarization is elliptical** (Table 2). However, for particular combinations of amplitude and phase, some specific polarization states are obtained (Table 2).

Table 2. Polarization state depending on the amplitudes and the phase difference.

$E_{ox} \neq E_{oy}$ and $\varphi \neq 0$ 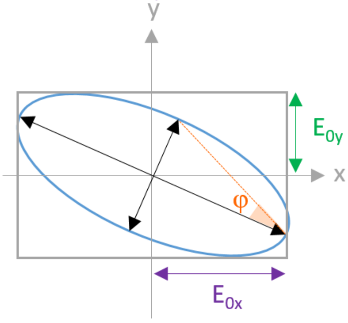	If $E_{ox} = 0$	
	If $E_{oy} = 0$	
	If $E_{ox} = E_{oy} = E_o$ and $\varphi = 0$ or $\varphi = \pi$	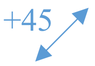 or 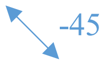
	If $E_{ox} = E_{oy} = E_o$ and $\varphi = \frac{\pi}{2}$ or $\varphi = -\frac{\pi}{2}$	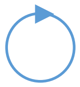 or 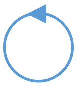

1.2. Refractive indices of anisotropic materials

In vacuum, light propagates in a straight direction at speed c (called celerity). In transparent, homogeneous and isotropic media, light propagates at a lower speed of $v = c/n$; where n is a dimensionless quantity called the refractive index which is related to the relative permittivity by $\mathrm{n} = \sqrt{\varepsilon_r}$. To put it differently, n is the ratio between the speed of light in air and the speed of light in a medium, the higher the refractive index the lower the speed of light in the medium. It can also be described as $\lambda = \lambda_0/n$; where λ_0 is the wavelength in vacuum. Thus, the refractive index n is characteristic of the medium. Over the years, researchers have built index libraries giving values of n for some of the most commonly used materials as for example the refractive index of air n = 1, of water n = 1.33 or of silica n = 1.49 at 351 nm.

For all materials, the refractive index is not constant and varies as a function of the wavelength: this is called dispersion. The dispersion can be approximated by dispersion relationships, a well-known one being the Cauchy equation:

$$\mathrm{n}(\lambda) = \mathrm{A} + \frac{B}{\lambda^2} + \frac{C}{\lambda^4} + \ldots \qquad (5)$$

Where A, B, C, etc. are coefficients that are specific to the material. However, in general the dispersion relation is more complicated, but for materials I will use, there are tabulated values found in libraries.

In an isotropic medium, the refractive index remains constant regardless of the light's polarization and direction. This is not the case in an anisotropic medium, where the refractive index depends on the polarization and the propagation direction of the light. This is called **birefringence** or **optical anisotropy**.

Let us see how this effect can be accounted for in the Maxwell equations.

In the case of optical anisotropy, the material can be oriented so that ε is a diagonal tensor that is function of directions along the x, y, z coordinate system:

$$\varepsilon = \varepsilon_0 \begin{bmatrix} \varepsilon_x & 0 & 0 \\ 0 & \varepsilon_y & 0 \\ 0 & 0 & \varepsilon_z \end{bmatrix} \tag{6}$$

For isotropic media, the tensor ε is constant ($\varepsilon_x = \varepsilon_y = \varepsilon_z$). For anisotropy, in the general case, all elements are different (biaxial anisotropy). Another way to relate the anisotropy to the directions is by using a geometric tool that describes a surface (see Eq. (7) [65]).

$$\frac{x^2}{n_x^2} + \frac{y^2}{n_y^2} + \frac{z^2}{n_z^2} = 1 \tag{7}$$

This geometric tool is called the **index ellipsoid** (Figure 11). It has three orthogonal axes: n_g, the longest axis; n_p, the shortest axis; and n_m, the third axis [66]. The index ellipsoid can be used to determine refractive indices, phase velocities, and polarization directions.

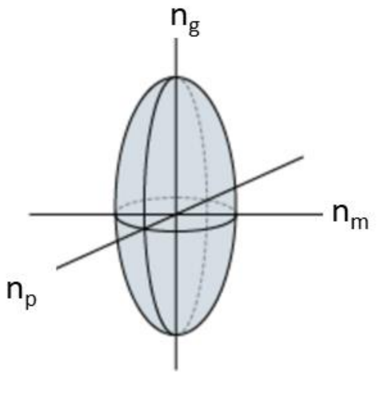

Figure 11. Index ellipsoid with its three orthogonal axes: n_g, n_m, and n_p [67].

In the n_g-n_p section, two cyclic sections with n_m as a radius can be drawn while rotating around n_m [67]. The axes perpendicular to these sections are called optical axes. A crystal with two cyclic sections, and thus two optical axes, is called a biaxial crystal (Figure 12). These axes are called the fast axis and the slow axis. The crystal has three principal axes: n_g, n_m, and n_p.

If the acute bisector of the optical axes is n_g, the ellipsoid is positive biaxial, as illustrated here. If the acute bisector of the optical axes is n_p, the ellipsoid is negative biaxial.

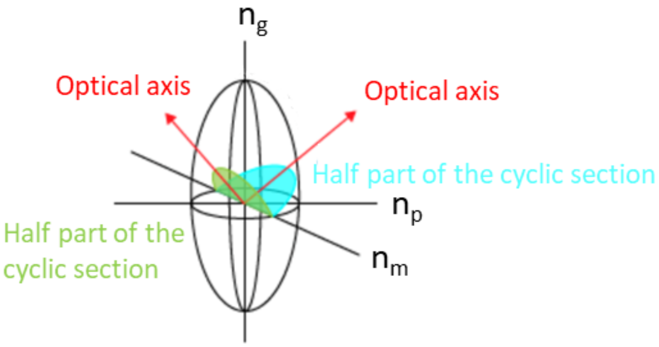

Figure 12. Biaxial crystal with two circular sections (green and blue) and two optical axes [67].

For a crystal with two equal indices ($n_p = n_m$), there is only one circular section, and therefore, one optical axis. This type of crystal is called uniaxial. The optical axis is also the axis of revolution of the ellipsoid. The crystal has two principal axes, n_p (small index, high speed) and n_g (big index, low speed), which are also called ordinary ($n_p = n_o$) and extraordinary ($n_g = n_e$) indices. If $n_e < n_o$, the ellipsoid is positive uniaxial; if $n_e > n_o$, the ellipsoid is negative uniaxial.

The refractive indices for the two principal polarization states can be determined by the intersection of the plane of the incident wave plate (k) and the index ellipsoid (Figure 13).

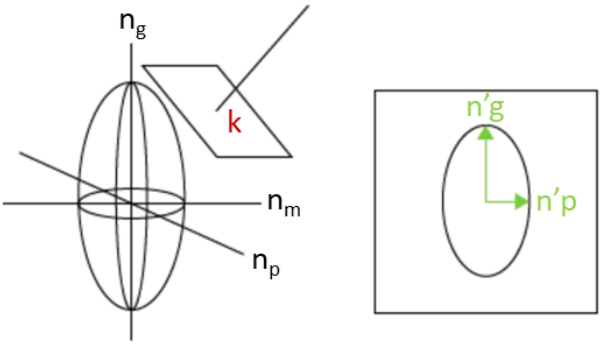

Figure 13. Intersection of the plane of the incident wave plate (k) and the index ellipsoid [67].

An ellipse can be drawn in the intersection plane (Figure 13) [67]. It has two major axes, n'_g and n'_p, which are the projections of the ellipsoid axes. The lengths of the semiaxes of the ellipsoid section are proportional to the refractive indices. The polarization directions coincide with the directions of these two axes [65]. For uniaxial and biaxial crystals, $n'_p \neq n'_g$, except when the section is cyclic (one for uniaxial and two for biaxial).

For a uniaxial material, if the wave is propagating parallel to the optical axis, there is no birefringence because the index experienced by the wave (n_o) is independent from its polarization. On the contrary, if the incident wave has an angle, the wave will split into two waves: the wave with linear polarization perpendicular to the optical axis will experience the ordinary refractive index n_o (and will keep the same direction) while the light polarized parallel to the optical axis will experience an extraordinary refractive index n_e. The ordinary wave and the extraordinary wave are orthogonal and have a different velocity because of the difference of index (n_o and n_e). Birefringence is the difference between those two indices, $\Delta n = n_e - n_o$. For a biaxial material, it is the same principle with the difference that the ordinary ray will be related to two indices.

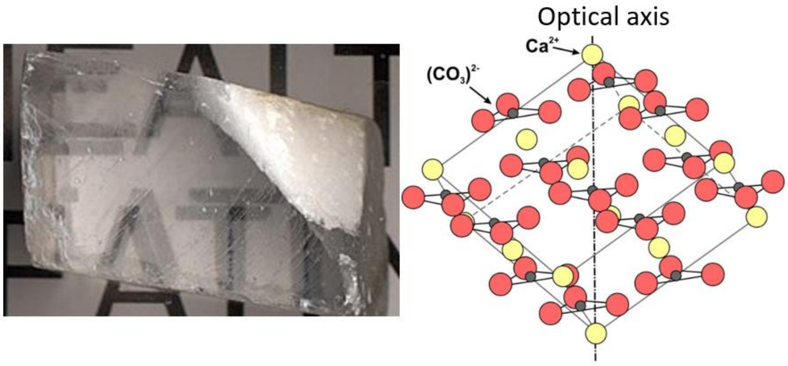

(a) (b)

Figure 14. (a) Natural birefringence of calcite as seen from a crystal place on top of printed letters [68] and (b) crystalline arrangement of the calcite unit cell [69].

Figure 14 is an example of calcite ($CaCO_3$) which is a natural birefringent material where the crystalline anisotropy results in uniaxial birefringence. When an incident beam enters the crystal with an angle different from the optical axis, the beam will split into two beams with perpendicular polarization that have different velocities [70] as illustrated by the double image seen on Figure 14(a). This phenomenon happens because of the crystallographic arrangement of calcite (Figure 14(b)) with an anisotropic unit cell effectively containing in one direction a higher density of atoms than in the others.

1.3. Jones and Stokes formalisms to describe the polarization and the behavior of anisotropic materials

Several formalisms exist to describe the polarization state, such as the Jones vector and Stokes vector.

By removing the common phase term $e^{-i(wt-kz)}$ of Equations (2) and (3), the polarization can be noted in a vector as:

$$E = \begin{pmatrix} E_x \\ E_y \end{pmatrix} = \begin{pmatrix} E_{0x}\, e^{i\varphi_x} \\ E_{0y}\, e^{i\varphi_y} \end{pmatrix} \tag{8}$$

The obtained vector is called the Jones vector. When a beam propagates into an optical component, the incident polarization E will be modified and the output polarization will be called E'. If this optical component is a polarizer, the amplitudes can be changed, if this is a wave plate, the phase can be changed. Finally, if the optical element is a rotator, the polarization ellipse may be rotated. The effect of the polarizing component is expressed by a 2 x 2 matrix J, called the Jones matrix. The transition from E to E' by this component is done by matrix product:

$$E' = \begin{pmatrix} J_{xx} & J_{xy} \\ J_{yx} & J_{yy} \end{pmatrix} \begin{pmatrix} E_x \\ E_y \end{pmatrix} = J.E \tag{9}$$

When considering a combination of different optical components in series, described by different Jones matrix met in the order J_1, J_2...J_i, the output polarization will be calculated according to Eq. (9) by inserting $J = J_i. \ldots .J_2.J_1$.

It exists another way to express the polarization: the Stokes parameters for the polarization state and the **Mueller matrix (MM) for the characterization of the optical element** (a wave plate for example). Equation (10) presents the relation between the components of the electric field within the Jones' formalism and the four real-valued elements of the Stokes vector S.

$$S = \begin{pmatrix} S_0 \\ S_1 \\ S_2 \\ S_3 \end{pmatrix} = \begin{pmatrix} E_{0x}^2 + E_{0y}^2 \\ E_{0x}^2 - E_{0y}^2 \\ 2E_{0x}E_{0y}\cos\varphi \\ 2E_{0x}E_{0y}\sin\varphi \end{pmatrix} \tag{10}$$

and $S_0^2 = S_1^2 + S_2^2 + S_3^2$ for fully polarized light.

S_0 describes the total intensity of the beam, S_1 is the difference in intensity between linear vertical and linear horizontal polarizations, S_2 is the difference between linear +45/-45 polarizations, and S_3 is the difference between circular right/left polarizations. For partially polarized light $S_0^2 > S_1^2 + S_2^2 + S_3^2$, and for unpolarized light S = (1,0,0,0).

This underlines the strength of the Stokes formalism as it allows to describe the propagation of partially polarized light, when the Jones formalism can't. However, in my work, I will consider only fully polarized light and non-depolarizing optical elements. Table 3 summarizes all the Jones vectors and the Stokes vectors for the particular polarizations state.

Table 3. Polarization state expressed using the Jones vector and the Stokes vector.

	↔	↕	+45 ⤢	⤡ -45	↻	↺
Jones vector	$E = \begin{pmatrix}1\\0\end{pmatrix}$	$E = \begin{pmatrix}0\\1\end{pmatrix}$	$E = \frac{1}{\sqrt{2}}\begin{pmatrix}1\\1\end{pmatrix}$	$E = \frac{1}{\sqrt{2}}\begin{pmatrix}1\\-1\end{pmatrix}$	$E = \frac{1}{\sqrt{2}}\begin{pmatrix}1\\i\end{pmatrix}$	$E = \frac{1}{\sqrt{2}}\begin{pmatrix}1\\-i\end{pmatrix}$
Stokes vector	$S = \begin{pmatrix}1\\1\\0\\0\end{pmatrix}$	$S = \begin{pmatrix}1\\-1\\0\\0\end{pmatrix}$	$S = \begin{pmatrix}1\\0\\1\\0\end{pmatrix}$	$S = \begin{pmatrix}1\\0\\-1\\0\end{pmatrix}$	$S = \begin{pmatrix}1\\0\\0\\1\end{pmatrix}$	$S = \begin{pmatrix}1\\0\\0\\-1\end{pmatrix}$

On the same principle as the Jones vector and the Jones matrix, the output polarization state S' is the product of the input polarization and a 4 x 4 matrix called the Mueller matrix (MM):

$$S' = \begin{pmatrix} m_{11} & m_{12} & m_{13} & m_{14} \\ m_{21} & m_{22} & m_{23} & m_{24} \\ m_{31} & m_{32} & m_{33} & m_{34} \\ m_{41} & m_{42} & m_{43} & m_{44} \end{pmatrix} \begin{pmatrix} S_0 \\ S_1 \\ S_2 \\ S_3 \end{pmatrix} = \mathrm{MM.S} \qquad (11)$$

The explicit relation between the Jones matrix and the elements of the Mueller Matrix (MM) are detailed in Appendix 1. It is usual to normalize the Stokes vector to S_0 and the Mueller matrix to m_{11}, in the remaining part I will use this convention. The following example is the Mueller matrix for a polarizer with an angle of θ with respect to the x-axis.

$$\mathrm{MM}_{\mathrm{polarizer}} = \frac{1}{2} \begin{pmatrix} 1 & \cos(2\theta) & \sin(2\theta) & 0 \\ \cos(2\theta) & \cos^2(2\theta) & \cos(2\theta)\sin(2\theta) & 0 \\ \sin(2\theta) & \cos(2\theta)\sin(2\theta) & \sin^2(2\theta) & 0 \\ 0 & 0 & 0 & 0 \end{pmatrix}$$

Then if θ = +45

$$\mathrm{MM}_{45^\circ} = \frac{1}{2} \begin{pmatrix} 1 & 0 & 1 & 0 \\ 0 & 0 & 0 & 0 \\ 1 & 0 & 1 & 0 \\ 0 & 0 & 0 & 0 \end{pmatrix}$$

The MM for a wave plate that has a phase difference of φ and a fast axis orientation of θ, will be:

$$\mathrm{MM}_{WP}(\varphi) = \begin{pmatrix} 1 & 0 & 0 & 0 \\ 0 & \cos^2(2\theta) + \sin^2(2\theta)\cos(\varphi) & \cos(2\theta)\sin(2\theta)(1-\cos(\varphi)) & \sin(2\theta)\sin(\varphi) \\ 0 & \cos(2\theta)\sin(2\theta)(1-\cos(\varphi)) & \cos^2(2\theta)\cos(\varphi) + \sin^2(2\theta) & -\cos(2\theta)\sin(\varphi) \\ 0 & -\sin(2\theta)\sin(\varphi) & \cos(2\theta)\sin(\varphi) & \cos(\varphi) \end{pmatrix}$$

Then, for a quarter-wave plate, that has the fast axis vertical:

$$\mathrm{MM}_{QWP}(\varphi = {}^{\pi}/_{2}) = \begin{pmatrix} 1 & 0 & 0 & 0 \\ 0 & 1 & 0 & 0 \\ 0 & 0 & 0 & -1 \\ 0 & 0 & 1 & 0 \end{pmatrix}$$

To illustrate the Stokes-Mueller formalism, let us consider the transformation of the polarization state of unpolarized light sent through a polarizer at 45° and a quarter-wave plate with vertical fast axis.

$S' = \mathrm{MM}_{QWP}(\varphi = {}^{\pi}/_{2}).\,\mathrm{MM}_{45°}\,.\begin{pmatrix} 1 \\ 0 \\ 0 \\ 0 \end{pmatrix}$ then $S' = \frac{1}{2}\begin{pmatrix} 1 \\ 0 \\ 0 \\ 1 \end{pmatrix}$ which represents right circularly polarized light. This formalism explains how to transform the naturally linear polarization of the laser of the LMJ to a circular polarization by using quarter-wave plates.

Finally, the MM describes the anisotropic property of a material with a 16-parameter matrix with eight basic optical properties. As we have seen in Section 1.2, for anisotropic materials the optical constants of materials depend on the polarization orientation. The relations between the MM elements and the basic optical properties are presented in Table 4. These elements vary within the refractive index (n), the extinction coefficient (κ), the path length through the medium (d), and the wavelength of light in vacuum (λ_0). Subscripts specify the polarization of light as x, y, 45° to the x axis, 135° to the x axis, circular left and circular right.

Table 4. Eight optical properties of the Mueller matrix [71], [72]

isotropic phase retardation = η	$2\pi nd/\lambda_0$	$MM = \begin{pmatrix} k & -LD_0 & -LD_{45} & CD \\ -LD_0 & k_0 & CB & LB_{45} \\ -LD_{45} & -CB & k_{45} & -LB_0 \\ CD & -LB_{45} & LB_0 & k_{circ} \end{pmatrix}$
isotropic amplitude absorption = k	$2\pi\kappa d/\lambda_0$	
(x-y) linear dichroism = LD_0	$\frac{2\pi}{\lambda_0}(\kappa_x - \kappa_y)d$	
(x-y) linear birefringence = LB_0	$\frac{2\pi}{\lambda_0}(n_x - n_y)d$	
45° linear dichroism = LD_{45}	$\frac{2\pi}{\lambda_0}(\kappa_{45} - \kappa_{135})d$	
45° linear birefringence = LB_{45}	$\frac{2\pi}{\lambda_0}(n_{45} - n_{135})d$	
circular dichroism = CD	$\frac{2\pi}{\lambda_0}(\kappa_{left} - \kappa_{right})d$	
circular birefringence = CB	$\frac{2\pi}{\lambda_0}(n_{left} - n_{right})d$	

The relationship between phase difference and birefringence is outlined in the following equation:

$$\varphi = \frac{2\pi d}{\lambda}\Delta n \qquad (12)$$

According to what we have seen above and to Eq. (12), the terms that play a role on the birefringence are the thickness of the coating (d) and the indices (n). In the next sections, we will see that the indices are related to the geometry of the GLAD columns. In Chapter 5, I will demonstrate that, to obtain the correct phase difference of $\varphi = {}^{\pi}/_{2}$, we can control the birefringence (Δn) by adjusting the deposition angles. In summary, Eq. (12) explains why the control over the geometry of the GLAD films and their thickness is crucial to achieve a QWP and, subsequently, a circular polarization of the laser beams.

1.4. Modeling anisotropic porous films using Bruggeman model and the depolarization factors

The new materials that were characterized and modeled are a mixture of materials. The effective medium approximation (EMA) governs the description of the refractive index of a mixture of materials.

A mixture of materials is mostly a composite material constituted of a matrix (the largest component, ε_m) that contains inclusions (ε_i). From the optical properties' perspective, it is interesting to assess the optical constants of the composite using only the ones of the matrix and inclusions.

To simplify the calculus, EMA has been proposed. This model considers the composite material as a new material with a new effective permittivity ε_{eff}. To use the EMA, the inclusions and their dimensions should be smaller than the wavelength [73]. There are two principal theories that can be used for isotropic matrix and isotropic inclusions (Figure 15): Maxwell-Garnett theory and Bruggeman theory.

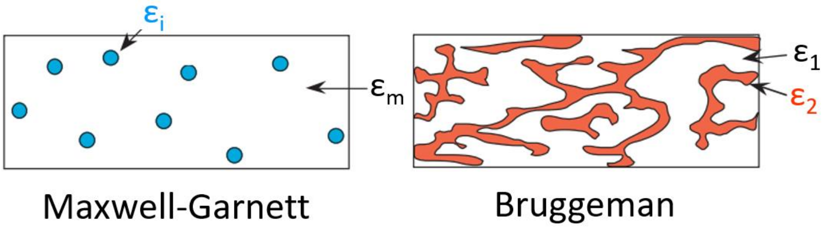

Figure 15. Two main theories to approximate an effective medium: Maxwell-Garnett and Bruggeman [73].

The Maxwell-Garnett (MG) theory [74], [75] is used for disordered spherical inclusions that represent less than 10% of the matrix [76]. This model is particularly well suited for the description of the properties of composites containing metallic inclusions.

MG theory [75]

$$\frac{(\varepsilon_{eff}-\varepsilon_m)}{(\varepsilon_{eff}+2\varepsilon_m)} = f_i\frac{(\varepsilon_i-\varepsilon_m)}{(\varepsilon_i+2\varepsilon_m)} \tag{13}$$

with f_i the volume fraction of the inclusions.

The Bruggeman Effective Medium Approximation (BEMA) is used for interspersed disordered inclusions [76], [77]. The assumption of this theory is that each component is a composite material (i.e. inclusions in a matrix) of the effective medium and each constituent is treated on an equal footing; each interacts with the other.

For a composite material composed of spherical inclusions of two materials with permittivities ε_1 and $\varepsilon_2$and volumes fractions f_1 and f_2, the effective permittivity of the composite, ε_{eff}, is given by:

BEMA [77]

$$f_1\frac{(\varepsilon_1-\varepsilon_{eff})}{(2\varepsilon_{eff}+\varepsilon_1)} + f_2\frac{(\varepsilon_2-\varepsilon_{eff})}{(2\varepsilon_{eff}+\varepsilon_2)} = 0 \tag{14}$$

MG and BEMA theories have been adapted for ellipsoidal cross-section shaped inclusions. In this case, the medium becomes anisotropic. Since the GLAD coatings studied for this work are transparent and contain a high fraction of porosity, only the Bruggeman theory was used [78], and we will focus on that one. This model is called **Anisotropic Bruggeman Effective Medium Approximation (ABEMA)** [74]. Orientation and shape distribution can also be considered [79]. However, for dielectric ellipsoidal inclusions all oriented in the same direction ABEMA is sufficient and three effective permittivities can be determined, hence defining a composite with biaxial optical anisotropy:

$$f_1 \frac{(\varepsilon_1 - \varepsilon_{eff,j})}{\varepsilon_{eff,j} + L_j(\varepsilon_1 - \varepsilon_{eff,j})} + f_2 \frac{(\varepsilon_2 - \varepsilon_{eff,j})}{\varepsilon_{eff,j} + L_j(\varepsilon_2 - \varepsilon_{eff,j})} = 0 \tag{15}$$

$$j = a, b, c$$

L_j is the depolarization factor that depends on the geometry of the inclusions. Here, the inclusion has an ellipsoidal shape, with semiaxes a, b, c that are parallel to the axes x, y, z, as depicted in Figure 16. L_j is comprised between 0 and 1. Equation (16) defines the depolarization factors as a function of the axes [80].

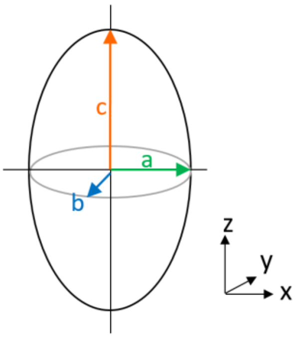

Figure 16. Ellipsoidal shape of the inclusions

$$L_j = \frac{abc}{2} \int_0^\infty \frac{dq}{(j^2 + q) f(q)} \tag{16}$$

With $f(q) = \{(q + a^2)(q + b^2)(q + c^2)\}^{1/2}$

There are no analytical solutions to Eq. (16). However, if a = b = c, which is a sphere, $L_a = L_b = L_c = {}^1/_3$. Only two factors are independents since $L_a + L_b + L_c = 1$. If $a > b > c$, $L_a < L_b < L_c$ [78], [80].

Interestingly, the depolarization factors are linked to the geometry of the ellipsoids but not their dimensions. Figure 17 presents the evolution of the refractive index in the z direction (c axis) as a function of the morphology of the ellipsoid by adjusting L_z. For that example, the ABEMA theory was used with 80 % of silica and 20 % of void and $L_x = L_y$. L_z can vary between 0 (infinite rod along z) and 1 (infinite x-y plane). It can be seen that L_z and n_z follow the opposite trend.

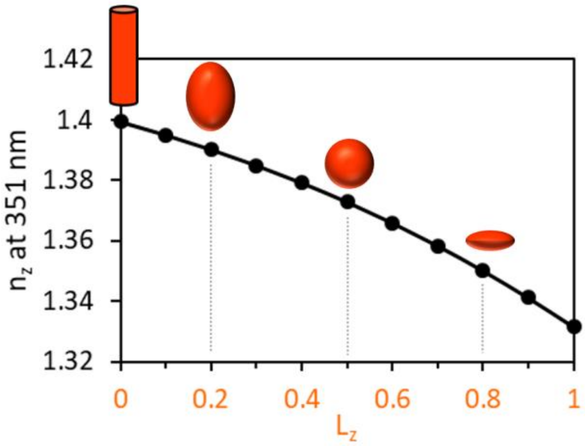

Figure 17. Morphology of an ellipsoid as a function of L_z with $L_x = L_y$. Value of n_z for an ABEMA theory as a function of the value of L_z.

Therefore, by controlling the shape of the inclusions, the optical anisotropy can be managed and the birefringence of dielectric materials can be handled. Thus, the QWP coatings can be done by fabricating thin films with ellipsoidal inclusions. We will see in the following sections that the GLAD films are composed of columns with an ellipsoidal cross-section (x-y plane) following the same direction, and surrounded by vacuum (more than 10%).

1.5. Measurement techniques to characterize the optical anisotropy

The retardance of GLAD films has been measured using an ellipsometer. Ellipsometry is a non-destructive optical technique that allows, for the standard version, the determination of the refractive index (and porosity) and the thickness of material layers. The principle of this technique is presented in Figure 18: a known polarized light (generally linear) is transmitted or reflected by the sample, after the sample, the polarization becomes elliptical and the parameters of the output polarization are determined.

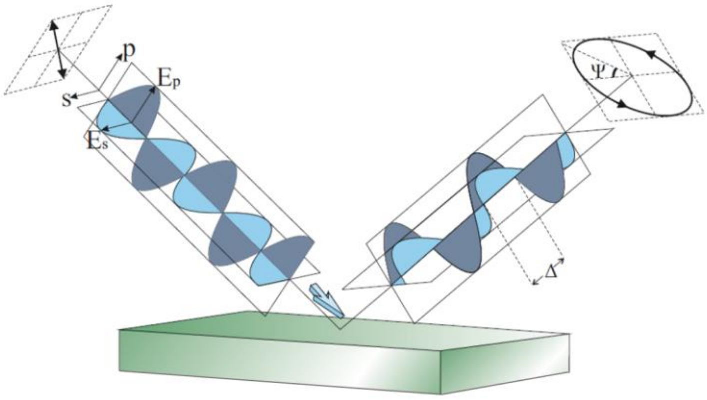

Figure 18. Principle of standard ellipsometry [81].

In more detail, the polarization can be split into two elements, an element parallel to the incident plane (E_p) and an element perpendicular to the incident plane (E_s). The incident polarization E_i becomes E_r after reflection and can be represented using reflection coefficients r_p and r_s for the two components of the polarization [82]. The coefficient for a polarization parallel to the incident plane is defined as:

$$r_p = \frac{E_{pi}}{E_{pr}} = |r_p| e^{i\delta_p} \tag{17}$$

And the reflection coefficient for a polarization perpendicular to the incident plane:

$$r_s = \frac{E_{si}}{E_{sr}} = |r_s| e^{i\delta_s} \tag{18}$$

With $|r_p|$ and $|r_s|$ the amplitude modifications and, δ_p and δ_s the retardance introduced by the reflection.

In reality, the measured parameters are Psi (Ψ) and Delta (Δ) which are the ratio of the two reflections coefficients:

$$\rho = \frac{r_p}{r_s} = \tan(\Psi) e^{i\Delta} \tag{19}$$

Psi is the ratio of $|r_p|$ to $|r_s|$ and delta is the phase difference between the two components of the electric field. In this work, the ellipsometric measurements have been mostly performed using an RC2 ellipsometer from J.A. Woollam (Figure 19(a)).

In practice, before the sample, the device is equipped with a light source, a polarization generator and after the sample a polarization analyzer and a detector (Figure 19(b)).

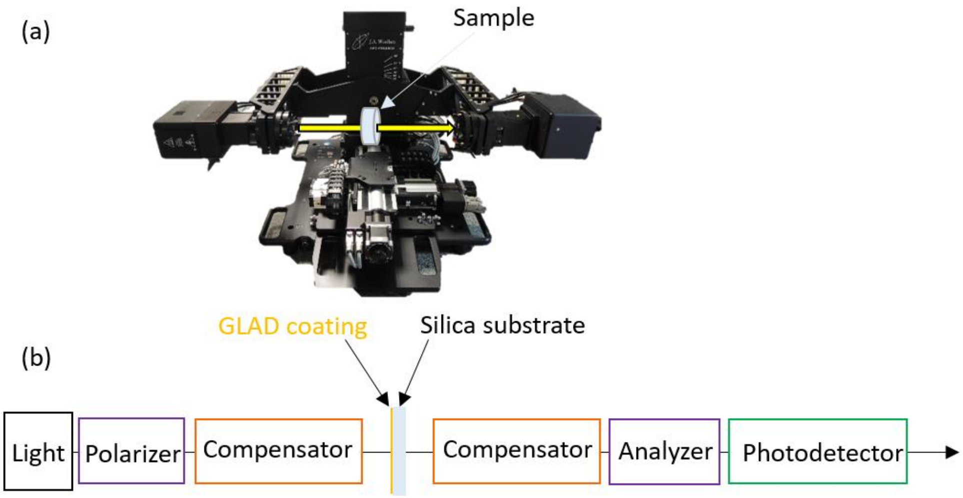

Figure 19. (a) Photo of the ellipsometer used to measure the samples. (b) Schematic of the ellipsometer.

However, Eq. (19) is mostly useful for isotropic samples. In this thesis, I have measured anisotropic samples. The ellipsometer used in this study also allows for the measurement of the 16 Mueller matrix elements which, as we have seen in Section 1.4, are appropriate for the characterization of optical anisotropy, and birefringence in particular. For this thesis, the measurements of the 16 MM elements were performed in transmission from 210 to 1690 nm, for the fast axis at 0°, 45° and 90° (Figure 20).

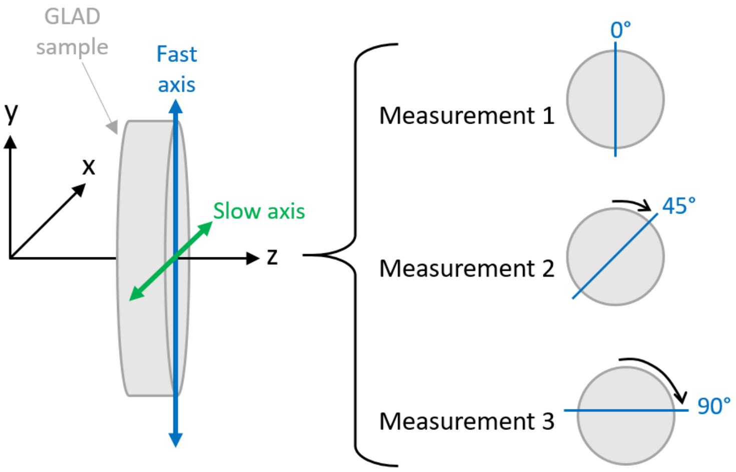

Figure 20. Measurements performed on the ellipsometer to characterize the retardance.

Once the measurement is performed, a model must be created on the ellipsometer software CompleteEASE (J.A. Woollam). This model is the interpretation of the physical parameters of the measured samples to optical properties: thickness, refractive index, void percentage, roughness, mixed-materials, etc. Then, the created model generates a Mueller matrix that is fitted to all the measured Mueller matrices thanks to a regression analysis. To evaluate the fit, an indicator called unbiased Mean Squared Error (MSE) is used. It is the sum of the quadratic differences between the measured data and the modeled data for all the measurement wavelengths corrected for the measurement uncertainty and number of parameters in the model. The lowest the MSE is, the better the results will be at the condition that the results are physical.

As explained earlier, the optical anisotropy can be modelled using the depolarization factor L which can be decomposed for each principal axis (x, y and z) by the depolarization factors L_x, L_y and L_z. However, CompleteEASE describes the depolarization split D_{xy} rather than the depolarization factors directly:

$$L_x = D_{xy}(1 - L_z), L_y = \left(1 - D_{xy}\right)(1 - L_z)$$
$$0 \leq L_z \leq 1 \qquad (20)$$

For elongated columns with biaxial anisotropy, L_x and L_y are associated with the in-plane dimensions of the ellipsoid that define the directions of the optical axes. L_z is oriented along the column height, parallel to the surface normal. The relation between the optical axes of the sample and the ellipsometer referential is described by applying rotations through the Euler angles.

Another technique was used to characterize the retardance: a birefringence mapper (BM) (Hinds Instruments Exicor 450XT Mueller matrix polarimeter). The functioning of the birefringence mapper is comparable to that of the ellipsometer, with the distinction that the mapper operates at a single wavelength of 355 nm.

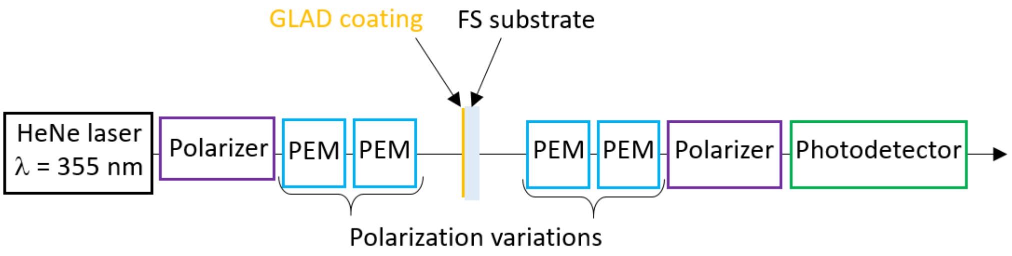

Figure 21. Schematic of the birefringence mapper. PEM is for PhotoElastic Modulators.

Figure 21 shows the schematic of the birefringence mapper. A laser beam is polarized thanks to a linear polarizer. The polarization is modulated with two PhotoElastic Modulators (PEMs). The beam is transmitted through the sample and then passes through a combination of two more PEMs and a polarizer. Then, a photodetector converts the time-modulated intensity of the transmitted light into an electric signal which is finally analyzed and converted into the sixteen Mueller matrix elements. The advantage of this technique is the possibility to realize a map of the birefringence by translating the surface in the x-y directions. The linear retardation resolution/repeatability of this instrument is 0.01 nm / ± 0.03 nm.

2. Description of the GLAD serial bideposition technique to create birefringence

Glancing Angle Deposition is a physical vapor deposition (PVD) technique. To understand the specificity of this technique, let's begin with the **growth of a PVD thin film**. It is divided into 3 steps:

- First, the material to be coated which is placed in a crucible, is vaporized thanks to a thermal source in a high vacuum environment (between 10^{-5} and 10^{-9} Torr). The thermal source used for this thesis is an electron beam bombardment (e-beam evaporation). The raw material is often in pellets.
- The vaporized species are transported from the source to the substrate thanks to a highly directional collimated vapor flux. Depending on the coated material, a reactive gas can be added (O_2, N_2 or CH_4). In this case, it is called a reactive evaporation.
- Finally, the vapor condenses on the substrate and forms a thin film with the germination/growth mechanism. More specifically, the species are adsorbed on the surface by Van der Waals bonds.

Depending on the thermal energy and the strength of the atom-substrate interaction, the adsorption is permanent or temporary. The atom is then either absorbed, called adatom, or re-evaporated from the surface.

After that, the adatom can diffuse on the surface and form aggregates/nuclei, which is the germination stage. Finally, the aggregates can form islands, which coalesce when they come together to form a continuous structure and increase in thickness.

2.1. Analysis of the tilted films fabricated using the GLancing Angle Deposition (GLAD) technique

The **specificity of the GLAD technique** is the orientation of the substrate which is tilted at a glancing angle. Figure 22 presents the GLAD technique from a front view (a) a side view (b) and a side view with a zoom on the column growth (c). In Figure 22(a), the elements described above are present: the electron beam that evaporates the material in the crucible, the vaporized material that condenses on the oriented substrate in a high vacuum coater.

The orientation of the substrate is expressed by α (Figure 22(b) and (c)), it defines the angle between the substrate normal and the incident vapor flux. GLAD generally takes place at α > 60°.

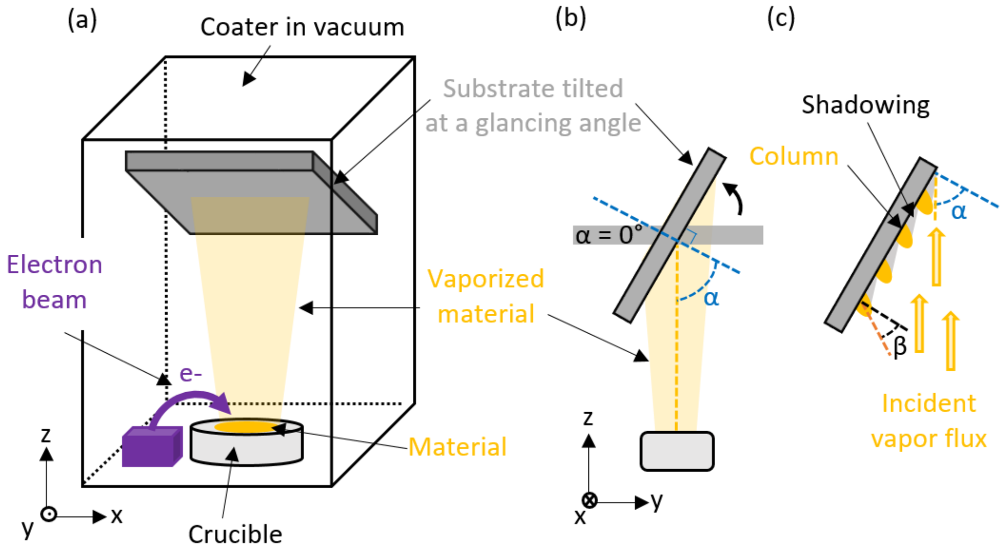

Figure 22. Principle of GLAD. (a) Schematic of a GLAD coater. (b) Side view of the schematic presented in (a). (c) Zoom on the formation of the columns with the shadowing regions.

Tilting the substrate angle has an impact on the growth of the thin film described above. As shown in Figure 22(c), during the growth of the film, because of the orientation of the substrate, some areas are hidden from the vapor flux. This phenomenon is called ballistic shadowing or simply shadowing. It is highly accentuated for such glanced angles. Because of the shadowing and the low diffusion, the formed structures are oriented columns in the direction of the vapor flux (Figure 22(c)) but, importantly, the angle β between the long axis of the columns and the normal to the surface and the glancing angle α are different, with $\beta < \alpha$.

In order to form defined columns, the diffusion must remain low. Movchan [83] and Thornton [84] have built a Structure Zone Model (SZM) to describe the morphology of PVD thin films depending on the substrate temperature and the pressure in the coater. The surface mobility of the adatom increases with the temperature. In the SZM, GLAD must remain within zone 1 ($^{T_s}/_{T_m} < 0.3$) where diffusion is limited and unable to fill-in void regions. T_s is the substrate temperature and T_m the melting point of the deposition material. GLAD films are typically conducted at room temperature or near.

In addition to the oriented columns, the shadowing creates competition between the columns (Figure 23(a)). During the growth, some columns grow faster than others. The smaller ones fall into the shadow of the larger ones, stopping their growth [85]. It can be noted that, by tilting the orientation of the substrate, the created shadow is asymmetric. In the direction of the plume, represented by yellow arrows in Figure 22 and Figure 23, the shadow maintains the gap between the columns and width is controlled. In the direction perpendicular to the plume, the growth of the column is not controlled, creating a progressive fanning of the column cross-section. Figure 23 illustrates the formation of these elliptical cross-section columns. In reality, the cross-section of the columns is more crescent shaped. These columns have rough apexes due to molecular nucleation and associated shadowing. This roughness is an important factor in the rate at which the columns broaden [85]. In some cases, large mounds can grow on top of the column, splitting it into multiple sub-columns. This phenomenon is exacerbated by the thickness and large width of the columns, as well as by the low-temperature coating that induces low diffusion: “bifurcation is a natural byproduct of column broadening” [85].

To summarize, by tilting the orientation of the substrate, a shadowing effect and a low diffusion allow for the formation of well separated slanted columns in one direction and with an increasingly elliptical cross-section observed in the other direction.

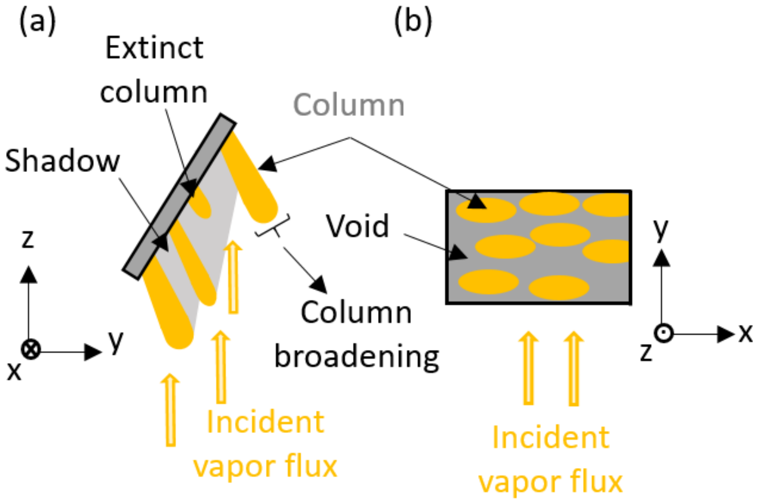

Figure 23. (a) Side view of a GLAD film growing the competition between the columns that leads to the extinction of one column and the broadening (b) Top view of a GLAD coating.

These columns exhibit two separate structural anisotropies: the tilt direction of the columns and the fanning of the columns.

By playing with the orientation of the substrate (glancing angle or polar angle), the shadowing effect is changed and consequently the morphology and the properties of the GLAD structures are modified. Birefringence can be optimized using a more complex substrate motion such as the **Serial Bideposition (SBD)** developed by Hodgkinson *et al.* [86].

2.2. Utilization of the Serial BiDeposition (SBD) technique to increase the anisotropy

Figure 24 presents the mechanism of the serial bideposition. It is based on a substrate motion performing back and forth polar rotations by 180° between the subdeposit angles (also noted ± α), with a fast growth time per subdeposit angle (few seconds for few nanometers). The polar rotation between the two subdeposit angles is at high speed (180 °/s). The fast growth time per subdeposit angle grants the fabrication of columns perpendicular to the substrate (Figure 24(a)).

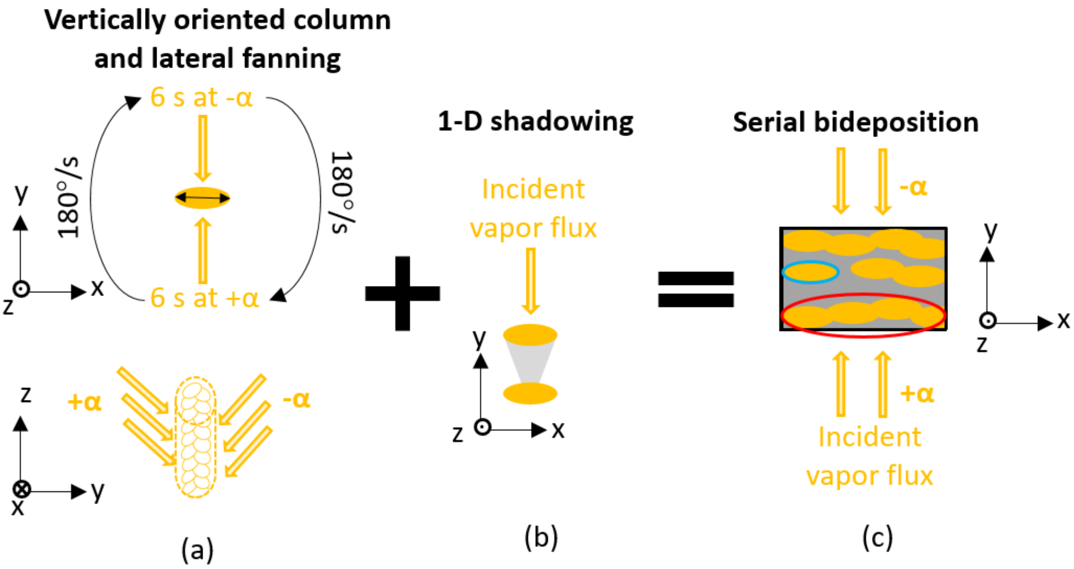

Figure 24. Fabrication of an anisotropic coating using the serial bideposition substrate motion. (a) Widening of the columns and growth perpendicular to the substrate. (b) Void in only one direction. (c) Final SBD structure.

In the same manner as explained above, the one-directional shadow allows the column to grow in one direction, the direction perpendicular to the incoming vapor flux, making the columns ellipsoidal-shaped. In parallel, in the direction of the incoming flux, a certain amount of void arises (Figure 24(b)). Then, the anisotropy of the film deposited using the SBD substrate algorithm is the combination of the ellipsoidal cross-section of the columns (structural asymmetry associated with fanning) as well as the shadowing in one direction yielding bunching of columns, both in the direction perpendicular to the growth directions (Figure 24(c)) [38], [85]. Some columns stay alone (blue circle) and some merge together (red circle). Importantly, the long axis of the columns is perpendicular to the surface of the substrate.

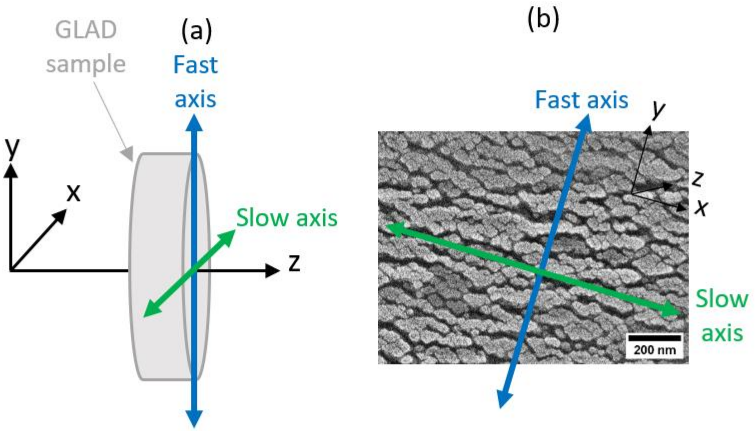

Figure 25. GLAD sample in the coordinate system of the ellipsometer. (a) Side view. (b) Top view on the Scanning Electron Microscopy image of the surface on an actual GLAD coating.

As explained in the previous sections, we decided to model the anisotropy of the GLAD films using the depolarization factors. However, the ellipsometry measurements were performed in transmission at normal incidence (Figure 25). As a result, only the in-plane birefringence between n_x (L_x) and n_y (L_y) was assessed (Figure 26). L_z couldn't be measured and was set to a constant value. Because the height of the columns is much larger than the size of their section, we approximate L_z as if from a rod of infinite length, $L_z = 0$ (Figure 17).

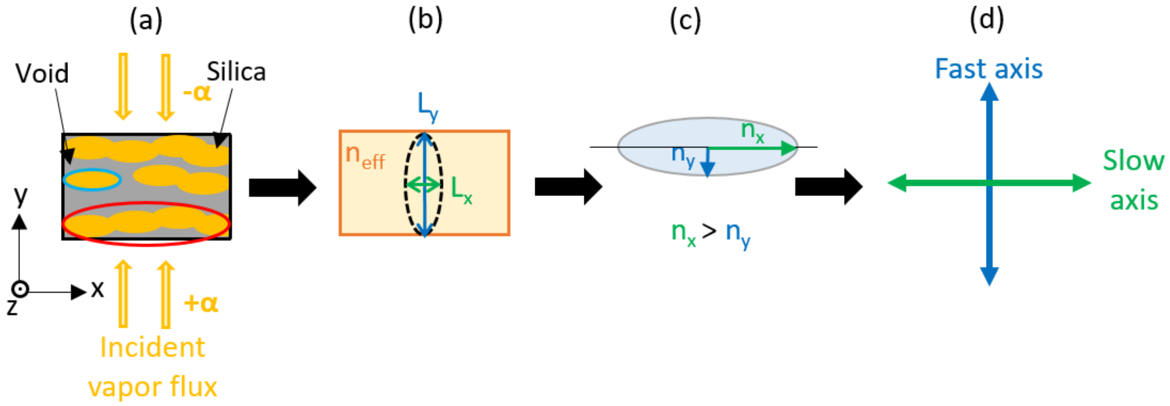

Figure 26. (a) Physical description of the coating. (b) Description of the coating following the ABEMA theory with the depolarization factors. (c) Index ellipsoid of the GLAD film. (d) Orientation of the fast axis and the slow axis following the previous descriptions.

In the case of elongated columns with biaxial anisotropy, L_x is associated with the longest dimension of the ellipsoid and L_y with the smallest dimension (Figure 26(a)). As outlined in Section 1.4, the depolarization factor is inversely proportional to the dimensions. Therefore, the ellipsoid that defines the depolarization factors has the geometry presented in Figure 26 (b). The refractive indices follow the opposite trend of the depolarization factors (Figure 17 from Section 1.4). As a result, the index ellipsoid will be rotated 90° (Figure 26(c)). Consequently, the optical axes are oriented as follows: the fast axis, small refractive index, is oriented along the smallest dimension of the ellipsoid (the x-axis), and the slow axis, high refractive index, is oriented along the longest dimension of the ellipsoid (the y-axis). Then, starting back from the equation of the depolarization split D_{xy} (Eq. (20)), with $L_z = 0$, $L_x = D_{xy}$ and $L_y = 1 - L_x$.

In summary, in order to control the anisotropy of the GLAD films, it is necessary to adjust the deposition angle α. However, the relation between the planar birefringence Δn and the angle α is not immediately apparent.

The determination of this maximum birefringence is specific to each material and deposition process. Empirical studies demonstrated that maximum birefringence (≃ 0.04 - 0.07) is reached at $\alpha = 70° \pm 10°$ [85].

2.3. Technical description of the fabrication of the GLAD coatings

Figure 27 presents the coater used to fabricate the samples [26], [87]. It is located at the Laboratory for Laser Energetics (LLE) at the University of Rochester in the USA, in the Optical Manufacturing group, directed by Amy Rigatti.

The coater is a 1.2-m vacuum chamber equipped with an electron-beam gun (EB Sources) which is located directly below the aperture, a quartz crystal microbalance on the side is used to measure the deposition rate and the thickness as well as a custom GLAD stage (Angstrom Engineering) capable of holding two 50-mm diameter substrates (fused silica and/or silicon) or one 100-mm diameter substrate. For SBD, the stage is rotated around the horizontal axis (substrate tilt) to the desired ± α angle every 6 s at a speed of 180 °/s. Silica is evaporated at a rate of 9 Å/s The chamber is heated at 25 °C thanks to quartz lamps and evacuated to a pressure better than 1×10^{-6} Torr. Silica growth is carried out without the addition of reactive gases. For alumina coatings, oxygen backfill is added at a partial pressure of 1.4×10^{-4} Torr.

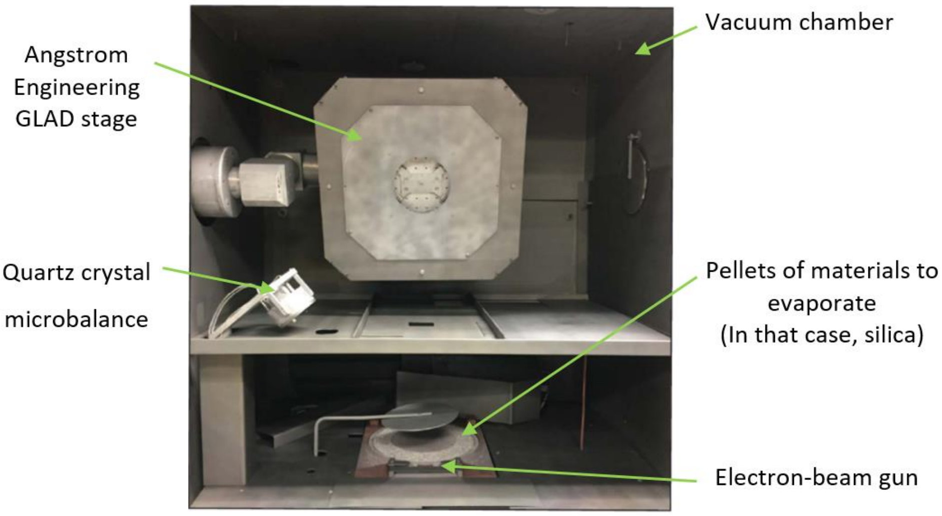

Figure 27. Photo of the GLAD coater of the Laboratory for Laser Energetics [26].

3. Laser damage resistance

Using a material for a high-power laser application requires to examine its behavior in the presence of high energy laser. Every material has a Laser Induced Damage Threshold (LIDT) which gives the fluence (energy per surface unit) above which the laser-material interaction has a high probability of causing an irreversible modification of the component. Figure 28 is the example of a damage site on a multilayer QWP made of silica and deposited using electron beam evaporation.

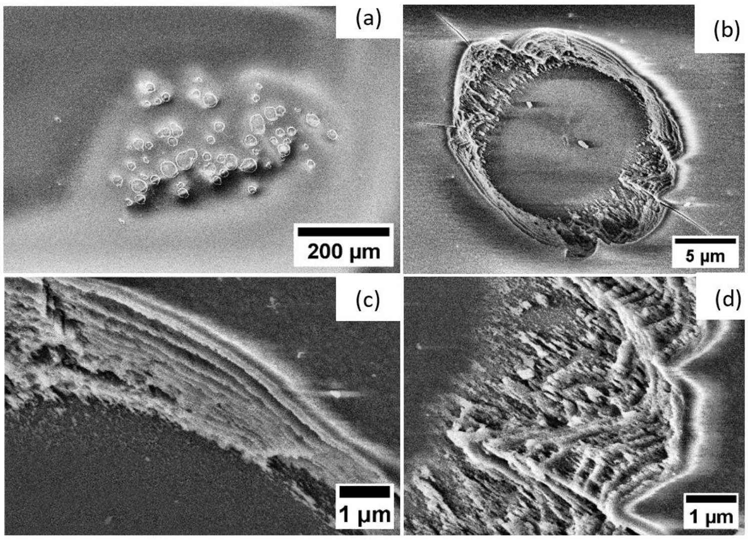

Figure 28. Scanning electron microscope images of a damage site in a multilayer QWP made of silica. Test: 1-on-1, λ = 355 nm, 7 ns, S_{eq}: 6.5 x 10^{-3} cm² (a) One entire damage site (b) Zoom on one little hole (c) and (d) Higher magnification on the edges of the hole, the different layers of the coating are visible. The bottom part of the holes is the silica substrate.

To measure the LIDT during this thesis, two laser set-ups were used: one at CEA and a second at the Fresnel Institute (Marseille, France). The second one allows for characterization in several environments (vacuum, ambient air, etc.). The laser at CEA, named ELAN, operates at 355 nm with a 7-ns pulse length, and an equivalent beam surface of 3.7 x 10^{-3} cm². The laser at Fresnel Institute operates at 355 nm with picosecond (ps) pulses train in a ns window and an equivalent beam surface of 9.3 x 10^{-5} cm². The details on the set-ups are in Appendix 2 and Appendix 3. All the laser resistance tests were performed with the 1-on-1 method (as defined in the norm ISO/FDIS 21254-1 and 21254-2) described in Figure 29.

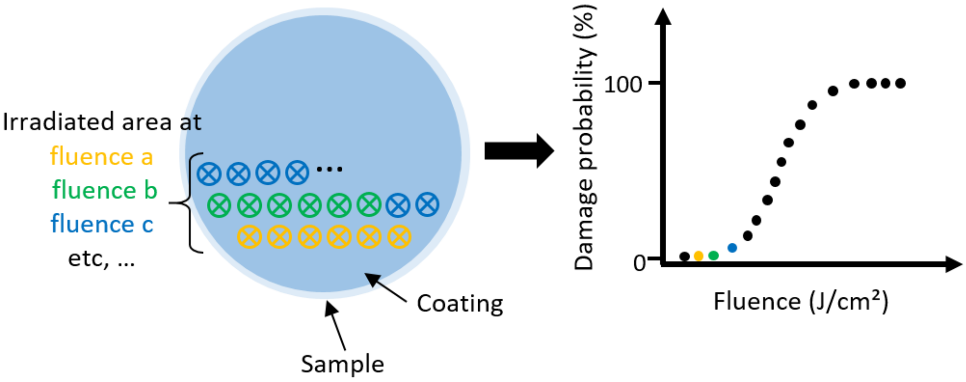

Figure 29. Front view of a sample with different irradiated sites and graph of the results of a 1-on-1 test.

The 1-on-1 method described in Figure 29 consists in testing the surface to a single shot at a fixed fluence, N times. The tested sites (represented by the different colored circles) are then inspected using differential interference contrast microscopy, also known as Nomarski microscopy, at a magnification higher than x100. The presence or absence of a damage site allows statistical models to evaluate damage probability. It is important to note that 1-on-1 tests may overestimate the threshold when dealing with optical elements that feature low-density defects. Raster scan tests are a solution for addressing this issue. The process involves scanning the surface at a constant fluence.

4. Description of secondary characterization techniques

4.1. Techniques used to determine the chemical composition

To comprehensively assess the optical performance of the GLAD samples, it is essential to characterize their chemical composition. Three techniques have been used: Raman spectroscopy, Fourier Transform InfraRed spectroscopy (FTIR) and Glow Discharge Optical Emission Spectrometry (GD-OES) for depth profile. FTIR and Raman spectroscopy are non-destructive techniques, unlike GD-OES.

The operating principle of the Raman spectroscopy is as follows: a laser is focused on the surface of a sample which excites the vibrational modes of the molecules of the material being measured and some photons are scattered. Figure 30 presents the three types of scattering: Rayleigh, Raman Stokes, and Raman anti-Stokes. Unlike Rayleigh scattering, Raman scattering is inelastic. Inelastic scattering results in the energy of the photon scattered being different from the energy before the interaction.

In Raman spectroscopy, both the Stokes and anti-Stokes scattering can be measured, but Stokes scattering is the primary signal used. The scattered light is collected and analyzed using a spectrophotometer. Raman probes transitions between vibrational levels that are called "virtual" vibrational levels because they are not true electronic states. The measurements are presented in Raman shift in cm^{-1}.

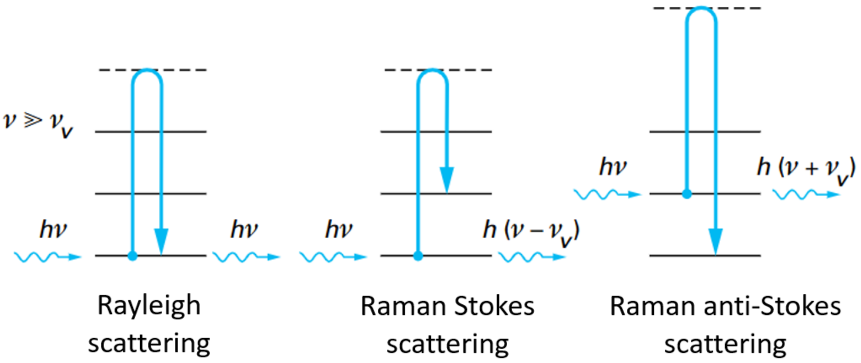

Figure 30. Three types of scattering phenomena illustrated by the vibrational energy levels for the interaction of a photon on a material [88].

We used a Renishaw confocal Raman microscope for these measurements with an excitation at 532 nm. The Raman shift was measured from 200 to 4000 cm^{-1}. All spectra were acquired with a 100x objective (0.85 numerical aperture and a 0.33-mm working distance), which provided an approximate laser spot size of 0.7 mm. The measurements of the coatings were performed with silica substrates.

For FTIR, an infrared beam is directed at the sample. It excites the nucleus of molecules that can result in an absorption if this movement changes the dipolar moment of the molecule. The vibrations of excited molecules are characteristic of the material's molecular bonds. The Fourier transform is used to convert the temporal signal into a frequency signal. The result is a transmittance spectrum of the thin film. We used a Nicolet and a PerkinElmer Spectrum Two. Each measurement was the average of 32 scans over the 400 to 4000 cm^{-1} range. The separation between two peaks (spectral resolution) was set to 8 cm^{-1}. The measurements were performed from the coatings on double side polished silicon substrates due to their IR transparency property. This technique allows for accessing different vibrational modes of the materials, thus completing the Raman spectroscopy characterizations.

Glow Discharge Optical Emission Spectrometry (GD-OES) was performed to access a concentration profile of coatings on silicon substrates. It works as follows: in a chamber, an argon plasma is generated by a discharge between an anode and a cathode, the sample being the cathode. The sample is connected to a radio frequency source, because of its insulating property. Atoms from the surface of the substrate are ablated and excited by collisions with electrons in the plasma. When the excited atoms of the sample finally return to their original energy level, they emit the excess energy in the form of photons. Then, an optical spectrometer measures the wavelength of each photon which is characteristic of the original atom. The ablation process allows probing different depth of the sample as a function of experiment duration.

This measurement was performed using a GD-Profiler 2 (HORIBA Jobin Yvon) applying pressure of 650 Pa, a RF-power source of 50 W and a 1 data acquired every 0.1 s. Because no reference samples could be used, the intensities of the reported species are non-quantitative.

4.2. Characterization of the morphology

To characterize the topography, a Jeol JSM, a Hitachi, and a Raith Scanning Electron Microscope (SEM) were used. They were also used to observe cross-section of the coatings, to characterize the thickness and the morphology. The principle of SEM is described as follows: in a vacuum environment, a beam of electrons is focused on the sample and scans the surface. The interaction between the electrons and the sample causes several types of emissions to form: secondary electrons, which highlight the topography of the sample; backscattered electrons, which provide an image with chemical contrast; and finally, X-ray photons for the chemical analysis using energy dispersive spectroscopy (EDS). Some samples were coated with few nanometers (from 2 to 5 nm) of platinum to facilitate observation by removing accumulated charges from the surface. These observations were generally performed on the coatings deposited on silicon substrates.

4.3. Measurement of the transmission spectra

We measured the transmission of these films with two spectrophotometers: a PerkinElmer Lambda 1050 and a PerkinElmer 900. Measurements were taken at normal incidence from fused silica substrates between 200 and 1400 nm, with intervals of 1 or 2 nm.

Reflection was collected using an in-house built measurement system. A spectrophotometer works as follows: a monochromatic light from a polychromatic source (deuterium/tungsten) is directed toward the sample. For the desired wavelength range, the light passes through the sample, and a detector measures its intensity. Transmission is the ratio of the intensity of the input light to the intensity of the output light. The sample is measured in a chamber that allows for transmission characterization in various environments, including vacuum, ambient air, etc.

5. Summary of Chapter 2

This second chapter presented the theoretical knowledge discussed throughout this thesis.

Within the context of this work of polarization smoothing using circular polarizations, we want to obtain quarter-wave plates as we have shown using the Stokes-Mueller formalism. This formalism will be used to characterize the polarimetric properties of materials. The relation between the shape of inclusion, in composite materials, and the refractive index of the composite was introduced. The optical measurements used to determine the polarization dependent properties of the films were presented.

The samples, envisioned as quarter-wave plates, will be realized using standard evaporation techniques with Glancing Angle Deposition (GLAD) and a substrate motion algorithm called Serial BiDeposition. The films exhibit two types of anisotropy: one related to the form of the substructure and the other due to the overall porosity only following one direction. Thus, to manipulate the birefringence, work must be done on the microstructure of the coatings. The samples were fabricated in a coater located in the Laboratory for Laser Energetics (University of Rochester, USA).

Main characterization techniques were described such as the resistance to laser damage with 1-on-1 tests; the chemical composition using Raman spectroscopy, Fourier Transform InFrared spectroscopy (FTIR), and Glow Discharge Optical Emission Spectroscopy (GD-OES); the morphology with a Scanning Electron Microscope (SEM); and the optical transmission using a spectrophotometer.

Chapter 3. Performance in air of quarter-wave plates GLAD coatings

After reviewing the context and the challenges associated with this thesis, as well as the optical principles behind the studied phenomena, this chapter will explore one method for producing quarter-wave plates.
This chapter will start with a description of the studied silica GLAD QWPs. These are 21-layer films in silica. The devices will be characterized in terms of topography, microstructure, and composition of their matrices. The second part of this chapter will evaluate the optical performance of the silica QWPs. The relationship between the optical properties and microstructure will be studied through ellipsometry measurements. Subsequently, the retardance, transmission, and laser resistance of the coatings will be assessed.

1. Analysis of a design fabricated by GLAD capable of inducing a phase retardation on the polarization

As a quick reminder of Chapter 1, the specifications for the GLAD coatings are: to have the optical function of a quarter-wave plate at 351 nm, to have a transmission higher than 99 %, and to have a LIDT higher than 14 J/cm² for a pulse length of 3 ns.

We decided to study silica-based multilayer QWPs designed and fabricated by the LLE [26]. By studying these samples from the state of the art, this chapter provides a comprehensive introduction to the analysis of the optical properties of QWPs based on the properties of its constituent layers, in relation to their morphologies and compositions. This methodology will enable the understanding of the effects of aging and contamination on the structural and optical properties of these QWPs, as presented in the following chapter. Finally, I will also present an example of the study of laser resistance of such QWPs.

1.1. Description of the studied silica GLAD samples

The QWP samples are 21-layer coatings composed of alternating 10 anisotropic and 10 isotropic layers with an antireflective layer on top. This design was proposed and published by S. MacNally *et al.* [26] from the Laboratory for Laser Energetics (LLE) in Rochester, United States. Moreover, since retardance was 20-25% lower in vacuum than in ambient air, and retardance increased by about 24% over five months [22], a 31-layer coating was designed for vacuum use. However, this chapter will only discuss the 21-layer coating.

The anisotropic single layers were deposited at α ± 73°, and their purpose was to introduce a retardation between two orthogonal polarizations. The isotropic denser layers were deposited at α = 0° and were added for the mechanical strength of the multilayer and to prevent the coalescence of the anisotropic layers when their thickness exceeded 400 nm [25]. The last layer was an antireflective layer, deposited at α ± 82°. The anisotropic and antireflective layers were coated with SBD algorithm (± α every 6 s at 180 °/s).

Thanks to a collaboration with the LLE, many samples have been provided specifically for this project. Most of these samples were fabricated by Daniel Sadowski and Sara MacNally during my three visits there. They are summarized in Table 5.

Table 5. Different silica GLAD sample provided by the LLE.

	Design of the coating	Substrate	Theoretical physical thickness
Single anisotropic layer	Substrate/**4B**/Air	- Silicon - Silica	272 nm
Single isotropic layer	Substrate/**I**/Air	- Silicon - Silica	60 nm
Bilayer (BL)	Substrate/**4B**/**I**/Air	- Silicon - Silica	332 nm
QWP multilayer	Substrate/$\mathbf{(4B/I)^{10}/AR}$/Air	- Silicon - Silica	3 392 nm

B is for birefringent layer also called anisotropic layer. I is for the isotropic layer. AR is for antireflective layer. B, I and AR have a quarter-wave optical thickness at 351 nm. As a consequence, 4B means a full-wave optical thickness. For the anisotropic layer (B), an average of the in-plane indices, n_x and n_y, is being considered for the calculation of the optical thickness. Coatings were deposited on silicon substrates for the purpose of SEM and FTIR analysis. In fact, silicon is more convenient to cleave than fused silica when only small parts are needed. Moreover, silicon is transparent in the infrared, which makes it useful for FTIR. The fabrication details have been presented in the Chapter 2.

To thoroughly examine the microstructure of the multilayer QWP, its elementary layers were observed. Figure 31 presents SEM images of one anisotropic single layer from the top (Figure 31(a)) and from the cross-section (Figure 31(b)). The crackle effect visible in Figure 31(b) is due to the platinum metallization.

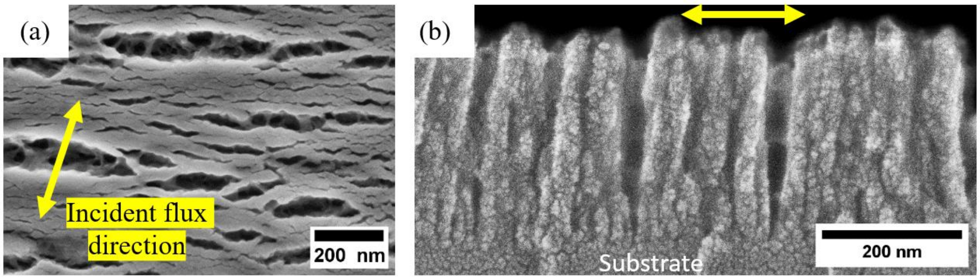

Figure 31. SEM images of the anisotropic single layer. (a) Top view. (b) Cross-section. Yellow arrows illustrate the orientation of the fast axis.

From the top of the film (Figure 31(a)), large pores are observed all oriented along the direction of the expanding of the columns. In Figure 31(b), columns perpendicular to the substrate are visible, with pores in between. Columns' width is around 20 nm to 40 nm. However, discerning only one single column is not straightforward. Some researchers have observed a gradual increase in the diameter of the columns [25]. This phenomenon is, again, not easily quantifiable. Additionally, broadening is not obvious to observe from the cross-section. The cross-section (Figure 31(b)) reveals columns with different lengths that might come from the nucleation phase, where nucleation sites can vary in size and therefore in column length. It could result in a possible rough surface. The thickness of the anisotropic layer is around the expected thickness of 272 nm.

Figure 32 presents SEM images of a bilayer, viewed (a) from the top and (b) from the cross-section. As observed with the two following images, the isotropic denser layer when deposited on top of the anisotropic columnar layer, penetrates into the open pores creating a rougher surface than a "classical" e-beam layer would. This penetration impacts the indices and then the retardance.

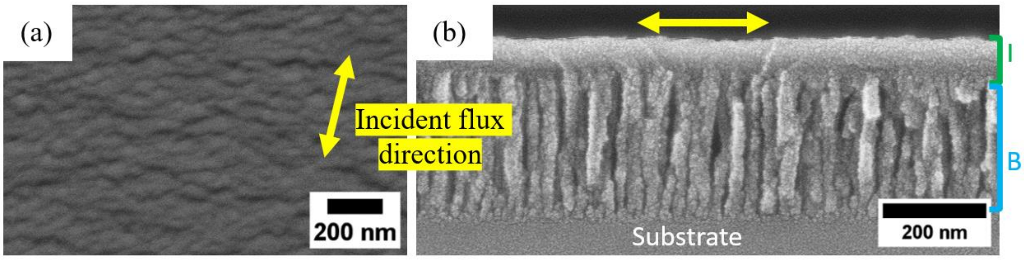

Figure 32. SEM images of a bilayer (Substrate/B/I/air). (a) Top view. (b) Cross-section. Yellow arrows illustrate the orientation of the fast axis. B is for birefringent layer and I is for isotropic layer.

Figure 33 presents three SEM images of the silica QWP coating. Figure 33(a) is a cross-section image of the entire QWP. Figure 33(b) is a top view image of the QWP coating. Figure 33(c) is a cross-section image taken at an angle that allows one to see the two coating orientations: incoming flux direction and perpendicular to that direction.

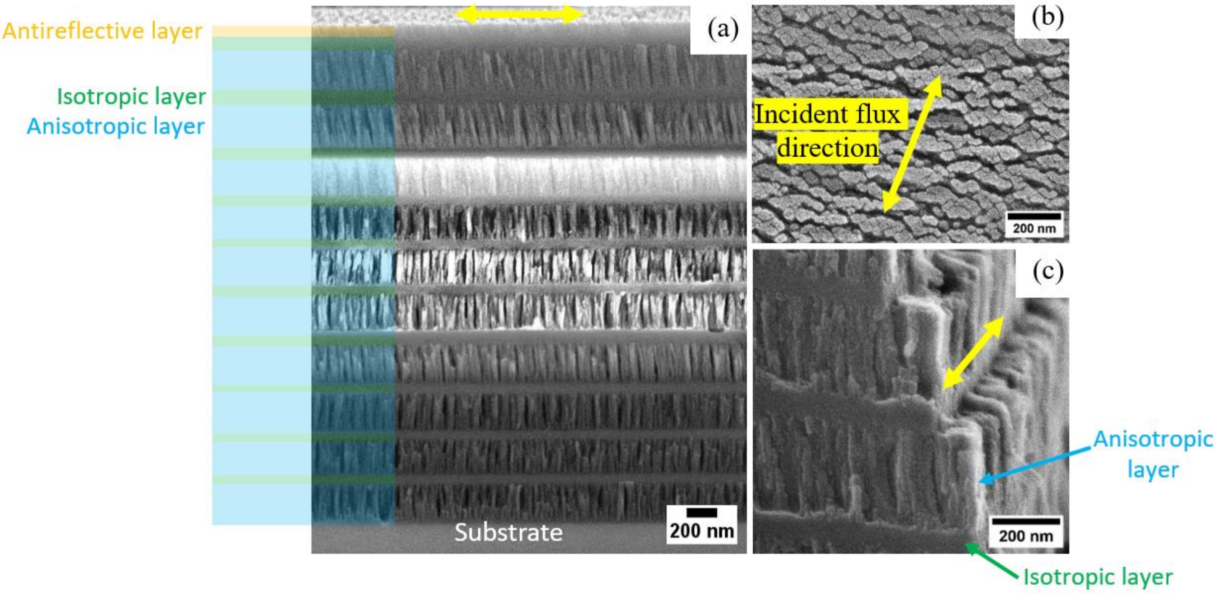

Figure 33. SEM images of the silica QWP. (a) Cross-section image of the 21 layers of the silica QWP. (b) Top view image. (c) Cross-section image. Anisotropic layers are in blue. Isotropic layers are in green. The antireflective layer is in yellow.

In order to better observe the columns, the cross-section of the entire QWP was taken parallel to the incoming flux. The alternating layers of anisotropic (blue) and isotropic (green) silica along with the AR layer (orange) are visible in Figure 33. The interfaces between the anisotropic and isotropic layers are well defined. Regarding the thicknesses, the first anisotropic layers seem to be thinner than expected, around 230-250 nm, for an expected thickness of 272 nm.
The last three layers seem to have the expected thickness. In contrast, the thicknesses of the isotropic layers are all around 60 nm. The perpendicular anisotropic columns have a width of around 20 nm. Between the columns, large voids that can have the size of one column are observed. Some columns growth seems to have been stopped. Indeed, as outlined in Chapter 2, the initial growth involves a nucleation phase in which larger nucleation sites might grow long columns at the expense of smaller nucleation sites.
On the top view of the QWP coating, shown in Figure 33(b), elongated structures separated by large pores are observed. They are oriented along the same direction which is perpendicular to the orientation of the incoming SiO_2 plume. The incident flux was parallel to the yellow arrows, therefore promoting shadowing in the orthogonal direction.

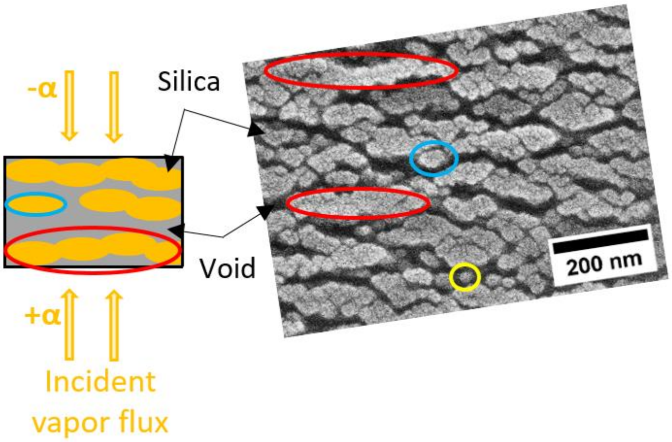

Figure 34. Highlighting of the ellipsoid cross-section of columns and the merging of the columns with a schematic representing the top SEM image from a QWP sample.

As observed in Figure 34, which is the top view of the QWP, some columns seem to be separated from the others (in blue) and some are merged (in red). Structures generally have an ellipsoidal cross-section, though few columns appear to be circular (see yellow circle in Figure 34). However, it should be noted that in top view, the AR layer, which is approximately 70 nm thick on top of an isotropic layer, may mask the known ellipsoidal shape of the columns.

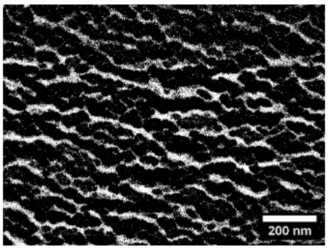

Figure 35. SEM image of the surface of the QWP binarized. Black is silica and white is void.

By binarizing the top surface image of the QWP, which means the top surface of the AR layer, (Figure 35), the percentage of open pores was estimated at around 15-20 %. In addition to this porosity, a microporosity within the silica matrix is also expected [85], [89], [90].

1.2. Composition profile of the silica QWP

Because the QWPs are highly porous, the ingress of water and/or molecular contaminants into this porosity can alter the optical properties. Glow Discharge Optical Emission Spectrometry (GD-OES) was performed to access a concentration profile of the entire 3.4 µm depth of the QWP (Figure 36).

The measurement details are in Chapter 2 but as a reminder, the intensities of the reported species are non-quantitative. Intensities were normalized and laid out with an offset to separate the curves and make them more visible. Four elements were measured, silicon in yellow, oxygen in red, hydrogen in green and carbon in pink.

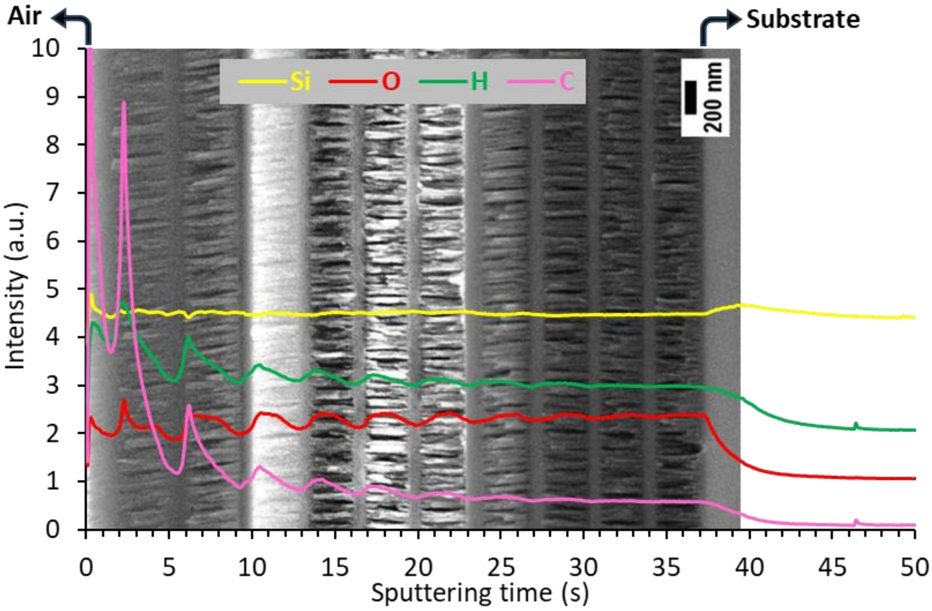

Figure 36. GD-OES profile superposed on the corresponding SEM image of the silica QWP.

The Si signal is constant throughout the depth of the multilayer sample as opposed to the three other species. The variations of the emission signal associated with the other species as a function of the ablation time can be compared to the spatial variations of the microstructure observed on the cross-section SEM image of the sample. This is presented as a superposition of the SEM image with the composition profile as presented in Figure 36.

The correspondence between the composition profile and the SEM image is dependent on where the substrate is believed to start. To construct Figure 36, I hypothesized that the substrate started at the sharp drop in the oxygen content at around 37.5 s, as some researchers suggested [91]. However, because of the development of a rough interface during the ablation process, this location is not obvious. The mid-height slope, around 39 s, could also be the starting point of the substrate [92], [93]. The hole generated by the measurement, after 50 s of ablation, was characterized using a profilometer. It was flat with a depth of 3.96 µm. As a comparison, the thickness obtained from ellipsometry measurements was 3.59 µm. The profilometry confirmed that substrate was reached.

For both positions of the substrate, the conclusions remain the same: an evolution of the quantity of O, H and C can be observed through the depth of the sample in relation with its microstructure. The concentrations of oxygen, hydrogen and carbon evolve almost cyclically with a decreasing amplitude of the variations up to 31 seconds and become a flat signal until the substrate is reached. In Figure 36, the higher oxygen, hydrogen and carbon intensities correspond to the anisotropic columnar layers. At the surface of the sample, there are high C and H concentrations. The C and H profile modulations decrease by moving forward into the depth of the coating. As for the O, the intensities are higher in the anisotropic columnar layers.

These observations suggest that there is contamination from the ambient atmosphere in the columnar layers and to a lesser extent in the denser layers. The carbon contamination near the surface is common in porous coatings [25]. The intensity of the elements in the substrate can be used as a reference: this shows that the contamination occurs in the full QWP. The reduction of the amplitude variations in the composition profile originate partly in the roughening of the surface during the GD-OES ablation process [91]. Another potential cause could be the aging of the sample; the carbon and moisture may require more time to reach the deeper layers. The water ingress, associated with the presence of H was expected. The presence of C however suggests that hydrocarbon contaminants can also affect the QWP, as we will see in Chapter 4.

1.3. Characterization of the silica matrix using IR spectroscopies

In addition to the spatial information provided by the GD-OES, characterizing the silica matrix thanks to FTIR spectroscopy and Raman spectroscopy provides data on the molecular structure formed within the silica matrix. The samples investigated here were the samples deposited onto silicon substrates.

Figure 37 shows FTIR spectra of the single anisotropic layer (green), the single isotropic layer (purple), the bilayer (orange) and the multilayer QWP (blue). The characteristic bands of silica are observed such as the Si-O-Si rocking, bending and stretching bands at around, 465 cm^{-1}, 800 cm^{-1} and 1080 cm^{-1} [94] - [96], respectively. The Si-O-Si bond is called siloxane. The intensity differences between the single layers, the bilayer and the multilayer are partly an effect of thickness especially on the Si-O-Si band around 1080 cm^{-1}.

For the same percentage of porosity, increasing the thickness shifts the maximum of this band to larger wavenumber, in that case from 1080 cm^{-1} to 1105 cm^{-1}, expands the width and flattens the shape of this band to yield a stopband (Reststrahlen effect). However, even considering the Reststrahlen effect, it seems that there is the emergence of another contribution at around 1190 cm^{-1}. This could be a contribution of carbon such as the Si-CH$_3$ bending mode [97] or the vibration of CH$_3$ [98], reported respectively at 1200 cm^{-1} and 1176 cm^{-1}.

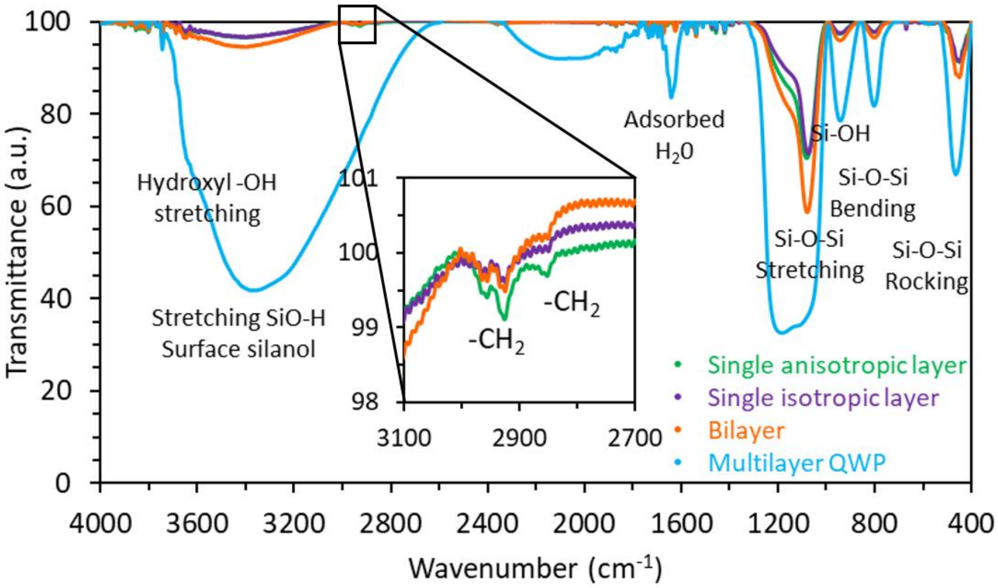

Figure 37. FTIR spectra of all the layer comprising of the QWP silica multilayer: the single anisotropic layer (green), the single isotropic layer (purple), the bilayer (orange) and the QWP multilayer (blue). Insert is a zoom on carbon related bonds between 3100 and 2700 cm^{-1}.

In Figure 37, different water-related bonds are also visible: around 950 cm^{-1}, 1640 cm^{-1}, and 3000-3700 cm^{-1} [89], [94], [99]. The presence of these bonds is expected. After venting the porous coating of the QWP, chemisorption of water onto the surface of the matrix takes place. The water then reacts with the strained siloxane bonds in a process called hydroxylation. This reaction forms silanol bonds (Si-OH) by breaking strained Si-O-Si bridges. This process locally relaxes the silica matrix. The siloxanes are arranged in rings. Small rings (3-4 Si-O members) are highly strained, particularly in evaporated silica, and more susceptible to hydroxylation. The reverse reaction, dehydroxylation, only occurs at temperatures higher than 200°C, making hydroxylation effectively irreversible under ambient conditions. We see in Figure 37 the characteristic band centered at 3500 cm^{-1} even for a single dense layer. The hydroxylated surface then creates favorable sites for the physisorption of water.

The affinity of silanols with water depends on their structure [100]: terminal or unbound, closed silanols have a high affinity, whereas simple, isolated silanols have a low affinity. The resulting hydrogen bonds are weak yet persistent under ambient conditions. This can be seen with the H_2O band around 1600 cm^{-1} present in the QWP. This H_2O band may have already been present in the single and bilayers, but probably too small to be observed in FTIR spectroscopy. These observations agree with the GD-OES measurements shown in Figure 36. Additionally, as observed in the insert, the modes of the -CH_2 group were detected around 2850 cm^{-1} and 2930 cm^{-1} but only for the single layers and the bilayer. These bands are not observed for the multilayer. It is likely that the large water-related bond serves to mask them. To investigate further this point, I have performed Raman spectroscopy measurements.

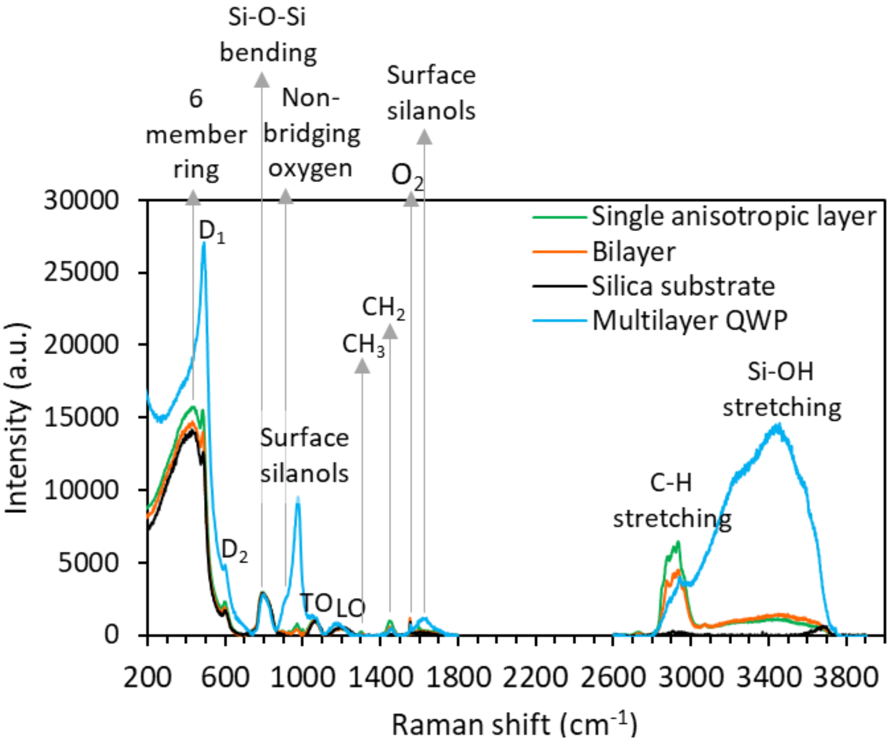

Figure 38. Raman spectra of GLAD coatings in silica: a single anisotropic layer (in green), a bilayer (in orange), the silica substrate and the multilayer QWP.

Figure 38 shows the Raman spectra of the anisotropic single layer (in green), the bilayer (in orange), the multilayer QWP (in blue) and the corresponding bare substrate (in black). The spectra were readjusted with the Si-O-Si bending mode around 800 cm^{-1} after a background baseline was removed. The three first bands at around 420-430 cm^{-1}, 490-515 cm^{-1} and 580-600 cm^{-1}, are assigned to siloxane. The first band is for six-membered rings, D_1 is for the four-membered rings and D_2 is for three-membered rings [96], [101] - [104].

For the bilayer and the single anisotropic layer, the amount of six-membered-rings and four-membered-rings seems to be similar to those observed in the silica substrate. On the other hand, the number of four-membered rings is larger for the multilayer. This suggests that the siloxane rings are stressed which would favor hydroxylation. This is in agreement with the large silanol bands near 1600 cm^{-1} and 3500 cm^{-1} observed in FTIR. Having a large presence of surface silanols predicts that water will adsorb later on, on the surface, and that the matrix will probably still evolve. This can induce an evolution of the optical properties of the component over long periods of time, as already observed by S. MacNally *et al.*, with a 24 % retardance increase over 5 months [26]. This will be the topic of the next chapter. In the Raman spectra, C-H bonds of different species were observed in all the evaporated films at around 1280 cm^{-1}, 1460 cm^{-1} and the large band at 2830-3000 cm^{-1}. They most likely arise from contamination from hydrocarbons found in the ambient atmosphere.

These results, together with the observation made in GD-OES, show the porous QWP is susceptible to permeating volatile species present in their environment, most commonly moisture and hydrocarbons in a laboratory. GD-OES suggests that the ingress would concern the full device thickness. Now that we have a good understanding of the microstructure of the films and their composition, we can analyze their optical properties.

2. Study of the silica QWP to induce a phase retardation in transmission and at high laser fluence

The main characteristics required for the use of a QWP to smooth the intensity profile of the laser beams of the LMJ are: a retardance of quarter-wave at 351 nm ($\lambda/4 = 87.75$ nm), a transmission higher than 99 % and a laser induced damage threshold higher than 14 J/cm² for a 3 ns laser pulse. In this section, the retardance of the films obtained with GLAD through modeling ellipsometric measurements will be analyzed. Transmission measurements will be provided to characterize the value of the transmission at 351 nm. Then, an analysis of the laser resistance of the QWP will be characterized.

2.1. Relationship between microstructure and anisotropy

The optical behavior of anisotropic films can be characterized using the Mueller matrix. This matrix was measured using the ellipsometer described in Chapter 2.

As a reminder, the samples were measured in transmission from the silica substrates in the 210 to 1690 nm range. The measurements were performed for several azimuthal angles: 0° (fast axis vertical), 45° and 90° (slow axis vertical). The retardance of the studied GLAD QWP should be the sum of the retardance of each anisotropic columnar layer. For a comprehensive study on the optical properties, I started the analysis with the single anisotropic layer, the bilayer and finally the multilayer QWP.

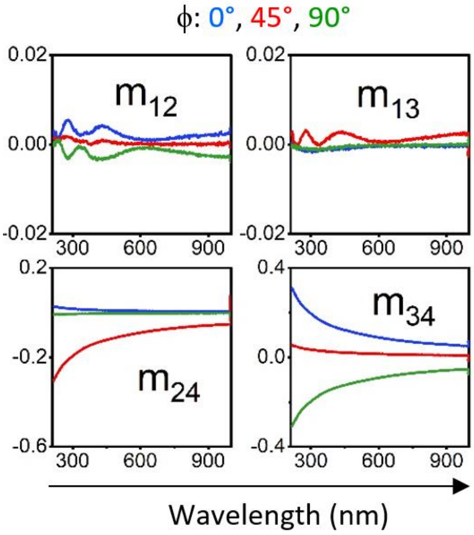

Figure 39. Four MM elements of the single anisotropic layer made of silica at ± 73°.

The main optical characteristics of a columnar layer in terms of linear retardation can be evidenced by inspecting a few Mueller matrix elements. Figure 39 presents four MM elements of the single anisotropic layer deposited at ± 73°. This subset of the measured Mueller matrix gives us qualitative information about the optical properties of this film. As previously discussed in Chapter 2, m_{12} and m_{13} are the linear dichroism at 0° and 45°, respectively. The dichroism values are small, which means that there is no absorption. However, they are not zero, which suggests that the samples have transmission losses.

Moreover, for m_{12}, the only measurement that is 0 is the measurement at 45°, whereas for m_{13}, it is the elements at 0° and 90°. This is consistent with the fact that the optical axes follow the axes of symmetry of the column cross-section in the (x,y) plane.

At 45°, both horizontal and vertical polarizations see the same microstructure from m_{12}, hence the absence of birefringence and dichroism, while the contrast is maximum for polarizations at ± 45° (m_{13}). Looking at m_{12} at 0°, $m_{12} > 0$, which means that the reflection is higher in that direction, and that the lower index (fast axis) is vertical, as proposed in Chapter 2, Section 2.2. As expected, the effect is reversed at 90°.

The elements m_{34} and m_{24} are the linear birefringence at 0° and 45°, respectively. Their values can be high. For m_{24}, associated with m_{13}, the only measurement not at 0 is the one at 45°, which confirms the observation about the optical axis regarding the columns. For m_{34}, the results of measurements at 0° and 90° are opposed, which tell us that there is a symmetry of column sections in the (x,y) plane.

To extract the optical properties from the measured MM, a model was built using the CompleteEASE software (J.A. Woollam) and fitted to the measured MM. Figure 40 presents the construction of the model built for the single anisotropic layer and the extraction of some results illustrated with the index ellipsoid.

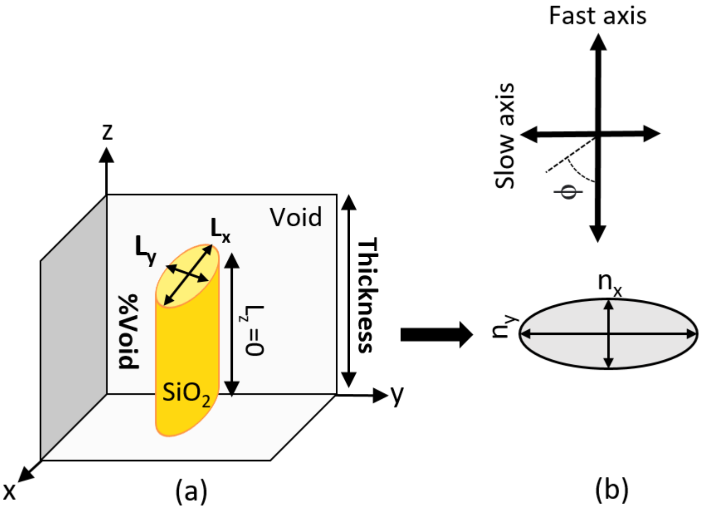

Figure 40. (a) Schematic of the CompleteEASE model to simulate the optical properties of the single anisotropic layer using the depolarization factors. (b) Index ellipsoid viewed along z, resultant of the fit.

The model utilizes two materials: silica and void mixed using the Anisotropic Bruggeman Effective medium approximation. The optical anisotropy is modeled by the shape of the GLAD columns using a depolarization factor L.

As outlined in Chapter 2, CompleteEASE describes the depolarization split D_{xy} rather than the depolarization factors directly. Here, $L_z = 0$, $L_x = D_{xy}$ and $L_y = 1 - L_x$. Finally, the Euler angle, Phi, is used to adjust the optical axes of the sample to the ellipsometer frame of reference.

In the schematics presented in Figure 40 and Figure 41(a), the void fraction is constant throughout the layer. However, in reality the amount of void may vary within the depth as seen in the cross-section image of Figure 41(b), being less important close to the substrate than to the air.

Additionally, the single anisotropic layers present obvious roughness (Figure 41(c)). To be as close as possible to reality, three model configurations were tested (Figure 41) and called, “simple” model (a), “graded” model (b) and “roughness” model (c), respectively.

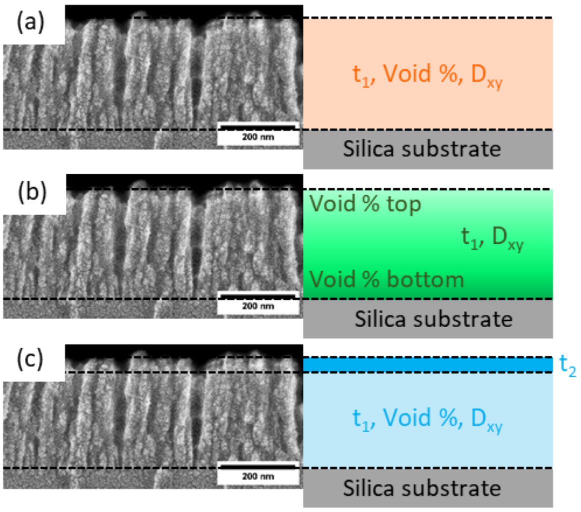

Initial	Adjusted
t_1 = 272 nm Void = 20 % D_{xy} = 0.70	t_1 = 252 ± 3 nm Void = 20 ± 2 % D_{xy} = 0.78 ± 0.02
t_1 = 272 nm Void top = 20 % Void bottom = 20 % D_{xy} = 0.70	t_1 = 263 ± 4 nm Void top = 40 ± 3 % Void bottom = 8.6 ± 1 % D_{xy} = 0.74 ± 0.01
t_1 = 272 nm t_2 = 1 nm Void = 20 % D_{xy} = 0.70	t_1 = 253 ± 3 nm t_2 = 13 ± 5 nm Void = 21 ± 2 % D_{xy} = 0.77 ± 0.02

Figure 41. Three model configurations tested for the single anisotropic layer with the correspondence to a cross-section SEM image. The stated elements are the fitted parameters for (a) “Simple” model (b) “Graded” model (c) “Roughness” model. Table presents starting values of the fit and the adjusted values after the fit.

The three models have the same base as explained above (Figure 40). For the simple model, the thickness (t_1) is fitted as well as the void fraction and the depolarization split. For the graded model, the void fraction is simulated as a 15-step stair with linear variation. The fit results are void fractions; at the bottom and at the top. The roughness model is only the addition of a surface roughness (t_2) limited to a maximum thickness of 50 nm with a concentration of 50 % of void in silica (BEMA). None of the other fitted parameters were bounded. The starting values of thickness, void % and D_{xy} were determined with the analysis of the SEM images (Section 1.1) and are reported in the “Initial” column of Figure 41. The parameters in the subsequent column, “Adjusted”, align closely with expectations for this anisotropic layer.

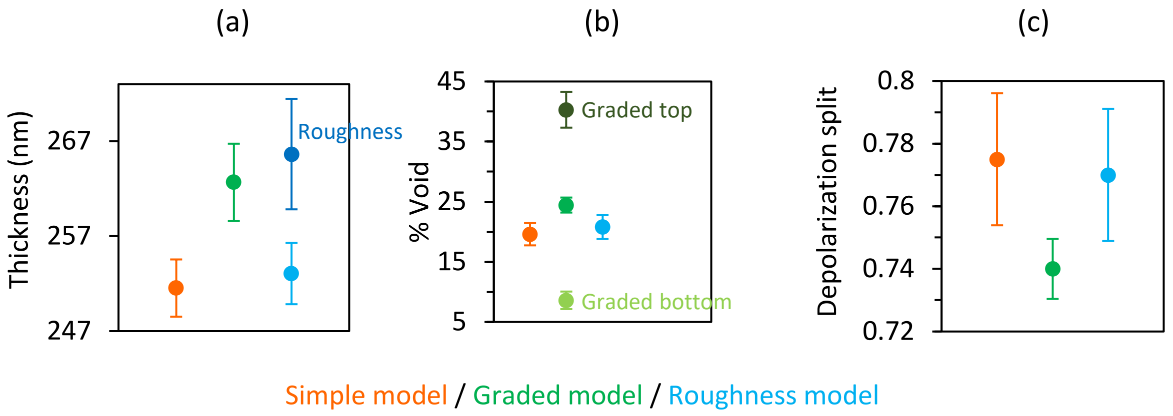

Figure 42. Results of the CompleteEASE fit. Thickness (a), Void percent (b), Depolarization split (c) depending on the model used (Simple, Graded or Roughness).

The mean squared error (MSE) can be used to evaluate the fits and to compare the models. It is the quadratic sum of the differences between the measured data and the modeled data for all the measurement wavelengths and azimuthal angles. An MSE of 4.87 was found for the simple model, an MSE of 4.83 for the graded model and an MSE of 4.87 for the roughness model. There is no significant difference between the MSEs.

Figure 42 shows the details of the fitted parameters: graph (a) is the result of the thickness, (b) the percent void and (c) the depolarization split. In graph (a) there is an additional fourth data for the roughness model: t_1 is reported in light blue as well as $t_1 + t_2$ in dark blue. Graph (b) has five data points; in addition to the data of the simple model and the roughness model; there is the average void fraction of the graded model, the void fraction on the top and on the bottom. The error bars correspond to the 90 % confidence limit in the value parameters obtained from the fitting procedure.

Let's begin the analysis with the thickness (a): The thickness estimated with the simple model is the smallest at 252 ± 3 nm. The total thickness of the rough model is the thickness of the layer $t_1 = 253 \pm 3$ nm added to the thickness of the roughness layer $t_2 = 13 \pm 5$ nm. The thickness of the graded model and the total thickness of the roughness model are quite similar. For the void fraction, the values of the simple and the roughness models, are similar and not far from the average value of the graded model. For the graded model the void goes from 9 % at the bottom to 40 % at the top. The average void fraction of 20 % compares favorably with the value estimated from the SEM image analysis (Figure 35).

Lastly, two depolarization split values obtained using the simple and the roughness models are quite similar. Nevertheless, all the depolarization split values are in the same order of magnitude.

It should be noted that all the fitted parameters are highly correlated (> 93 %) which limits their independent determination. As a result, only the in-plane refractive index and birefringence were accurately assessed in the fitting procedure. And the main output of interest that should be extracted from the models is the retardance at 351 nm induced by the films.

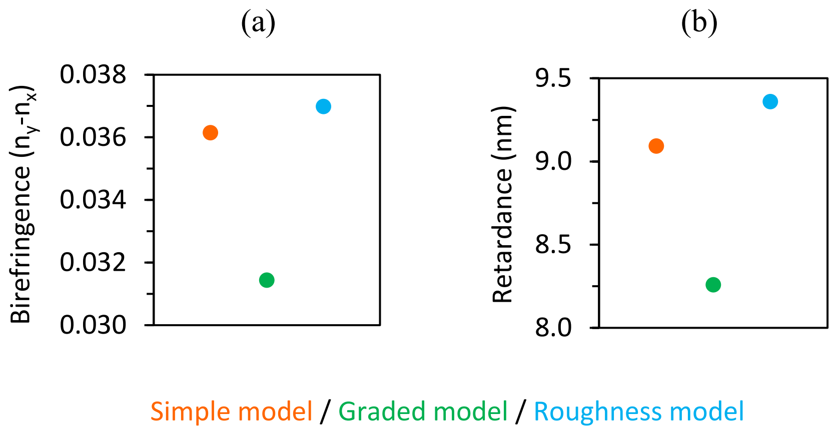

Figure 43. Optical properties extracted from the CompleteEASE fit. (a) Birefringence: $n_y - n_x$. (b) Retardance: $(n_y - n_x) \times T$.

Figure 43 presents the birefringence (a) and the retardance (b) extracted from the fits. The birefringence (at 351 nm) of the simple, graded and roughness models are, respectively, 0.036, 0.031, 0.037. The value of the graded model deviates most. The calculated retardance at 351 nm are, 9.1 nm (simple), 8.3 nm (graded) and 9.4 nm (roughness). The retardance at 355 nm are, respectively, 9.1 nm, 8.2 nm and 9.3 nm. As a comparison, the retardance of the same layer was quantified using the birefringence mapper at 355 nm. The retardance was measured at 9.4 nm at 21 % RH and 9.2 nm in a nitrogen environment. The graded model does not appear to be suitable for estimating the retardance.

To conclude, among the models, the graded model has results of birefringence and retardance that stand from the other models and the retardance measured with the birefringence mapper is the closest to the retardance of the simple model and to the roughness model. However, the fit in CompleteEASE is in the 210-1690 nm range and for the three azimuths, compared to a retardance measurement only at 355 nm.

Regarding the MSE, it is quite similar for all three models. With all these elements, there is no evident better model. With this conclusion, in this instance, **the simple model could be preferred to estimate the characteristics of the anisotropic film.**

Figure 44 is the result of the fit between the measured MM (full lines) and the simple model (dashed line) for the single anisotropic layer. As indicated by the MSE of 4.87, the overlap is satisfactory, and the model appears to adequately describe the coating.

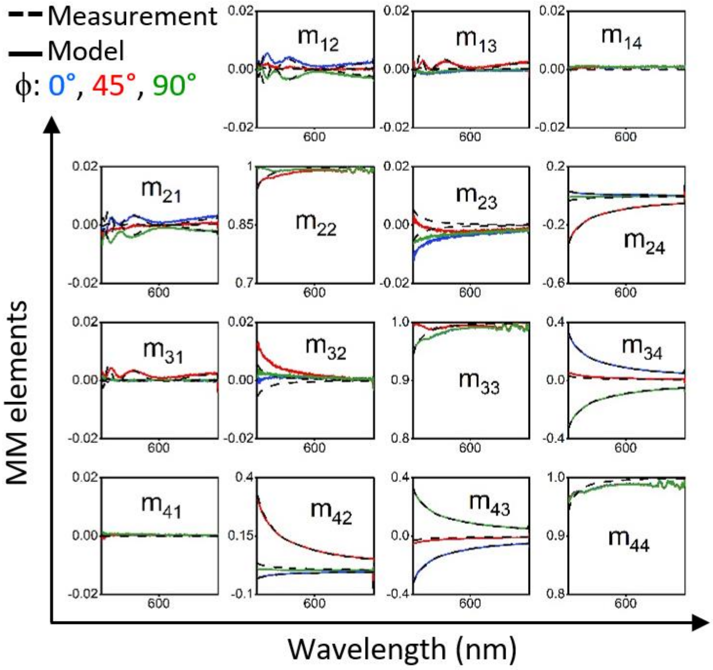

Figure 44. MM elements, measured (full lines) vs CompleteEASE modeled (dashed lines), for one columnar layer deposited at ± 73°. The model used is the “simple” one.

The bilayer was modeled using the same “simple” model along with an additional isotropic silica layer (Figure 45(b)). For the top isotropic layer, only the thickness was fitted. Its refractive index, which comes from an index library, is 1.48 at 351 nm. The study of the bilayer sample revealed a 12 nm decrease in the thickness of the bilayer as well as a decrease of the void fraction by 5.6 %. The depolarization split with the error are close. It is hypothesized that the deposition of the isotropic layer into the anisotropic layer results in the migration of silica molecules into the open voids of the anisotropic layer [105]. The evolution of thickness and % void is accompanied with an evolution of the retardance. The birefringence and the retardance of the bilayer are, at 351 nm, 0.036 and 8.6 (and 8.6 at 355 nm), as compared to 0.036 and 9.1 nm for the single layer. The retardance decreased by around 5 %.

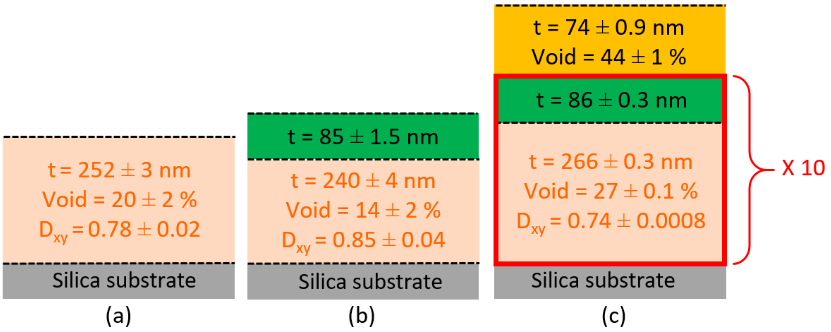

Figure 45. Results of the CompleteEASE model for the single layer (a), the bilayer (b) and the multilayer QWP (c).

With this information we could add an intermix layer between the anisotropic and dense layers. However, it did not improve the adjustment (MSE = 6.3). Moreover, the error bar on the thickness of the intermix layer was larger than the thickness itself.

Using the retardance of 8.6 nm calculated on the bilayer sample, the total thickness necessary to achieve a retardance of 87.75 nm would be 2.45 µm. This could be achieved with 10 anisotropic layers 266 nm thick separated by 86 nm thick isotropic layers, as depicted in the schematic of Figure 45(c). The QWP fabricated was measured by ellipsometry in the same conditions as for the monolayer and the measurements were fitted to a multilayer model. The multilayer model (Figure 45(c)) was designed as a 10 times repetition of the same bilayer structure, inspired from the model obtained for the bilayer sample, along with a porous isotropic last layer for the antireflective layer. The AR layer is modeled as silica and void mixed using the Bruggeman Effective medium approximation (see Chapter 2). Thus, the depolarization factor was kept at $^1/_3$. In this model, the AR layer does not introduce additional retardance. In addition to the bilayer, the adjusted parameters were the thickness of the AR layer and its void fraction. None of the parameters were bounded.

Figure 45(c) presents these fit results of the multilayer with the AR layer with a void fraction of 44 % and a thickness of 74 nm. The multilayer's total thickness was simulated at 3.6 µm, resulting in a total retardance of 101 nm at 351 and 355 nm. This value is the same as the retardance measured with the birefringence mapper, which is 101 ± 0.89 nm at 355 nm. Although, this is higher than the desired retardance of 87.75 nm, it is part of the typical iteration required when developing optical coatings.

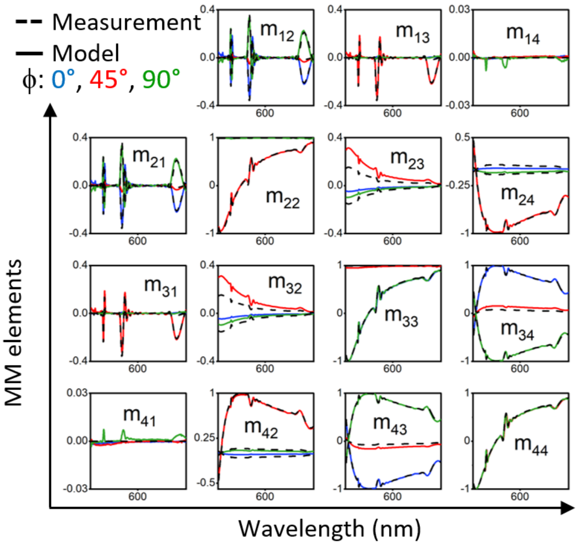

Figure 46. Correspondence between the measured MM elements by the ellipsometer and the model created with the CompleteEASE software, for the multilayer QWP.

Figure 46 presents the correspondence between the measured MM elements obtained using an ellipsometer and the model created using CompleteEASE software for the multilayer QWP. For comparison with the single layer case, the MSE for this fit was found to be 27.1. Evaluating the matrix provides qualitative information about the optical properties of the film. Compared to the MM of the anisotropic single layer (Figure 39 and Figure 44), there are intense oscillations near 300-350 nm, 450-550 nm and 850-1000 nm. The origin of these oscillations can be traced back to interference fringes by calculating the optical response when the thickness of the anisotropic layer is reduced by 16 nm. Figure 47 illustrates this, showing the measured m_{12} (t = 266 nm) in blue and the simulated m_{12} (t = 250 nm) in yellow. The values calculated with a smaller thickness show a downshift of the oscillating signals well in line with the effect expected from interference fringes.

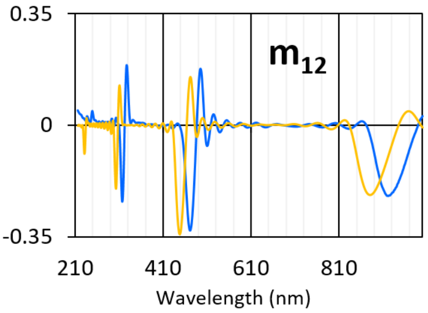

Figure 47. Evolution of m_{12} of the QWP measured at 0°. Blue curve the experimental measurement and yellow curve is a simulation of the QWP design with a lower thickness of the anisotropic layer (t = 250 nm).

2.2. Characterization of the retardance

The target retardance value is important, but so is the homogeneity of retardance across the entire surface of the QWP. This homogeneity was characterized using the birefringence mapper (Chapter 2). Figure 48 presents the retardance maps of the single anisotropic layer and the bilayer measured in the previous sections. The measurements were performed at 355 nm, with a map resolution of 1 mm. The average retardance over the surface (19.6 cm²) of the single layer is 9.2 ± 0.06 nm and 8.6 ± 0.08 nm for the bilayer. The retardance is homogeneous for both coatings. The values are similar to those calculated using the CompleteEASE model, which lends credibility to our model.

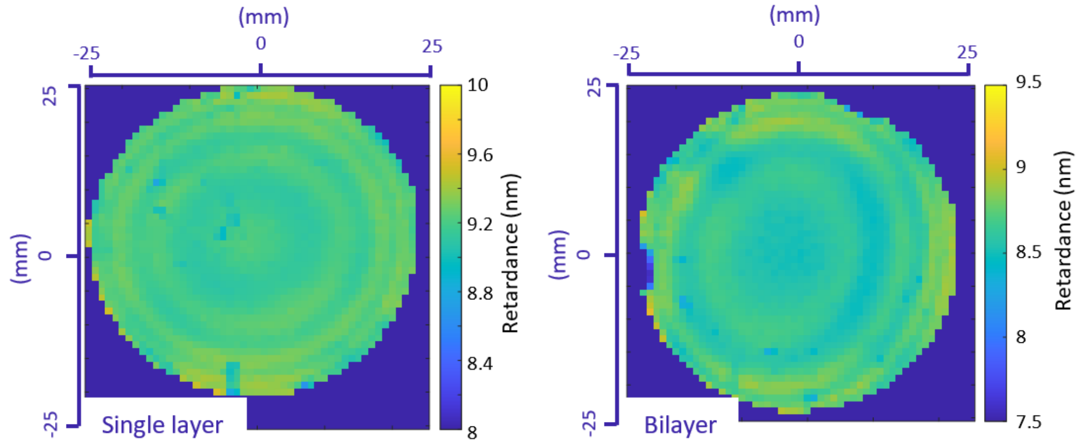

Figure 48. Retardance maps of the single anisotropic coating and the bilayer coating. Samples have a 50-mm diameter. The retardance over the entire surface is 9.2 ± 0.06 nm for the single layer and 8.6 ± 0.08 for the bilayer.

With the aim of evaluating the retardance homogeneity of a multilayered QWP, a new sample was designed and realized on a 100-mm diameter silica substrate. Figure 49 presents the retardance map of this silica QWP over the whole surface. The average retardance over the 78.5 cm² surface of the QWP sample is 90.2 ± 0.40 nm, which is equivalent to λ/3.9. Moreover, the retardance spatial distribution is homogeneous.

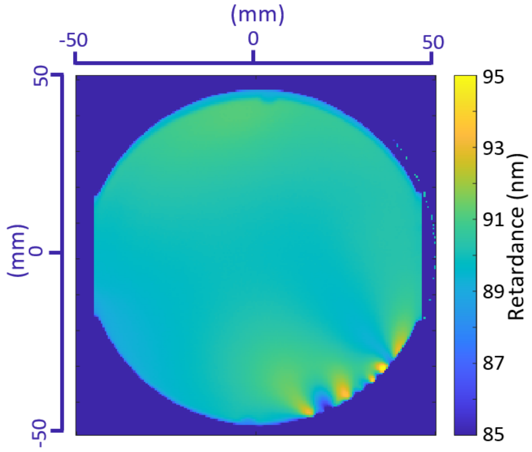

Figure 49. Retardance map of the QWP coating. The retardance was measured with a birefringence mapper at a wavelength of 355 nm, on a 100-mm diameter sample. The retardance is 90.2 nm ± 0.40 nm. This corresponds to a retardance of $\frac{\lambda}{3.9}$.

As a reminder, the target value is $\lambda/4 = 87.75$ nm, although any value going from $\boldsymbol{\lambda/4}$ to $\lambda/2$ (both values included) could be useful. However, the smoothing is more efficient when the polarization is circular as was discussed in Chapter 1. The measured retardance value falls within the specified range. The measurement by the ellipsometer and the birefringence mapper, of a smaller sample, was 101 nm. There is an important gap here. The differences between the target value and the experimental values could result from a retardance deviation over time and/or depending on the environment of use. Indeed, the samples are stored in boxes at ambient air and are known to be sensitive to relative humidity, with an increase in retardance following the relative humidity and an increase in retardance as a function of time [26], [106]. The deviation over time could represent an issue for the application as well as an unknown behavior depending on the environment of use. This point is critical, and I will address it in detail in Chapter 4.

2.3. Characterization of the transmission

As explained earlier, the component must function in transmission because of engineering constraints in the LMJ. The specification for this property is higher than 99 % for the GLAD coating. The optical spectrum of the QWP is presented in Figure 50. It was measured at normal incidence on the fused silica substrate.

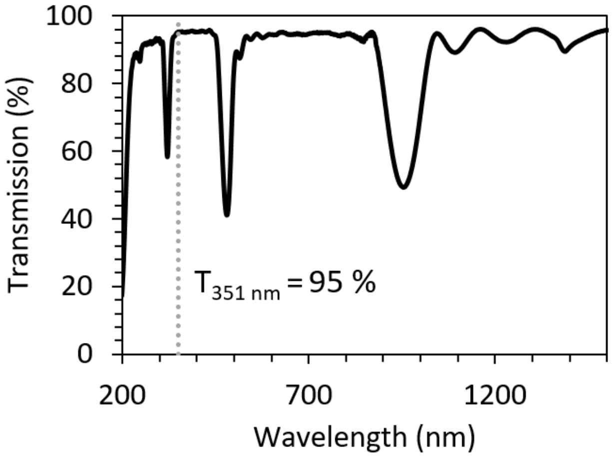

Figure 50. Transmission spectrum of the silica QWP. Grey dashed line is the wavelength of interest for the LMJ application, 351 nm.

At 351 nm, which is the wavelength where the component will be used, the transmission is equal to 95 %. By taking into account the Fresnel reflection of the back side of the substrate, for a refractive index of 1.48 at 351 nm, R = 3.7 %. The comparison between the transmission of the component and the Fresnel reflection evidences a 1.3 % loss. These losses could be explained by some scattering phenomena due to the high roughness of the coating, or could come from the last AR layer, that will require some adjustments. Scattering measurements would help us clarify the cause.

2.4. Characterization of the laser damage resistance

Finally, the last specification to control is the laser damage resistance of the silica GLAD coatings with the fluence conditions similar to the ones of the LMJ. As the position of the component in the LMJ is not determined yet, we have two possibilities: the GLAD coating in the entry side of the laser (called side A) or in the exit side (called side B). To rotate the polarization the fast axis of the component must be at 45°. To characterize the reproducibility, + 45° rotation and - 45° rotation (Figure 51) were tested. Subsequently, four options have been tested.

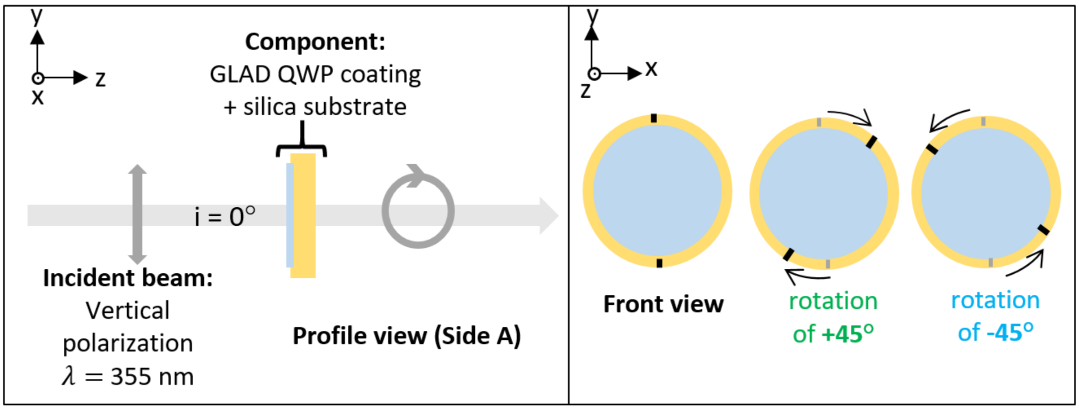

Figure 51. Measurements parameters to characterize the laser damage resistance of the silica QWP GLAD coatings.

As a first determination of the behavior of the GLAD components regarding LIDT, 1-on-1 tests were performed for the four options. The principle of this test as well as the details on the test bed are detailed in Chapter 2. As a summary, the test bed used for this study operates at the wavelength of 355 nm, with a 7 ns pulse length, and an equivalent beam surface of 3.7 x 10^{-3} cm² (686-µm diameter laser). The measurement is at normal incidence with a linear polarization.

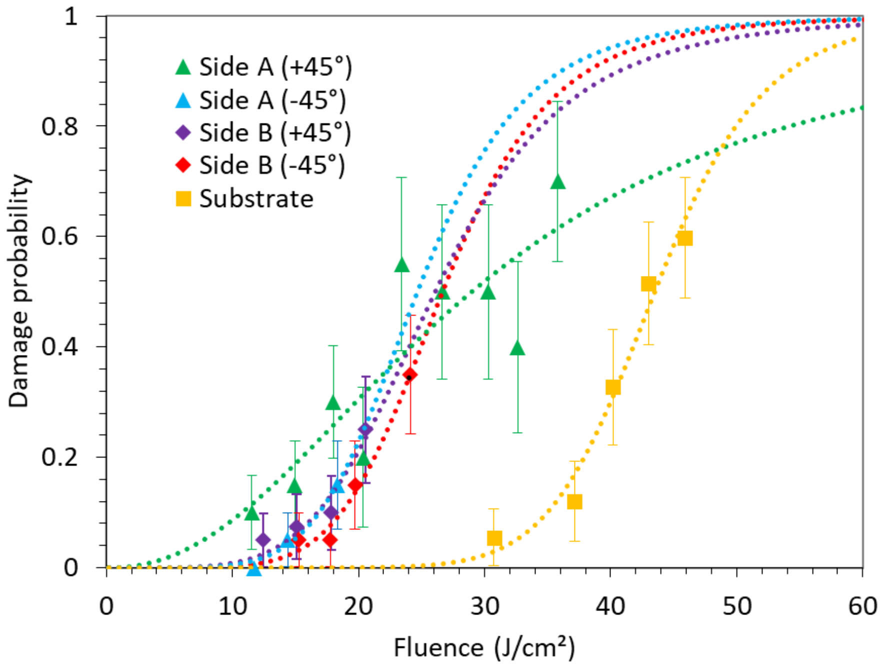

Figure 52. Laser damage resistance of the silica QWP depending on the entry side of the laser into the sample and depending on the orientation of the fast axis. Dashed lines are a fit of the measurement to an empirical sigmoid function. Fluence is given for a 7-ns pulse length.

Figure 52 presents the damage probability as a function of the fluence for the four different sample positions and for the corresponding bare substrate. It can be noted that, for all the configurations, the damage sites were always observed on the coating side. For the silica substrate, the damage sites were on the back side of the component (the exit side of the laser) as expected [55], [56] but at much higher fluences. Together with the experimental results, a damage probability was extracted after fitting each measurement to an empirical sigmoid function. These are represented by the dashed lines in the colors of the experimental data. The damage probability error (vertically) depends on the number of sites that are tested. Twenty sites were tested for each fluence except for the fluences higher than 20 J/cm² for the configuration "Side A + 45°" (green curve). The fluence error (horizontally) is specific for each test bed and is ± 10 % [107]. This error considers the energy and the surface. For clarity, this error was not added on Figure 52 but was added to the summary of the results presented in Table 6. This table summarizes the thresholds for a 5 % and a 25 % damage probability. Comparing all samples with their 25 % damage probability allows for less extrapolation than for a 5 % damage probability. However, 5 % is closer to what is specified for the LMJ.

Table 6. Results of the laser damage resistance tests. Laser functioning at 355 nm, 7 ns and $S_{eq} = 3.7 \times 10^{-3}$ cm². Side A is coating in entry side. Side B is substrate in entry side.

Entry side	**Polarization**	**LIDT at 5 %**	**LIDT at 25 %**
Side A	+ 45°	7.7 ± 0.8 J/cm²	18 ± 1.8 J/cm²
Side A	- 45°	15 ± 1.5 J/cm²	20 ± 2.0 J/cm²
Side B	+ 45°	20 ± 1.9 J/cm²	21 ± 2.1 J/cm²
Side B	- 45°	16 ± 1.7 J/cm²	22 ± 2.2 J/cm²
Substrate		32 ± 3.3 J/cm²	39 ± 3.9 J/cm²

Two groups can be distinguished in Figure 52, the substrate on the right at high fluence and all the curves of the sample grouped on the left at lowest fluence. As expected, the coating is the critical element in the laser damage resistance. Indeed, the damage threshold at 25 % is, for the substrate, 39 J/cm² and for the coatings between 18 J/cm² to 22 J/cm².

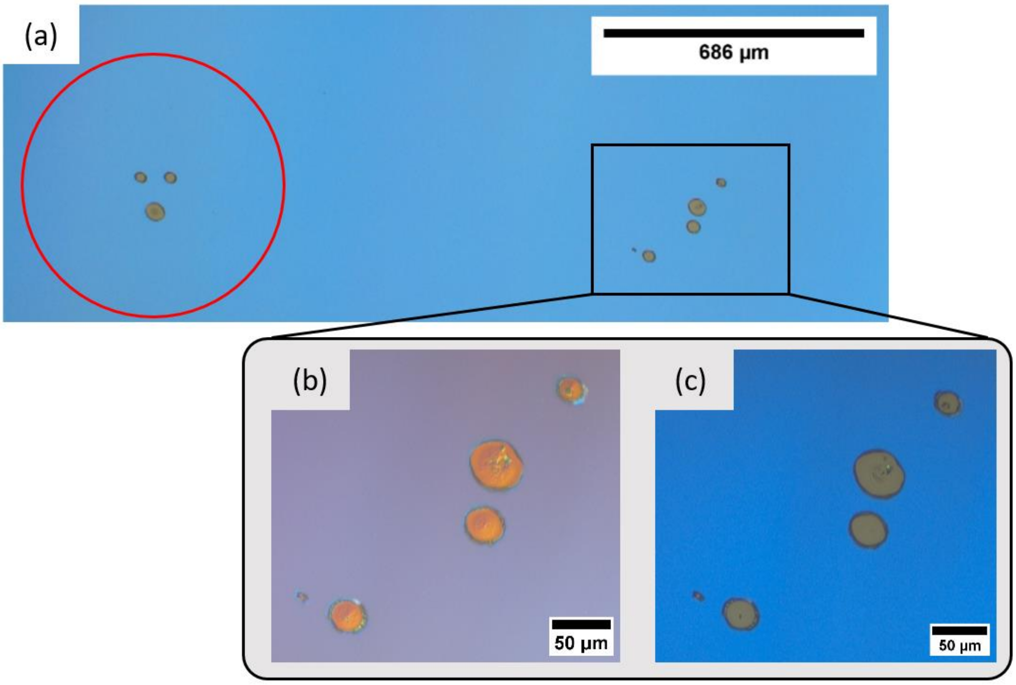

Figure 53. Damage sites observed on the coating after the laser resistance test. (a) Two sites irradiated. The scale represents the diameter of the laser beam, and the red circle is the size of the laser compared to the damage sites. Higher magnification of the right site observed with different contrast in order to better observe the depth and the broken layers: (b) interferential contrast, inducing a phase difference; (c) no contrast.

Figure 53 presents optical microscope images of damage sites on the coating. In Figure 53(a), there are two clusters of dots which are two irradiated zones. The scale is the diameter of the laser beam and the red circle also represents the surface area of the laser. One irradiation produces small damage sites on the coating. The damage sites have a diameter around 25 µm for the small ones and around 50 µm for the larger ones. Figure 53(b) and (c) are a higher magnification of the second irradiated zone. As observed with the interferential contrast image in (b), the damage extends into the depth of the coating. In the no-contrast image (c) different layers are visible in the larger damage. The presence of small dots as opposed to a big damage of the size of the laser may indicate that the defects of the coatings are responsible for this lower LIDT. As outlined in Chapter 1.4, it is common that intrinsic or extrinsic defect of the coating lowers the LIDT [62]. The higher the concentration of defects, the more important the probability is of irradiating a zone containing such defects. However, further characterization is necessary to determine the specific defects responsible.

Finally, by judging the entry side of the laser (Side A or Side B), the coating in the back side of the sample (Side B) seems to be a better configuration. Nevertheless, this observation is not fully conclusive, further characterizations should be performed. In addition, difference in results between polarizations (+ 45° or - 45°) is not straightforward either.

A comment can be made concerning the LIDT with respect to the pulse length. The fluences here are given for the pulse length of 7 ns, however the pulse length of the LMJ is 3 ns. In the nanosecond regime, the damage evolves as a function of τ^{α}, where τ is the pulse length and α is the time-scale law. The detailed calculation between the pulse lengths is expressed by the following equation:

$$F_{ref} = F_{testbed} \times \left(\frac{\tau_{ref}}{\tau_{testbed}}\right)^{\alpha} \tag{21}$$

No time-scale law exists for GLAD silica but for bare fused silica, α is 0.5 [108]. Using the different pulse length between the testbed and the LMJ, the thresholds should be lower by a factor 0.65 for the LMJ laser pulse length.

For a more detailed determination of the LIDT, more tests must be performed, as for example raster scan tests. The latter involves illuminating a large area of the sample with multiple, overlapping laser shots at the same fluence. The advantage of this test is that more surface is irradiated and then it will highlight the cause of the reduced LIDT: punctual defects or an intrinsic property of the coating.

Summary of Chapter 3

This third chapter presented the coating capable of inducing a phase retardation on the polarization of the LMJ laser beam.

The anisotropic layers fabricated by GLAD have ellipsoidal cross-section columns, perpendicular to the substrate and are highly porous in the direction orthogonal to the incoming vapor flux. It appears that the isotropic layers, which are coated between each anisotropic layer, effectively fill in the pores of the anisotropic layers located close to the surface. On top of the multilayer, a highly porous (15-20%) structure is visible, with ellipsoidal columns that merge or stand alone. The multilayer shows presence of C and H within the depth of the coating with a higher concentration in the columnar anisotropic layers. This suggests that the coatings are prone to be infiltrated by volatile species in the ambient atmosphere, with a higher concentration in the columnar layers and, to a lesser extent, in the isotropic denser layers. The analysis of the silica matrix confirmed the formation of bonds with water and carbon. The surface of the GLAD coatings, even for the single isotropic layer, is hydroxylated which represents a favorable surface for the physisorption of water. Additionally, QWPs present a larger amount of four-membered ring siloxanes, which is in a favor of the hydroxylation and probably a variation of the silica matrix over time.

The measurement of the Mueller matrix of the GLAD samples provides both qualitative and quantitative information such as optical axes that follow the symmetry axis of columns in the (x,y) plane. The construction of a model in CompleteEASE allows the extraction of the depolarization split, fraction of void, thickness, indices of refraction, birefringence and retardance. For a single anisotropic layer, there is no clear superior model among a graded void model, a roughness model, and a simple model. Therefore, the simplest model is preferred. It should be noted that, since the fitted parameters are highly correlated, only the birefringence and retardance can be accurately determined. At 351 nm, the birefringence is 0.036, with a retardance of 9.1 nm (also 9.1 nm at 355 nm). This is consistent with measurements taken with the birefringence mapper. The retardance of the bilayer is lower than that of the single layer because the isotropic layer on top of the anisotropic layer is believed to fill a portion of the open pores. The retardance is 8.6 nm at 351 and 355 nm. This is consistent with the measurement of 8.6 nm at 355 nm by the birefringence mapper.

Based on this information, the multilayer was fabricated to have ten times the number of bilayers. However, the experimentally obtained retardance was 101 nm, which is higher than the expected retardance of 87.75 nm. This discrepancy can be attributed to the sample having been stored in ambient air for an extended period, as the 24 % retardance increase observed by S. MacNally *et al* over 5 months [26]. This point is critical and will be discussed further in the next chapter. The transmission, corrected for Fresnel loss of the back surface, is 98.3 %. The remaining 1.3 % loss could be due to scattering phenomena. Laser resistance tests revealed thresholds around 18 J/cm² and 22 J/cm² (1:1 test at 355 nm, 7-ns pulse length and 686-µm diameter laser) depending on the laser's entry side and the rotation of the optical axis (+45° or -45°). The coating on the backside of the component seems to be a better position for a higher resistance. Defects in the coating are believed to be responsible for damage initiation. Converting the pulse length of this test to that of the LMJ, reduces the LIDTs, making them too low.

This comprehensive study of a state-of-the-art sample from the LLE enabled us to understand how such a device functions. While it has interesting optical properties, infiltration of C and H, as well as retardance evolution over time or in different environments, could pose significant challenges for the application. The latter will be the subject of the next chapter.

Chapter 4. Study of the silica wave plate stability over time and in the environments of the LMJ

The aim of Chapter 3 was to study the silica QWPs fabricated using the GLAD technique for the creation of circular polarizations in the LMJ laser beams. We described promising optical properties, namely, a uniform retardance of 90.2 nm on a 100-mm substrate, a transmittance of 95 % at 351 nm and a 25 % probability of damage between 18 J/cm² and 22 J/cm². However, the internal structure of the QWP multilayer showed a highly porous coating that is carbon and water contaminated, and that had also bond defects (Non-Bridging Oxygen for example). The moisture adsorption is already known to impact the retardance [20], [26]. In addition, all these elements may lower the LIDT of the coatings. The previous measurements were performed in ambient air. However, given these conclusions, and the intended locations either in controlled ambient air or in contaminated vacuum, questions arise about the sensitivity and the stability of this coating over time and depending on the environment.

This chapter is divided into two parts. The first section will study the impact of a deliberate contamination in case of a position of the component in the contaminated vacuum of the experiment room. Among the contaminants found in the LMJ target chamber, phthalates were most commonly found. We chose dimethyl phthalate (DMP) as the reference phthalate contaminant. The optical performances of the GLAD devices will be studied in terms of retardance, transmittance, and laser resistance.

The second section will explore an aging accelerating method in case of a position of the component in ambient air, before the vacuum window. The aging accelerating method is based on climate chamber exposition (70°C, 60 % RH). To measure the effect of this experimental method on the aging of the GLAD coatings, the retardance, the refractive indices and the chemical bonds will be investigated.

1. Exploration of the contamination effects of DMP on the silica quarter-wave plates

By positioning the GLAD component after the vacuum window, the component is near the target chamber and exposed to its contaminants. The contamination could impact the optical performance of the silica QWP coatings.

1.1. Implementation of the contamination procedure on the silica QWP coatings

This study was conducted in two times: a contamination procedure at the CEA-Le Ripault (Tours) for the analysis of the transmission and the bonds and a contamination procedure at the Fresnel Institute (Marseille) for the analysis of the laser resistance.

For the analysis of the transmission and the bonds, QWP was contaminated on the silica and silicon substrates by placing the samples in a vacuum chamber (between 2.2 x 10^{-1} and 5.2 x 10^{-1} mbar) for 18 hours, alongside a glass container containing 2 g of liquid DMP (Figure 54 and Figure 55). After the contamination step, air was progressively introduced into the chamber, and the glass container with the remaining DMP was removed.

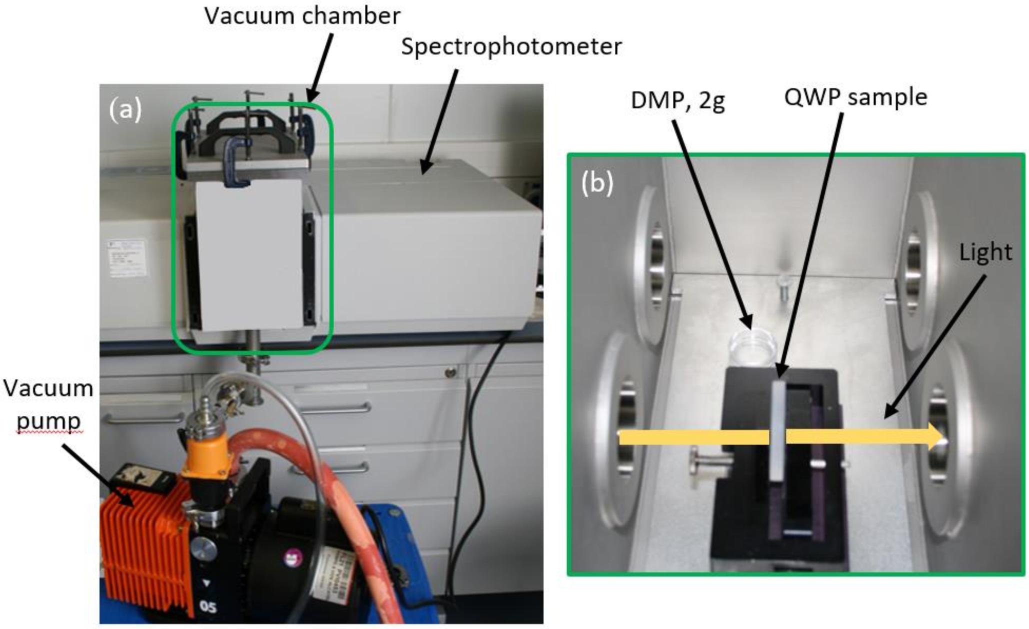

Figure 54. Photo on the contamination setup for the spectrophotometer at the CEA-Le Ripault. (a) Entire setup. (b) Zoom on the inside of the vacuum chamber.

Transmission measurements were performed on the QWP on a glass substrate, in situ, during sorption of the contaminant and after venting during desorption. Figure 54 presents photos of (a) the contamination setup and (b) with a zoom inside the contamination chamber. Spectra were obtained at normal incidence between 200 and 1400 nm, at 1 nm intervals. For the contamination measurements, the contamination chamber was placed inside the sample compartment. Baseline measurements were carried out with the contamination chamber to remove the contribution of the windows.

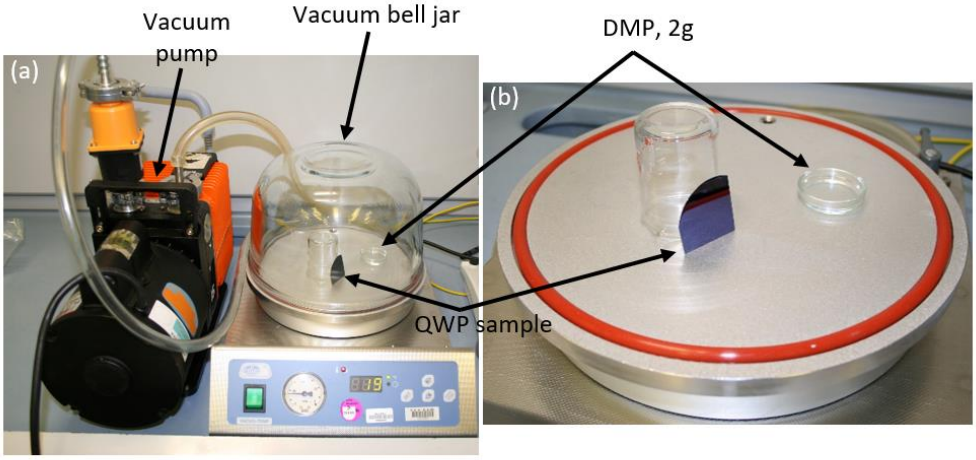

Figure 55. Photo of the contamination procedure of the GLAD coating on a silicon substrate for the FTIR measurements at CEA-Le Ripault. (a) Entire equipment. (b) Zoom on inside de vacuum bell jar.

FTIR measurements were performed on the QWP deposited on the silicon substrate after venting during desorption to identify the bonds present between the 400 and 4000 cm^{-1} range. Figure 55 presents the contamination setup with a zoom inside the vacuum bell jar. We analyzed the long-term evolution of the QWP using Raman spectroscopy measurements. Meanwhile, the samples were placed in non-outgassing boxes made of PolyEthylene Terephthalate Glycol (PETG). The Raman shift was measured from 200 to 4000 cm^{-1} with an excitation at 532 nm. In the meantime, we performed retardance acquisition of the QWP on the glass substrate with a birefringence mapper at 355 nm taking measurements at 0.5-mm intervals.

In a second time, silica QWPs were contaminated, and the impact on the LIDT was analyzed. Three tests were performed in three different environments: air, vacuum, and DMP contaminated vacuum. Then, the tests were performed on one 21-layer coating and two 31-layer coatings on fused silica depending on the environment of the tests. The 21 layers sample would be for a use in the ambient air while the 31 layers sample would be for a use in vacuum. The tests were completed using the testbed of the Fresnel Institute, described in Chapter 2 and Appendix 3, and following a 1:1 procedure with 20 tested sites. The silica QWP was contaminated for around 23 hours in a chamber at a pressure of 6.5 x 10^{-5} mbar and was kept in vacuum during 72 hours at the same pressure. The setup required using 25 mm diameter samples so only one azimuthal orientation was tested, +45 with the coating in the exit face of the laser.

1.2. Highlight of the bonds related to DMP sorption

Figure 56 summarizes the different times for the characterizations performed with FTIR, Raman spectroscopy, spectrophotometer, and birefringence mapper. These time notations will be kept throughout this study.

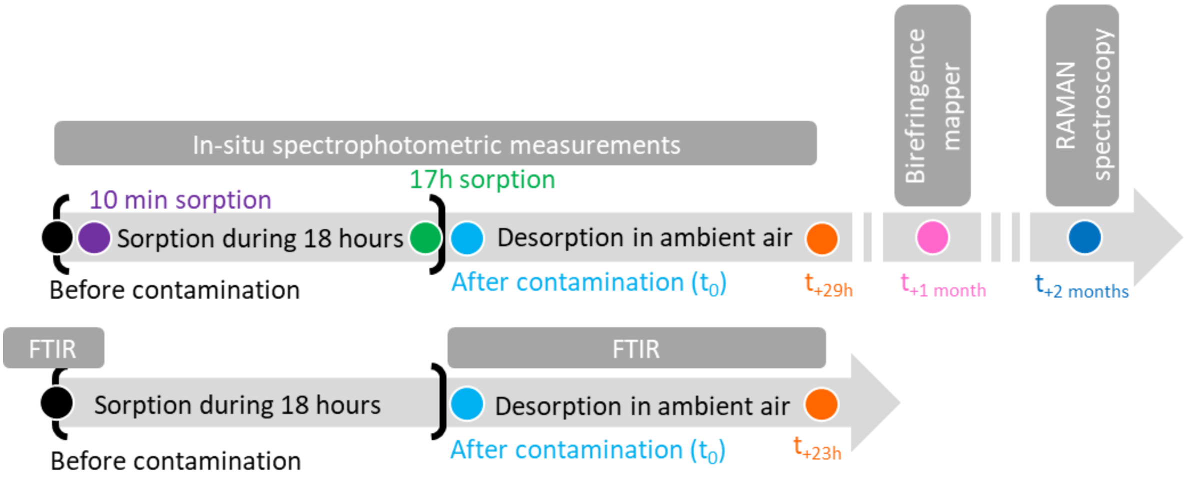

Figure 56. Timeline of the characterizations performed on a silica QWP coatings.

FTIR measurement presented in Figure 57 can inform us on the evolution of the presence of DMP within the QWP upon contamination by analyzing the signature of the molecular bonds.

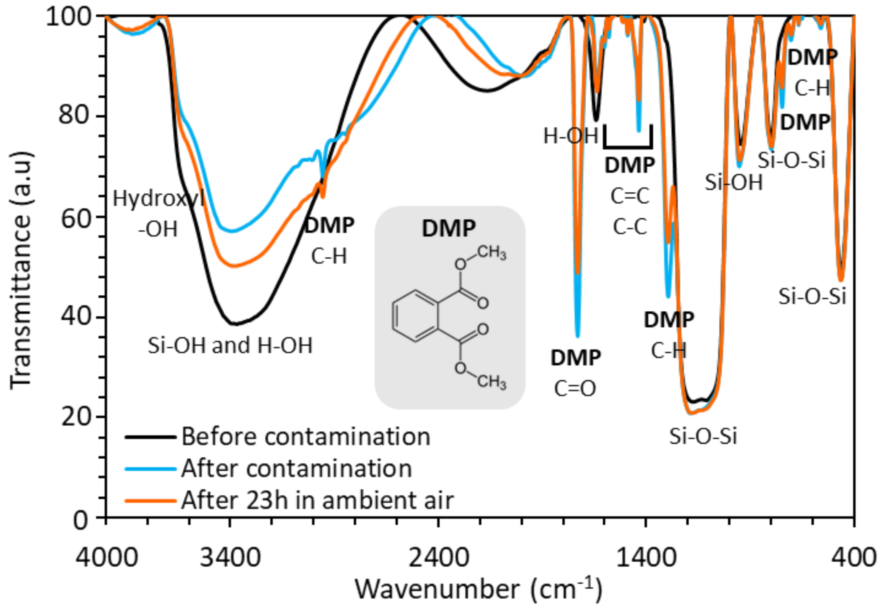

Figure 57. FTIR spectra of a silica QWP, before contamination (black line) right after contamination (blue line) and 23h after contamination (orange line). The molecular structure of DMP is shown in inset.

Before contamination (black line), the characteristic bands of silica are observed such as the Si-O-Si rocking, bending and stretching bands at around, 465 cm^{-1}, 800 cm^{-1} and 1080 cm^{-1} [96], [109], respectively. Different water related bonds are also visible: around 950 cm^{-1}, 1640 cm^{-1}, and 3000-3700 cm^{-1} [89], [94], [99]. The measurements in air just after the contamination step (blue line) and after 23 hours in air exhibit additional absorption bands which can be related to the presence of DMP. Notably characteristic absorption bands are observed around: 520 cm^{-1} (C-H bending), 780 cm^{-1}, 1295 cm^{-1} (C-H bending), 1435 and 1490 cm^{-1} (C=C and C-C aromatic ring), 1730 cm^{-1} (C=O stretching) and 2980 cm^{-1} (C-H stretching) [110]. However, no clear bands associated with Si-O-C groups could be observed. In parallel the bands associated with the O-H groups were reduced as compared to the measurement before contamination. The presence of the characteristic bands of DMP, together with the reduction in the intensity of the Si-OH band, suggests its sorption within the structure of the silica coating. These observations, even after 23 hours in ambient air, seem to confirm that the coating is contaminated for an extended duration.

To further investigate the stability of the contamination over time, Raman spectroscopy was conducted after 2 months of storage in air. The latter is presented in Figure 58 (dark blue line). It can be compared to the spectrum obtained on a QWP which did not undergo a contamination step with DMP (dashed black line).

The non-DMP contaminated silica bands are around 440 cm^{-1}, 495 cm^{-1}, 605 cm^{-1}, 800 cm^{-1}, 980 cm^{-1}, 1070-1200 cm^{-1}, 1460 cm^{-1}, 1620 cm^{-1}, and correspond to ≥ five membered-ring, four membered-ring, three membered-ring, Si-O-Si bending, silanol groups, Si-O-Si stretching, CH_2 and H_2O adsorbed to silanol groups [44], respectively. For the contaminated DMP spectra, the assignment of the bonds relevant to this analysis are directly annotated in Figure 58 [110]-[113]. It can be observed that several carbon-based bonds remain present even after two months in ambient air. There are also intense C-H bonds and, to a lesser extent, C-O bonds. The absorption of DMP appears to be persistent, with a significant number of DMP bands still detectable after two months without any contact with DMP contamination.

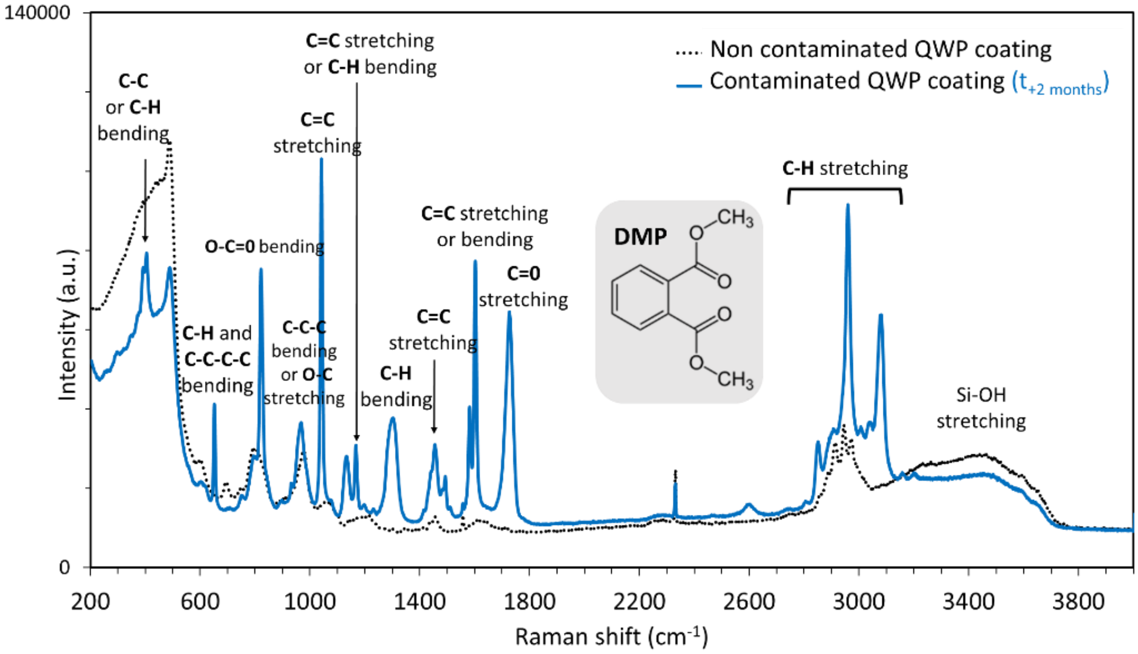

Figure 58. Raman spectra of the DMP contaminated sample after 2 months in ambient air ($t_{+2\ months}$) (dark blue line) compared with a non-contaminated sample (dashed black line). After 2 months, several of the characteristic bands of DMP are still very intense.

The contamination is still bonded to the coating after 2 months and can alter the optical performances of the coatings.

1.3. Exploration of the impact of DMP contamination on the optical properties

Transmission spectra of the silica QWP upon contamination are presented in Figure 59. The wavelength of interest for the LMJ QWP is 351 nm, it is indicated by the gray vertical dashed line. The black spectrum corresponds to the one of the silica QWP prior to contamination. A transmission of 96 % was observed at 351 nm. Transmission dips were observed near 325 nm, 500 nm and 950 nm. They are associated with interference effects in the coating as previously observed in Figure 47 (Chapter 3).

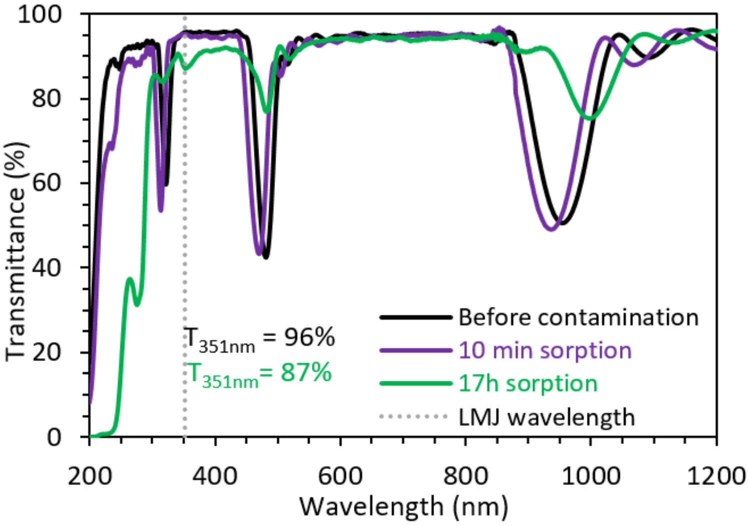

Figure 59. Transmission spectra of silica QWP depending on the environment: before (black line), after 10 min in contact with DMP contamination (purple), and after 17 hours in the presence of DMP contamination (green). The dashed grey line is a guide for the eye corresponding to LMJ wavelength (351 nm).

Ten minutes after initiating the contamination, the spectral features of the transmission spectrum (purple line) were shifted toward shorter wavelengths compared to prior to contamination. However, the transmission at 351 nm remained at the same value of 96 %. The overall shift may merely result from the vacuum conditions inducing an effective refractive indices reduction owing to water desorption [114]. In addition to this phenomenon, in the 200-300 nm range, the transmission was slightly reduced which may indicate the start of the contaminating agent adsorption.

After 17 hours in presence of the DMP contamination environment (green line), the transmission spectrum changed significantly. The features associated with the interferences in the coating were reduced and redshifted. More importantly, a significant decrease of transmission in the UV region was observed. Specifically, at the LMJ wavelength, the transmission dropped from 96 to 87 %. The transmission was completely suppressed between 200 nm and 220 nm and remained low up to 300 nm, enhancing the effect that was seemingly already present already after 10 minutes. The decrease of transmission, associated with absorption in the QWP coating appears to correspond to the presence of the characteristic absorption bands of DMP [115]. The variations of the spectral profile associated with interferences may also be explained by an increase of the average refractive index of the coating together with a reduced index contrast. This would confirm the filling of the porosity with DMP.

The presence of the DMP contamination would be detrimental to the performance of the QWP within the context of the LMJ program: first by reducing the transmission of the silica QWP at 351 nm, second by introducing the absorption associated with DMP which could reduce the LIDT. However, the silica coating exposed to air might be capable of releasing this contaminant from its pores. To determine this, additional transmission measurements were carried out after more than one day after storing the QWP in ambient air as displayed in Figure 59.

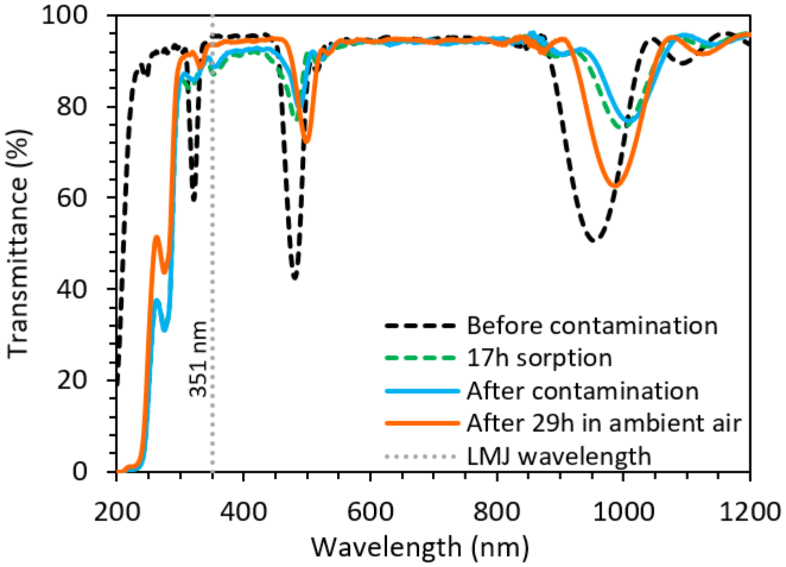

Figure 60. Transmission spectra of silica QWP before (dashed black line), during (green) and after the contamination with DMP just after venting the contamination chamber (blue line) and after 29 hours in ambient air with (orange full line). The dashed grey line is guide for the eye at the LMJ wavelength (351 nm).

The measurements presented previously in Figure 59 corresponding to the QWP before contamination (dashed black line) and after 17 hours in the contamination chamber (green dashed line) are recalled in Figure 60 for comparison. A transmission measurement was performed in ambient air, just after venting the chamber, at the end of the 18-hour contamination step (blue line). Then another one was performed after 29 hours in ambient air (orange line). Different variations in transmission spectra can be observed. The redshift of the features around 500 nm and 950 nm continued between 17 hours and 18 hours of contamination. However, after 29 hours in ambient environment, these features seemed to recover partly the spectral properties observed before contamination (compare orange and black dashed lines in Figure 60). In the UV region, no variation was observed between the measurements in contaminated ambient after 17 hours and just after venting (green dashed and blue lines).

After 29 hours in ambient atmosphere (orange line) the transmission increased, but it was still far from the reference one (black dashed line) and transmission remained close to zero below 225 nm. This is indicative that DMP did not desorb even after 29 hours in air. This suggests that desorption of DMP, and the UV absorption associated with DMP, might be irreversible.

The influence of the contamination on the retardance of the wave plate was determined with a birefringence mapper over the full surface of the samples as presented in Figure 61.

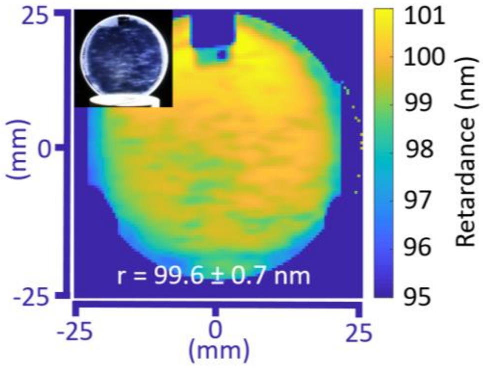

Figure 61. Retardance map at 355 nm of the contaminated silica QWP coating (after one month). The 50-mm diameter sample has an average retardance of 99.6 ± 0.7 nm. The largest retardances are visible in yellow and the lowest in blue. Picture of the same contaminated silica QWP coating (after one day in ambient air).

Figure 61 displays the retardance map at 355 nm of the silica QWP sample exposed to a DMP contamination and stored one month in ambient air. The average value of the retardance was 99.6 nm with a rather large standard deviation of 0.7 nm as compared to what is generally obtained on QWPs realized with GLAD [26], [106]. Without taking the edge effects, the standard deviation was 0.4 nm. More striking were the large local variations of retardance which were also associated with a non-uniform haze on the surface of the sample. Indeed, the features of phase shift variations correspond with the ones noticeable in the visual control of the same sample, in the inset of Figure 61. This picture was taken just one day after the end of DMP contamination. This correlation tends to indicate that firstly, DMP contamination is only partially removed from the coating pores and secondly that the silica QWP is considerably altered by contamination.

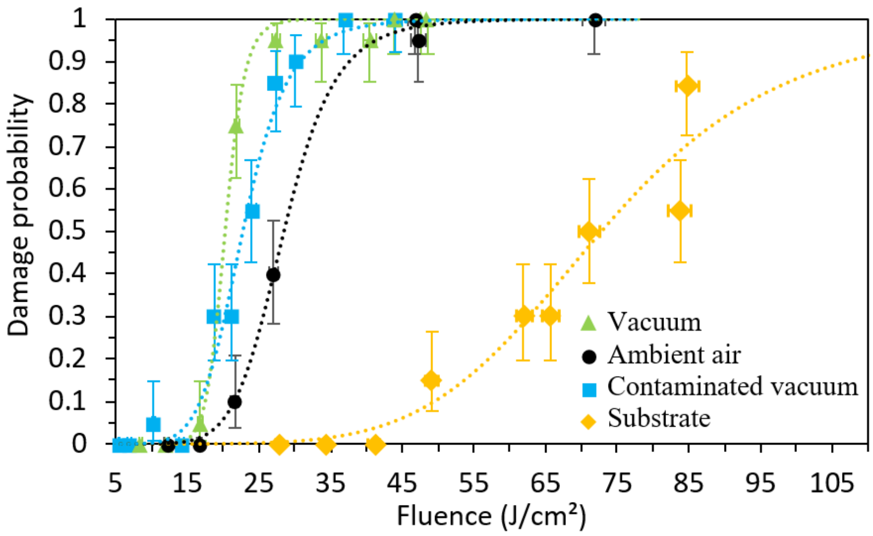

Figure 62. Laser damage resistance of the silica QWP depending on the environment. Dashed lines are a fit between measurement and empirical sigmoid function.

Figure 62 presents the results of the laser damage resistance tests on the silica QWP, depending on the environment as well as the corresponding substrate of the coatings. The dashed lines show the fit of each measurement to an empirical sigmoid function. The damage probabilities are summarized in Table 6 from this fit. In all environments, damages were always observed on the coating side. As described in Chapter 3, the error in the damage probability (vertical axis) depends on the number of sites tested. The fluence error (horizontal axis) is around ± 2.2 %; 2.0 %, 2.3%, and 1.9 % for the tests; in air, vacuum and contaminated vacuum, respectively; and for the substrate. This error considers the energy calculus and the surface. Table 7 summarizes the thresholds for 25 % and 50 % damage probabilities. It should be noted that the laser resistance results presented in Chapter 3 are not comparable to those presented here. Indeed, the testbeds have different parameters: a 7-ns pulse length compared to ps train pulses within a ns window.

Table 7. Results of the laser damage resistance tests depending on the environment. Laser functioning at 355 nm, with ps pulse length train in a ns window and $S_{eq} = 9.3 \times 10^{-5}$ cm²

Sample	Polarization	LIDT at 25 %	LIDT at 50 %
SiO_2 QWP	Ambient air	25 ± 0.5 J/cm²	28 ± 0.6 J/cm²
	Vacuum	19 ± 0.4 J/cm²	20 ± 0.4 J/cm²
	Contaminated vacuum	20 ± 0.4 J/cm²	23 ± 0.5 J/cm²
SiO_2 substrate	Ambient air	60 ± 1.1 J/cm²	73 ± 1.4 J/cm²

As Figure 62 and Table 6 show, the substrate has a significantly higher threshold than the silica coatings. Among the different environments, the ambient air LIDT is slightly higher. The vacuum and contaminated vacuum LIDTs are equivalent, and lower than that of the sample left in the air. The previous results showing absorption in the UV (Figure 60), and the haze effect on the entire surface (Figure 61) do not appear to affect the coating's laser resistance at 355 nm. Given the limited available information, it is difficult to determine the factors that reduce laser resistance in a vacuum environment. As discussed in Chapter 1, this reduction could be attributed to one or several phenomena, such as the evolution of matrix stress.

In summary, it appears that the optimal position for the GLAD device is in air, rather than in a vacuum, regardless of whether it is contaminated or not. However, it is known that the silica matrix evolves in ambient air. Therefore, it is crucial to understand how this evolution changes over time and depending on the environment, which is the focus of the next section.

2. Accelerated aging method for the optical properties of the silica QWPs

As the position of the component is still under consideration, knowing its behavior in both environments is essential. Silica GLAD coatings as well as silica coatings in general, are known to be sensitive to moisture [20], [26], [89], [116]. S. MacNally *et al.* measured a 20-25 % lower retardance in vacuum than in ambient air, as well as an approximate 24 % increase of the retardance over 5 months [26].

2.1. Experimental setup of a stabilization method involving treatment in a climate chamber for the silica quarter-wave plates

The ISO 9022-2:2015 standard [117] ensures the reproducible performance of optical coatings with respect to variations in temperature and/or humidity. Inspired by these tests and the tests performed on silica e-beam coatings [118], [119], an experimental procedure has been designed, and I have performed the characterizations directly at the LLE. The experimental plan is schematized in Figure 63. It consists of three steps: (1) fabricating two silica GLAD samples, (2) characterizing the samples' optical properties and internal structure the day after fabrication, and (3) studying how the properties of one sample change when placed in a climate chamber (CC) with hot (70 °C) and humid (60 % RH) environment. The second sample will be stored in ambient air. At regular intervals, both samples will undergo the same series of characterizations.

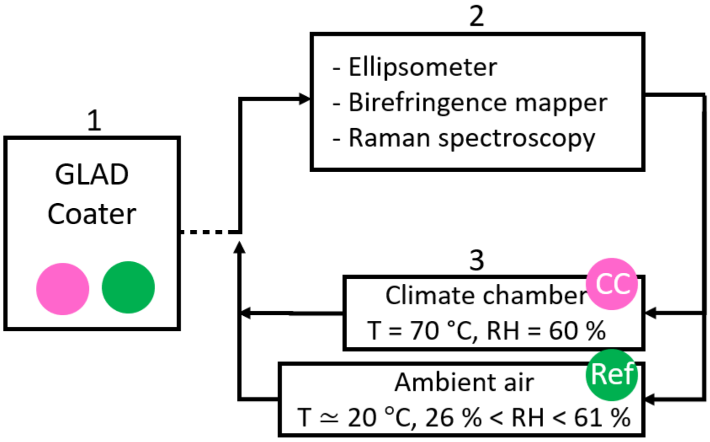

Figure 63. Experimental procedure for the stabilization of the silica QWPs. Pink sample is the CC sample. Green sample is the reference sample (Ref) stored in ambient air.

The samples were fabricated following the same procedure as the samples described in Chapter 2. To measure in detail the impact of the climate chamber on the samples, two QWPs were deposited on 50-mm diameter fused silica (FS) substrates. Those samples were used for the following characterizations: Raman spectroscopy (σ = 300-1500 cm^{-1}, $\lambda_{excitation}$ = 532 nm), ellipsometry (λ = 300-600 nm, step = 10 nm, optical axis position: 0°, 45° and 90°, transmission measurement), and birefringence mapping (λ = 355 nm, step = 2 mm). The details on the characterization techniques are described in Chapter 2.

The samples treated in the climate chamber are called CC. The other samples that stay in the ambient air are called Ref; for reference sample. The Ref samples were stored in polystyrene boxes with a hygrometer and a thermometer to ensure environmental control and to facilitate the collection of data in the event of unexpected measurement values. The CC samples were treated for 14 days, followed by a one-day break, and finally treated for 6 days, for a total of 20 days in the chamber. Subsequent to this period, the samples were stored in ambient air in their polystyrene boxes and monitored for a period of six months. Then, in total, samples were monitored for a period of 10 months from November 2024 to September 2025.

2.2. Characterization of the climate chamber impact on the silica coatings stability

Figure 64 presents the retardance deviation for the CC sample (pink) and the Ref sample (green) over time in days. The time displayed does not reflect the time in the chamber. The measurements begin on day 1, which is the day after unloading the sample from the coater in vacuum.

The CC period started after the measurement on day 2 and ended on day 23. Following this, the sample was stored in ambient air, alongside the Ref sample. The retardance is calculated as an average of the retardance over the surface of the sample.

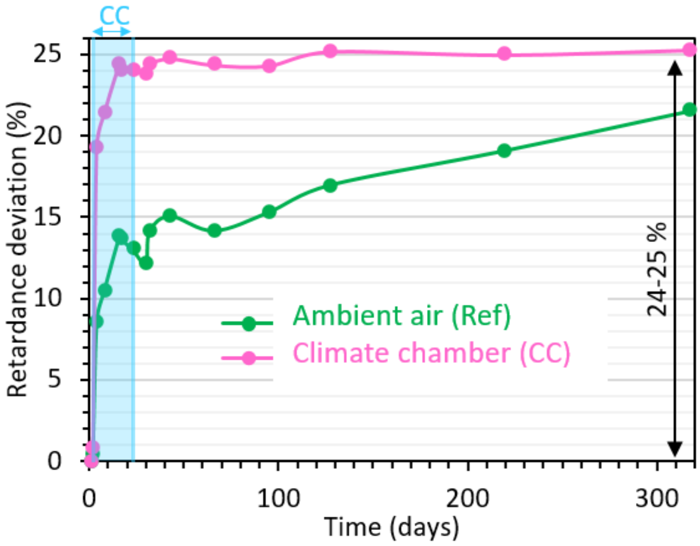

Figure 64. Retardance deviation as a function of time. Ref sample (green) is stored in ambient air. CC sample (pink) is first stored in a climate chamber at 70 °C, 60 % RH, and then in air with the reference sample. Blue lines delimit the time in the climate chamber from day 2 to day 23.

As illustrated in Figure 64, there is a rapid increase in retardance for both samples, particularly obvious in the CC sample. After the fabrication the retardance is 71.6 nm for the Ref sample and 71.4 nm for the CC sample. One day later, the retardance increased by 1 % for both samples. However, after two days in the climate chamber (day 4), the retardance increased by 9 % for the reference sample and by 19 % for the climate chamber sample. After the 14-day in the CC, i.e., on day 16, the retardance increased by 24 % for the CC sample and by 14 % for the Ref sample. From this date to day 317, the retardance increased by 1 % for the CC sample and by 6 % for the Ref sample. After 14 days in the CC and during the 300 days after in ambient air, the retardance appears to be constant at 24-25 %. Oppositely, it seems that the retardance of the reference sample continues to increase. The last retardance values are 87.0 nm for the Ref sample and 89.5 nm for the CC sample. The measured retardance deviation is comparable to the one measured on the same type of sample after five months [26]. In conclusion, it appears that the climate chamber accelerates the stability of the retardance of the QWP samples.

As a reminder, retardance is the product of birefringence by the thickness. To understand the retardance increase or to highlight another involved phenomenon, ellipsometry was performed. The spectra of the measured MM elements before and after 14 days in the climate chamber are presented in Appendix 4. These spectra were analyzed using the same model described in Chapter 2 and 3 and the fitted parameters were the thickness, the depolarization split and the void fraction. All the azimuthal rotations, the Mueller matrix elements and measurements were fitted together.

Figure 65 presents the refractive index dispersion of the birefringent layer before, during, and after the climate chamber. First measurement (pink full line) was before the climate chamber, and two days after the fabrication. Second measurement (green full line) was after 14 days in the climate chamber. Third measurement (purple dashed and dotted line) is after 20 days in the climate chamber. Last measurement (blue dashed line) is after the climate chamber and after seven days in ambient air. The dispersion is the average of n_x and $n_{y,}$ which are the indices in the cross-section plane of the column.

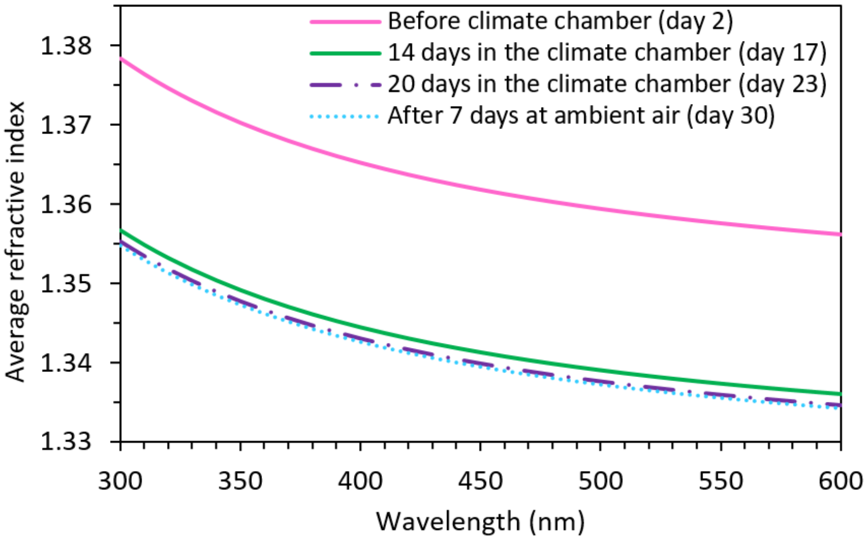

Figure 65. Average refractive indices between n_x and n_y of the birefringent layer before the climate chamber, for 14 days in the climate chamber, for 20 days in the climate chamber, and after 7 days in ambient air.

After 14 days in the CC, the average refractive index (at 350 nm) decreased from 1.37 to 1.34. For all the other measurements, values near 1.34 were found. The differences (less than 0.001) being below the sensitivity of the ellipsometry measurement (0.01), were not significant. The sorption of water should increase indices.

However, Figure 65 shows the opposite, suggesting that water sorption does not compensate for the decrease in refractive index associated with matrix relaxation during hydrolysis.
This indicates that the matrix is highly stressed.

Table 8. Evolution of the void fraction, the depolarization split, and the birefringence at 350 nm for the climate chamber sample. First data are before climate chamber, on day 2. Second data are after 14 days in the climate chamber, on day 17.

	Void fraction	D_{xy}	Birefringence at 350 nm
Before climate chamber (day 2)	21 % ± 0.38 %	0.30 ± 0.002	0.028
14 days in the climate chamber (day 17)	25 % ± 0.27 %	0.27 ± 0.002	0.036

Table 8 summarizes the void fraction, the depolarization split, and the birefringence at 350 nm, for the CC sample, before, and after 14 days in the climate chamber. The void fraction increased slightly from 21 % to 25 %, the depolarization split decreased slightly from 0.3 to 0.27, and finally, the calculated birefringence increased significantly from 0.028 to 0.036. The evolution of the birefringence is consistent with the retardance data previously presented in Figure 64. This analysis highlights the difficulty of the process. The decrease in the refractive index could be explained by an increase in the void fraction.

2.3. Understanding the phenomena with modification of internal structure when stabilizing samples

While the retardance and ellipsometric measurements were being conducted, Raman spectroscopy was performed to establish a correlation between the retardance evolution and the internal structure of the QWPs. Figure 66 presents the Raman spectra of the sample that will become the CC sample (pink) and the Ref sample (green), taken one day after the fabrication. All Raman spectra are normalized, with the maximum value set at 1 (at the D1 band) and the minimum value set at 0.

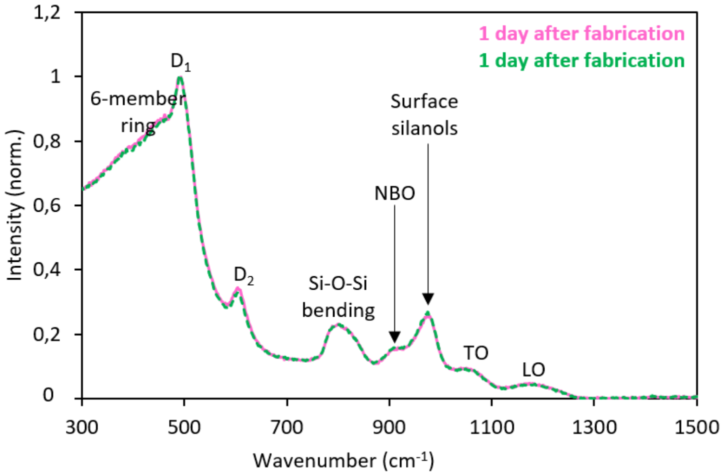

Figure 66. Raman spectra of the QWPs just after fabrication, on day 1. Sample that will be exposed to climate chamber is in pink (full line). Sample that will remain exposed to ambient air is in green (dashed line).

As illustrated in Figure 14, the bands that were discussed in Chapter 3 and in the previous section are visible. These bands are annotated on the spectrum. Furthermore, both samples exhibited identical Raman spectra. This observation enabled us to study the impact of the climate chamber on molecular vibrations.

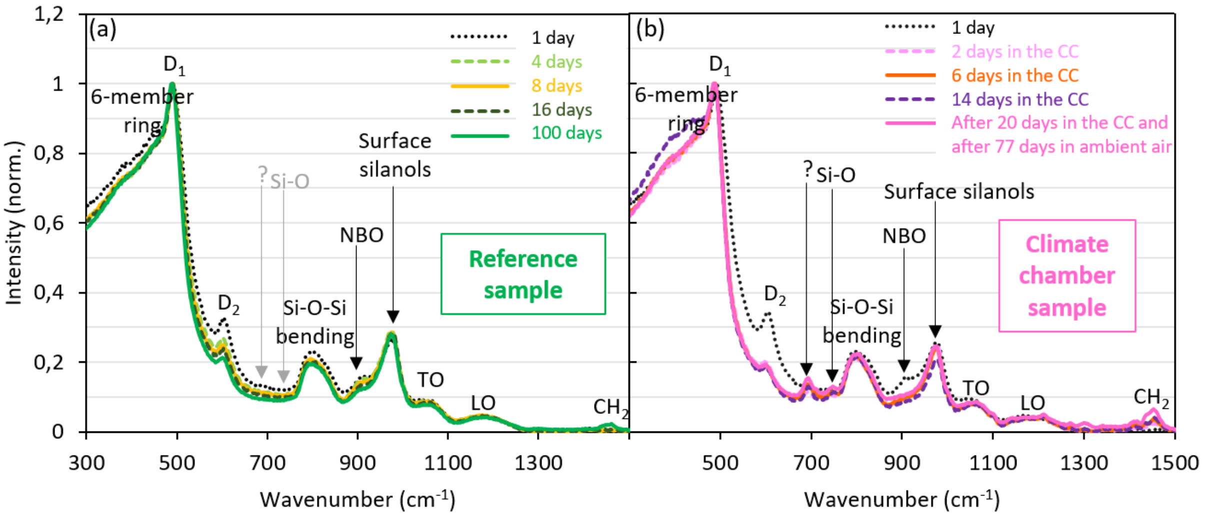

Figure 67. Evolution of the Raman spectra of the QWPs as function of time. (a) Evolution of the reference sample in ambient air. (b) Evolution of the climate chamber sample.

Figure 67 presents the evolution of the QWPs as a function of time as determined by Raman spectroscopy. Figure 67(a) is the evolution of the reference sample in ambient air, at day 1 (black dotted line), day 4 (light green dashed line), day 8 (yellow full line), day 16 (khaki dashed line), and day 100 (green full line).

Figure 67(b) is the evolution of the climate chamber sample at day 1 (black dotted line), after 2 days in the CC (light pink dashed line), after 6 days (orange full line) in the CC, after 14 days in the CC (purple dashed line), and after 20 days in the CC, and after staying for 77 days in ambient air (pink full line). For the sample exposed to ambient air (Figure 67(a), in green), the D_2 band (3-membered ring), the Si-O-Si band and the NBO (Non-Bridging Oxygen) band progressively decreased over time. The intensity of Si-O-Si is lowered compared to the CC sample. The number of 6-membered ring decreased after 4 days and the intensity is stable. Although it is difficult to observe, the surface silanols exhibited a slight increase from day 4 and remained consistent for the remainder of the measurements. For the last spectrum, a CH_2 band started to grow.

For the sample exposed to the climate chamber (Figure 67(b), in pink), the D_2 band intensity decreased immediately after exposure to hot humidity and reached a lower intensity as compared to the reference sample. Furthermore, its intensity appears to remain consistent over time. The Si-O-Si band decreased after 2 days in the CC and remained stable for the other measurements expect for the last measurements after staying in ambient air (pink full line), for which the intensity slightly increased to be closer to the first measurement before CC. After the first exposure to the climate chamber, the NBO band, presents a lower intensity than the reference sample. Moreover, its intensity appeared to slightly vary depending on the measurement. The number of 6-membered rings seemed to be stable with exception to the 14 days measurement (purple dashed line). Surface silanols progressively decreased over time with again the exception of the 14 days measurement (purple dashed line) which is importantly lowered. The intensity of this band is lower than for the reference sample. Three new bands began to grow from day 2: at around 700 cm^{-1}, 750 cm^{-1} and 1450 cm^{-1}. The origin of the one around 700 cm^{-1} is unknown and more investigation is required. The two other bands are believed to be related to Si-O and CH_2. For these three bands, the intensity is increasing as a function of the time. The two bands around 700 cm^{-1} and 750 cm^{-1} are only visible for the samples in the CC.

In summary, for the D_2 band, the Si-O-Si band, and the NBO band, the climate chamber seemed to rapidly accelerate their evolution. There is a difference in the 6-membered ring, which evolved for the Ref sample only and has a smaller intensity. The behavior of the surface silanols is the opposite for both samples with a higher intensity for the Ref sample.

There is the appearance of two new bands for the CC sample which could be a Si-O band and still an unknown band. Finally, the CC seemed to importantly accelerate the appearance of the CH_2 band.

The explanations could be the following: the climate chamber accelerates drastically the relaxation of the silica matrix with the formation of larger membered ring Si-O as illustrated by Figure 68. It illustrates the hydroxylation of the silica surface via the opening of three- and five-membered siloxane rings to form more stable six-membered rings [120], [121]. The angles of the bonds open and the density decreases as well. Surface silanols are correlated to siloxane: the CC sample seems to have more siloxane and less surface silanols than the reference sample. Other contributions, such as NBO and surface silanols, have a lower intensity perhaps due to evolving into fully formed silica or carbon related bonds.

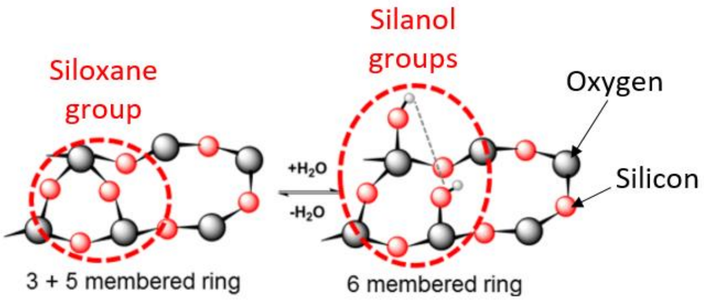

Figure 68. Hydroxylation of silica after exposure to humid environment: three- and five-membered rings opening to six-membered ring [120].

For the C, the hypothesis of a contamination into the climate chamber may be done, however carbon was already observed in the characterizations presented in Chapter 3. The change in the internal structure because of the exposure of the climate chamber could also increase the affinity with carbon bonds. Nevertheless, as observed with the laser resistance results of the previous section, the contamination of the samples does not appear to have an important impact on their LIDT. Such tests should be performed to validate this hypothesis.

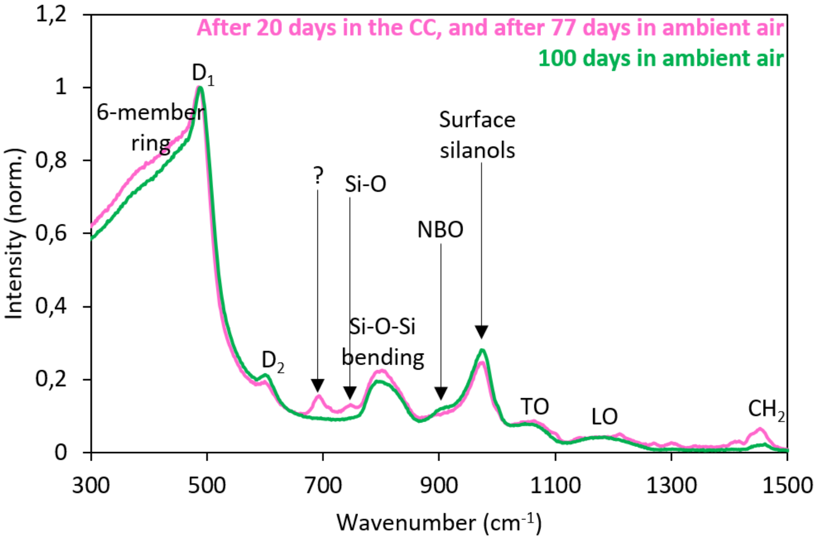

Figure 69. Raman spectra of the QWPs. CC sample: after 20 days in the climate chamber, and after 77 days in ambient air; Ref sample: 100 days in ambient air.

Figure 69 presents the comparison between the sample exposed to the climate chamber and the reference sample after 100 days. Compared to the Ref sample: the sample previously exposed to climate chamber, exhibited higher intensity for the 6-membered ring bond and the Si-O-Si bond, while the intensity of the D_2 band, NBO, and surface silanols were lower. The significant differences observed in the previous spectra between the Ref and CC samples (Figure 67) are less important here. The Raman spectra indicate that both samples tend to exhibit a convergence in their microstructure after 100 days.

The decreasing of the surface silanols (Figure 69) tells us that less water could physisorbed on the surface, and, as a consequence, the matrix may exhibit less variation, which was verified with the measurement of the retardance in nitrogen purged environment (Figure 70). Between the measurement in air and the measurement in nitrogen, the retardance decreased by 8.6 % for the climate chamber sample and by 14 % for reference sample.

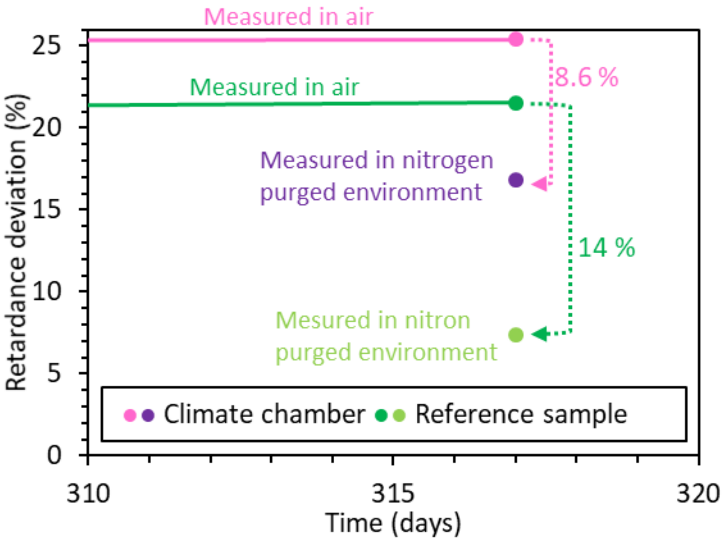

Figure 70. Evolution of the retardance of the climate chamber sample and the reference sample on the same day at different environments: ambient air and nitrogen purged.

GLAD films have mesopores between the columns and micropores inside the columns. When the environment is purged to nitrogen, the water inside columns' micropore is removed, the index of the columns is changed and the retardance is different, as observed in Figure 70. In the CompleteEASE model, the void fraction represents the addition of the mesoporosity and the microporosity. However, by knowing this variation of retardance, the fraction of mesoporosity and microporosity might be separated.

In conclusion, the acceleration of aging using the climate chamber seems to function regarding the retardance over time. The results of this section, in conjunction with those of the previous section, are highly encouraging for the use of these components in ambient air.

3. Summary of Chapter 4

Given the intended locations of the QWP in the LMJ, whether in controlled ambient air or in contaminated vacuum, concerns have been raised regarding the sensitivity and stability of this coating over time and depending on the environment.

The first section allowed the study of a dimethyl phthalate (DMP) contaminated vacuum, which corresponds to a location next to the LMJ target chamber. The performances of the GLAD component were studied monitoring transmission, retardance and laser resistance. Phthalate contamination reduced transmission at 351 nm from 96 % to 87 % after 17 hours of contamination. This transmission value did not recover even after 29 hours of storage in non-contaminated ambient air. This reduction in transmission at 351 nm appears to be associated with DMP absorption in this spectral range. Retardance measurements taken after contamination and storage in air for one month revealed an inhomogeneous sample surface. This inhomogeneity of retardance resembled the feature visible on the sample one day after the contamination protocol. Moreover, the laser resistance of the QWPs was lowered in a vacuum environment, however, the contamination did not further reduce the resistance. The presence of DMP appears to affect the optical properties by infiltrating the pores of the silica GLAD coating. The characteristic bonds of DMP were observed in the contaminated samples even after two months of storage in air. This contamination results in an irreversible impact or very slow desorption over time. Using this device in a contaminated environment could be detrimental to the optical performance of GLAD QWP components.

Based on these findings, the location in ambient air was determined to be the optimal choice. However, GLAD samples are known to be sensitive to relative humidity and known to evolve over time. Therefore, an experimental method was employed to stabilize the samples. The QWP samples were exposed to a hot and humid environment in a climate chamber. For 14 days, in the climate chamber, the retardance values were the same as the ones published by S. MacNally *et al.* after 5 months. The sample demonstrated a retardance increase of 24-25 %. The retardance of this sample has been measured over a period of more than 10 months and the results indicate that the sample has stabilized, while the retardance of the sample exposed to ambient air is still increasing.

This evolution is characterized, notably, by a decrease in the average refractive index of the birefringent layer and an increase in birefringence. After a two-day period in the CC, the internal structure appeared to have adopted a stable form, with the silica matrix exhibiting signs of relaxation. The aging acceleration has also diminished the sensitivity of the QWPs to environment changes. Indeed, the measure in nitrogen purged environment is 8.6 % different for the climate chamber sample compared to 14 % for the reference sample. To conclude, using GLAD QWPs samples in silica could be a promising option.

Chapter 5. Fabrication of a less sensitive wave plate coating using alumina

Chapter 3 and Chapter 4 focused on the qualification of a silica-based GLAD QWP in ambient air and contaminated vacuum. This contamination impairs the optical performance of silica thin films. An artificial aging of these silica-based components appeared to be a promising option for ambient air use. However, the engineering complexity of the LMJ would not necessarily allow for the selection of the QWP component's location. As outlined in Chapter 1, alumina was identified as a promising material. In addition to the specifications previously listed regarding retardance, transmission, and laser resistance, the material requires chemical stability. Owing to the higher refractive index of alumina, such GLAD films should exhibit higher birefringence compared to silica films. They also demonstrate notable 3ω laser damage resistance [13], [122], [123]. Alumina is recognized for its chemical inertness [49] and alumina thin films are utilized as humidity barriers [50] - [53]. These chemical properties tend to indicate superior resistance to aging and environmental effects.

This chapter will present a QWP design fabricated from alumina and coated by the serial bideposition (SBD) GLAD technique. The main findings of this chapter have been published in the following article [106].

First, the optimization of the deposition conditions on single anisotropic layers in order to obtain high birefringence will be described. The characterization of birefringence will be performed through the modeling of ellipsometric measurements conducted on the coatings. Secondly, we will provide a detailed explanation of the fabrication of the all-alumina QWP. The optical performance of this device will be evaluated in terms of retardance and transmittance. The following section will investigate the stability of the alumina QWP regarding the environment (relative humidity or contaminated vacuum) and over time. The following measurements will be discussed: retardance, laser resistance, and transmission. Finally, as the primary concepts discussed in this chapter have been previously addressed in other chapters, they will not be elaborated upon again.

1. Study of the optical properties of alumina single layer depending of the serial bideposition angle

As previously outlined in Chapter 3, GLAD QWPs can be fabricated as alternating layers of: anisotropic layers for the optical function, fabricated by the SBD technique, and isotropic denser layers for mechanical strength and to prevent broadening of the columns [13], [25], [26].

Given that the optical retardation function is only achieved with the anisotropic layers, a thorough study was conducted to optimize the deposition angle in order to obtain the highest anisotropy.

1.1. Fabrication of single anisotropic layer in alumina

The samples were coated at various angles around 70° ± 10° (as detailed in Table 9) since it is generally where the maximum birefringence for SBD columns has been reported [85]. The letters I and B, correspond to the isotropic and birefringent, respectively. The layers have a quarter-wavelength optical thickness at 351 nm. Therefore, 4B signifies a full-wavelength optical thickness. All samples were coated on 50 mm diameter silicon wafers and fused silica substrates, and were fabricated in the same 1.2 m vacuum chamber described in Chapter 2. As a reminder, the following parameters are: a chamber temperature of 25 °C, a background pressure better than 1×10^{-6} Torr, a deposition pressure of 1.4×10^{-4} Torr achieved by oxygen backfill, a time per subdeposit angle of 3 seconds, a rotation speed of 180 °/s, and a deposition rate of 1.5 Å/s.

Table 9. Details on the studied deposition angles. All the layers (I for isotropic and B for birefringent) have a quarter-wavelength optical thickness.

Type of coating	Single layer						
Deposition angle	0°	± 68°	± 73°	± 76°	± 78°	± 80°	± 82°
Design	I	4B	4B	4B	4B	4B	4B

Figure 71 presents the SEM images of the layer deposited at ± 68°, ± 73°, and ± 82°, observed from the top and from the cross-section. The fabricated columns are perpendicular to the substrate and have a constant diameter of approximately 20 nm. For all films, a porous, columnar structure was formed with a significant number of large open voids.

Smaller columns are observed for all three coatings, they may come from the breakage of the sample required for the observation of the cross-section. The one-direction orientation of the columns and the pores is easily noticeable for all three coatings. The coating at ± 82° appears to present a lower aspect ratio that may indicate a lower birefringence compared to the two other films.

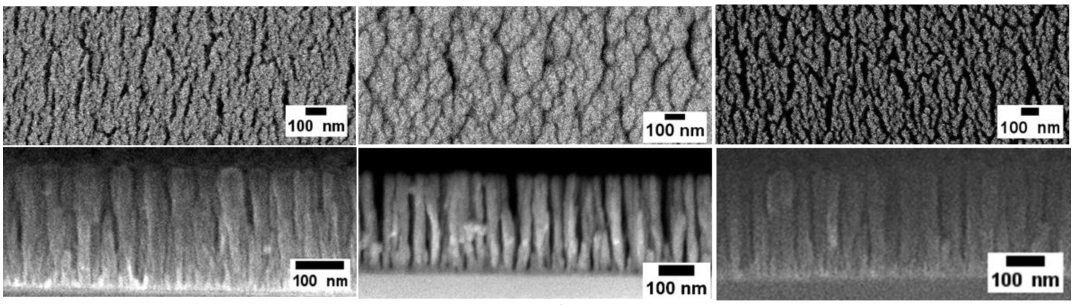

α = ± 68° α = ± 76° α = ± 82°

Figure 71. SEM images on the top and the cross section of single anisotropic layers deposited at ± 68°, ± 76°, and ± 82°

1.2. Optimization study of the anisotropic layer based on CompleteEASE models related to ellipsometric measurements

The optimization study focused on identifying the highest birefringent single layer. The property was assessed using models related to MM ellipsometric measurements, as previously described in Chapter 3. The MM was measured using an RC2 ellipsometer (J. A. Woollam). It was characterized in transmission, from silica substrates, between 210 and 1690 nm, at several azimuthal orientations: 0° (fast axis vertical), 45°, and 90° (slow axis vertical). Figure 72 presents the measured MM and the generated MM of the single anisotropic layer deposited at ± 76°.

As previously discussed in Chapter 2 and Chapter 3, examining the MM allows for the analysis of the film's optical behavior. The same conclusions can be drawn: the sample may have transmission losses, and the optical axes follow the axes of symmetry of the column cross-section in the (x, y) plane. However, alumina exhibits higher dichroism and birefringence values compared to silica. As for example, at 0°, m_{34} has a maximum value of 0.3 for silica and 0.5 for alumina.

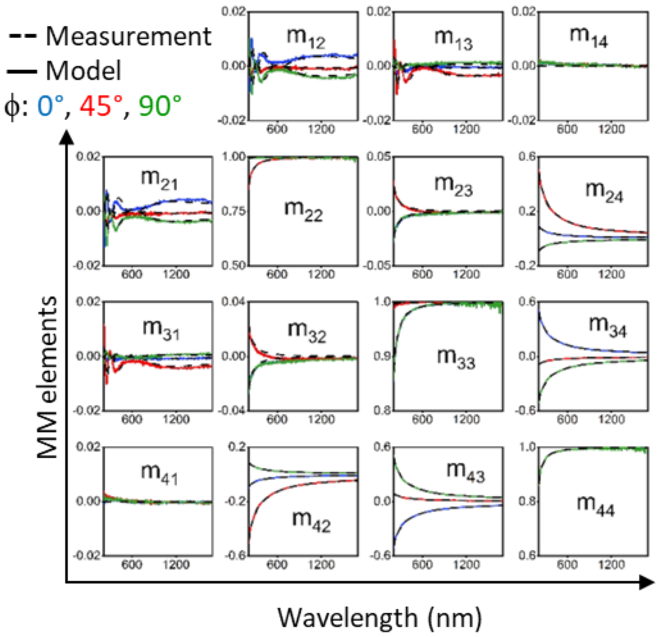

Figure 72. Correspondence between the measured MM by the ellipsometer and the model created with the CompleteEASE software, for one columnar layer deposited at ± 76°.

To extract the optical properties from the measured MM (Figure 72), a CompleteEASE model was built, as outlined in Chapter 3. The distinction is that this time, alumina was utilized instead of silica. The characteristics of the alumina material were obtained from the measurement of the single isotropic layer listed in Table 9. For the latter, Psi and Delta (see Eq. (19)) were measured in reflection at 65°, 70°, and 75° from the silicon substrate and between 300 and 1100 nm. The model uses a Cauchy dispersion relationship, as described in Chapter 2. The following parameters were determined: $A = 1.58$, $B = 0.0055$, and $C = 0$ (see Eq. (5)). For the anisotropic model, the void fraction is modeled to be constant throughout the layer.

Figure 72 presents the result of the fit between the measured MM and the model for one columnar layer deposited at ± 76°. The MSE of 2.13 for the single layer shown in Figure 72 provided confidence in these results. The MSE varied between 1.32 and 3.99 for all the single anisotropic layers.

Figure 73 presents the evolution of the fitted parameters (D_{xy} and % void) and extracted parameters ($\bar{n}_{xy}$ and Δn) from the optical model as a function of the deposition angle. The error bars correspond to the 90 % confidence limit in the value parameters obtained from the fitting procedure.

The depolarization split increased from 0.645 to reach the maximum value of 0.680 at 76° and then decreased to 0.665 at 82° (see Figure 73(a)). Figure 73(b) shows an increase in the void fraction from 30 % - 29 % for the first two angles (68°, 73°) to higher values for 76°, 78°, and 80° with a maximum of 37 % at 80°. After this plateau, the void fraction decreased to 32 % at 82°. These orders of magnitude are typical in other materials such as silica [26]. It should be noted that D_{xy} and void fraction were highly correlated (> 97 %) which limits the independent determination of these two parameters. As a result, only the in-plane refractive index and birefringence were accurately determined in the fitting procedure.

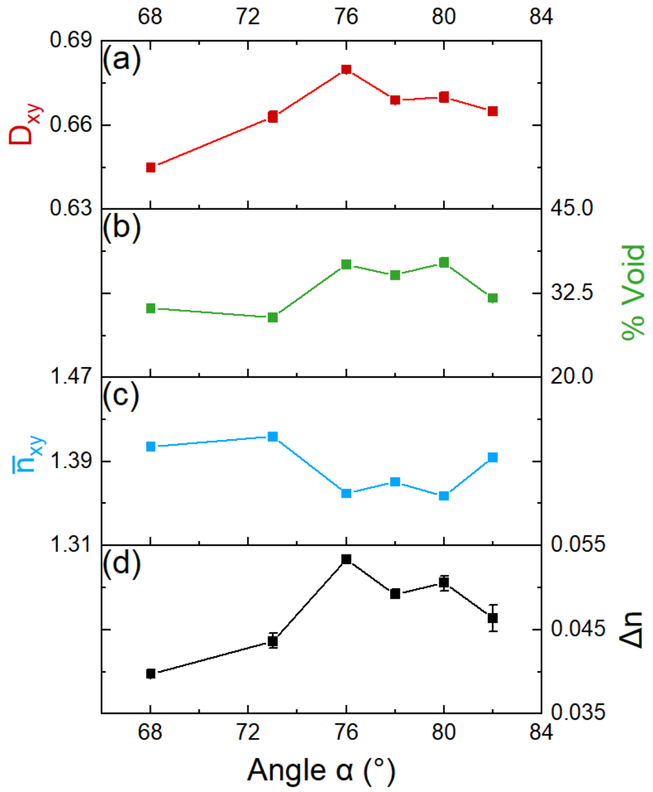

Figure 73. Characterization as a function of deposition angle, including: (a) depolarization split, (b) void percentage, (c) in-plane refractive index at 351 nm and (d) in-plane birefringence at 351 nm. (a) and (b) are fitted parameters from the model. (c) and (d) are extracted parameters. (a) and (b) error bars are extracted from the fit. (c) and (d) errors are calculated by taking into account the correlation between the fitted parameters.

Figure 73(c) presents the mean index of the columnar layers. It was calculated as the average of n_x and n_y. As expected, this value was inversely proportional to the void fraction of the columnar layers. It varied between 1.41 and 1.36 at 351 nm. In comparison, the dense layers deposited at normal incidence had a refractive index of 1.62 at 351 nm.

Figure 73(d) is the in-plane birefringence, calculated as follows: $\Delta n = n_y - n_x$. We observed an increase from 0.040 for a deposition angle of 68° to reach a maximum value of 0.053 at 76° and then a decrease to reach 0.046 at 82°. This suggests that a deposition angle of 76° would be the optimal to yield birefringent layers in a WP design. These values are larger than those obtained for silica GLAD coatings where Δn was of approximately 0.036.

For the layer deposited at ± 76°, the thickness was estimated at approximately 253 nm. With a birefringence equal to 0.053 at 351 nm and 355 nm, the retardance is 13.5 nm at both wavelengths. The value is close to the retardance of 13 nm measured with the birefringence mapper at 355 nm.

In summary, at this specific SBD angle of ± 76°, the created microstructure is more favorable for the formation of a high birefringent film. Moreover, this finding, based on an experimental determination, is in the range of other materials, such as Ta_2O_5, ZrO_2, or TiO_2 [85].

2. Fabrication of a quarter-wave plate multilayer coating in alumina

2.1. Design of the quarter-wave plate as a multilayer in alumina

From the single layer to the bilayer, alumina exhibited trends similar to those of silica. The thickness and the void fraction decreased by almost 8 nm and 11 %, respectively. When designing the QWP, this reduced retardance value was taken into account. The retardance of the bilayer is 12.5 nm at 351 nm. Given that the retardance of the QWP ($\frac{\lambda}{4} = 87.75$ nm at 351 nm) is the sum of the retardance of each birefringent layer, seven anisotropic layers are required. As previously discussed, an isotropic layer was deposited at 0° between each anisotropic layer to prevent broadening of the columns. In addition to the seven-layer pairs, a final layer was incorporated to minimize reflection of the multilayer QWP.

The thickness and index of this antireflective layer were designed to generate destructive interferences in the reflected light of the overall interaction of the design. These required parameters were achieved by taking advantage of the porosity control inherent to the SBD microstructure. The optimal index match with the overall design was achieved at an angle of ± 86° at the time of conducting this work.

Future work will include the optimization of this layer, potentially considering a graded-index approach. Nonetheless, adding this AR layer increased the transmission of the QWP by 4 %. To summarize, the design can be written as follows: Substrate/$(4B/I)^7$/AR/Air. All the layers have a quarter-wave optical thickness. Figure 74 presents SEM images of the QWP.

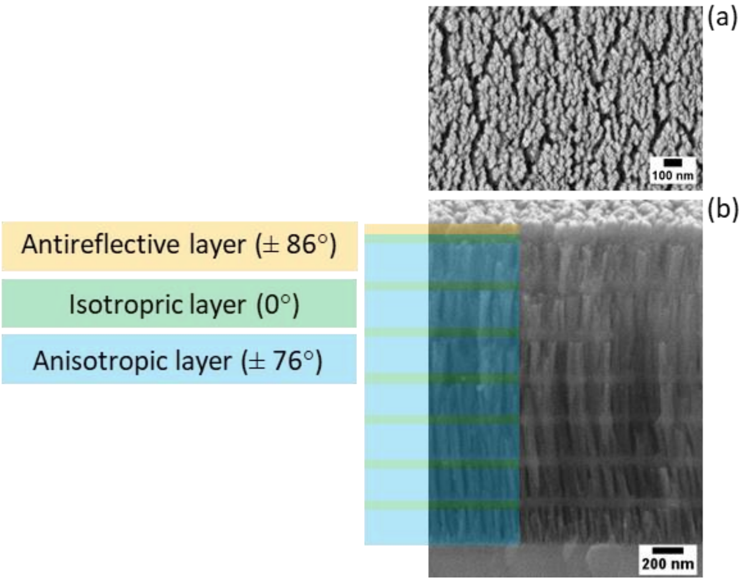

Figure 74. SEM images of the multilayer in alumina, observed from the top (a) and from the cross-section (b).

The coating consists of 15 layers, including seven pairs of anisotropic layers (± 76°) and isotropic layers (0°), along with an antireflective layer (± 86°). The straight columns are clearly visible for the anisotropic layers in between the isotropic layers. The top of the multilayer coating exhibits significant roughness and porosity.

The multilayer is designed with 15 layers, compared to 21 or 31 layers for the silica QWP (depending on the environment of use). Reducing the number of layers could offer a distinct advantage in terms of laser resistance or mechanical resistance.

2.2. Optical performances of the GLAD QWP made of alumina

Finally, the QWP's performance was analyzed using ellipsometry, following the same procedure as previously described. Birefringence mapping was used to assess homogeneity, and spectrophotometry was used to determine the transmission property.

The model of the QWP was created with the exact repetition of the bilayer seven times. The AR layer is modeled as alumina and void, mixed using the BEMA (see Chapter 2 and Chapter 3). None of the parameters were bounded.

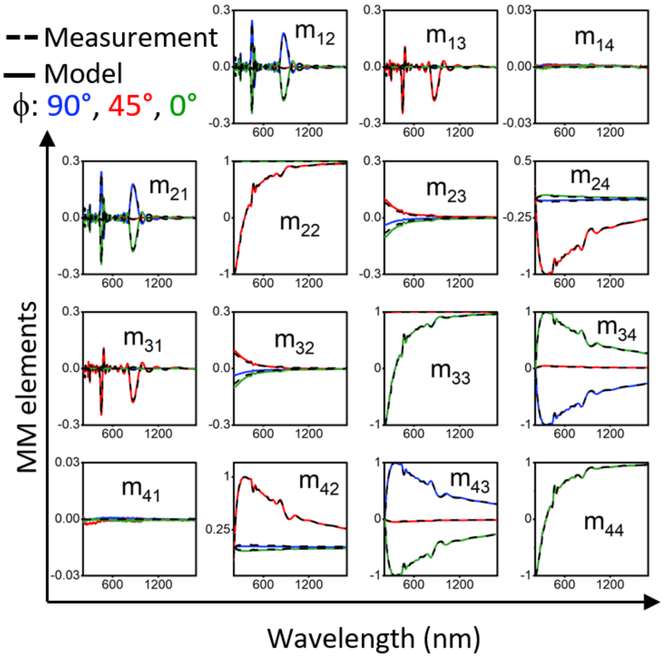

Figure 75. Correspondence between the measured MM by the ellipsometer and the model created with the CompleteEASE software, for the QWP coating.

Figure 75 presents the correspondence between the modeled MM and the experimental MM. They are a good match, and an MSE of 8.34 was found in that case. m_{12} and m_{13} suggest that the coating will exhibit some transmission losses. Additionally, as for silica, the optical axes follow the axes of symmetry of the column cross-section in the (x, y) plane.

Figure 76(a) presents the fitted parameters of the multilayer QWP. For the anisotropic layer, a thickness of 230 nm and a void fraction of 25 % were found. The antireflective layer had a thickness of 52 nm and a void fraction of 34 %. The experimental thickness of the overall coating is 2.23 µm, compared to a modeled thickness of 3.59 µm, for the silica QWP. Figure 76(b) presents the refractive index dispersion of the anisotropic layer with n_z, n_x, and n_y, as well as, the antireflective layer with n_{AR}. The in-plane refractive indices for the anisotropic and antireflective layers were modeled at 351 nm: 1.44 and 1.40, respectively. The birefringence was measured at 0.055 at 351 nm, and the retardance was calculated at 88 nm (for 351 nm and 355 nm).

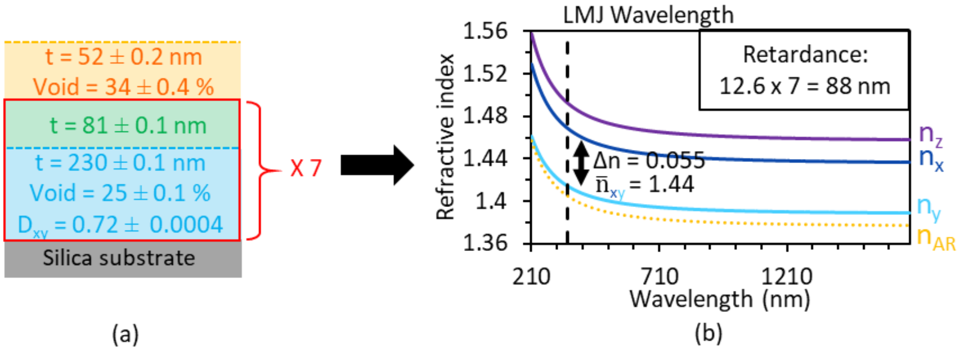

Figure 76. (a) Fitted parameters of the CompleteEASE model for the multilayer QWP. (b) Refractive index dispersion of the anisotropic layer of the multilayer QWP. Black dashed line at 351 nm is the wavelength of LMJ. Δn is the in-plane birefringence at 351 nm. $\bar{n}_{xy}$ is the in-plane average refractive index at 351 nm. Retardance at 351 nm is shown in inset.

Retardance (Δn) was measured with the BM at 355 nm in transmission from the silica substrate sample with a 0.5-mm step. Figure 77 presents the retardance map of the QWP. The retardance is 89 ± 0.6 nm, corresponding to a retardance of $\frac{\lambda}{3.9}$, with good uniformity over the sample. This contributes to our confidence in the model. Finally, the retardance fits into the specification for the LMJ application, which is in the [λ/4; λ/2] range.

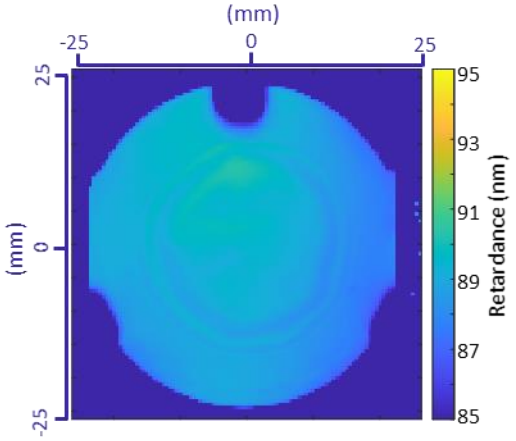

Figure 77. Retardance map of a QWP sample. The average retardance is 89 ± 0.6 nm

In addition to retardance, the transmission property is crucial. The transmission of these was measured with a spectrophotometer at normal incidence from fused silica substrates, and the reflection with a measurement system built in-house.

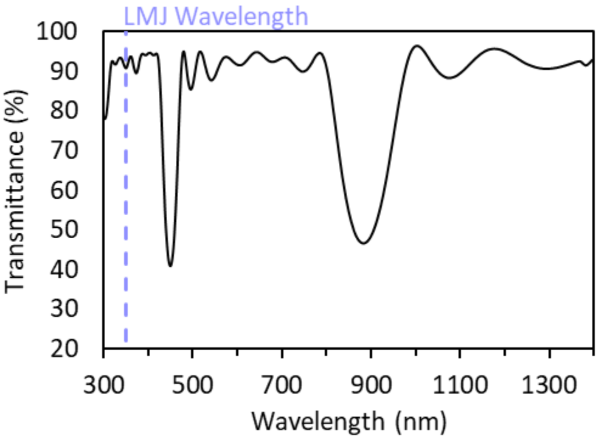

Figure 78. Measured transmittance of the QWP. The lavender dashed line at 351 nm represents the wavelength of interest utilized in the LMJ.

Figure 78 shows the transmittance spectrum of the QWP sample (uncoated backside) at 0° of incidence for a beam linearly polarized at 45° from the fast axis of the QWP. At the wavelength of 351 nm (lavender dashed line), the GLAD coating exhibits 91.1 % and 92.0 % transmittance for S and P polarization, respectively, while reflecting 6.22 % and 5.85 % of the light. The estimated losses are approximately 2.7 % in S polarization and 2.1 % in P polarization. Previous studies on GLAD silica coatings have shown that these losses are mainly due to scattering, a phenomenon that can be attributed to the columns or the roughness created during the deposition process [26]. Further optimizations are required to improve the performance of the QWP.

In summary, we demonstrated the feasibility of fabricating QWPs made of alumina. These films are composed of seven pairs of anisotropic layers deposited at ± 76°, and isotopic layers deposited at 0°, along with a layer deposited at ± 86 ° for an antireflective purpose. The QWP device has a uniform retardance that falls within the specified range of [λ/4; λ/2]. However, the transmittance is insufficient, and optimization should be performed on the final layer, the antireflective layer. The following section will examine the stability of the alumina QWP over time and in various environmental conditions.

3. Investigation of the stability of the alumina wave plate over time and environmental changes

3.1. Highlight of the stability of alumina QWP over time

First, to evaluate the stability of alumina QWP over time, the retardance of an alumina QWP was tracked over almost one year. The measurements were performed using the birefringence mapper by scanning the entire surface of a 50-mm sample with a 4-mm step and at 355 nm.

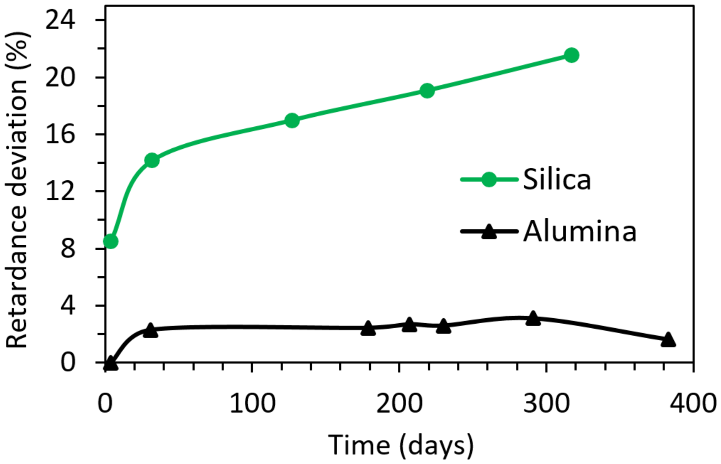

Figure 79. Retardance deviation of the alumina QWP, compared to the silica QWP presented in Chapter 4.

As shown in Figure 79, the retardance track of the alumina QWP (black triangles) was measured over a period extending from four days following the unloading of the sample from the coater to a year later. Silica retardance variations (green circles), which were already presented in Chapter 4.2, were incorporated for comparison. The samples were stored in ambient air between measurements. The alumina QWP described in this work exhibited a slight retardance increase of 3.1 % after more than one year. In comparison, the silica QWP exhibited a 22 % retardance increase after 10 months. Alumina QWP demonstrated stability over an extended period.

3.2. Sensitivity of alumina QWP to relative humidity and contamination

To assess the impact of relative humidity, measurements of retardance were conducted in ambient air and in a nitrogen environment. We observed a 1 % difference for the alumina QWP, as compared to a 20-25 % difference for the silica QWP [26].

The same schematic was performed using the spectrophotometer from 300 to 1400 nm. As shown in Figure 80, the measurement at ambient was found to be 91 %, while the measurement in dry air was 93 % at 351 nm. These results appear to support our hypothesis that the alumina QWP demonstrates stability over time and independent of relative humidity.

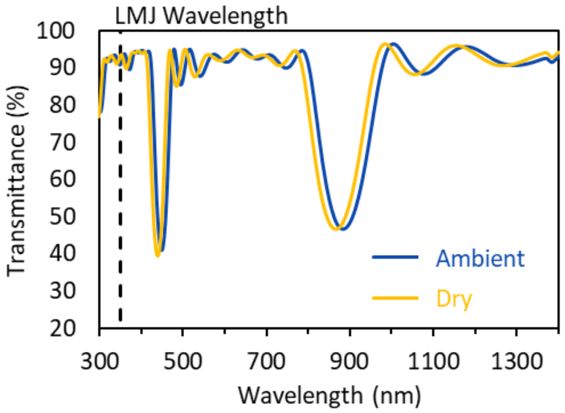

Figure 80. Transmission spectra of the alumina QWP measured in ambient air (blue) and in dry air (yellow).

In a second instance, alumina QWPs were contaminated, and the impact on the LIDT was analyzed such as presented in Chapter 4.1.3. Three tests were performed in three different environments: air, vacuum, and DMP contaminated vacuum. The tests were performed on fused silica substrates. The tests were completed using the testbed of the Fresnel Institute, as described in Chapter 2 and Chapter 4. The tests followed a 1:1 procedure with 20 sites tested. For the contaminated measurement, the alumina QWP was exposed to DMP at a pressure of 6.5 x 10^{-5} mbar for 23 hours. For the vacuum measurement, the QWP was kept in a vacuum at 6.5 x 10^{-5} mbar for 20 hours. The sample was oriented with its fast axis at 45° from the incident linear polarization direction with the coating on the exit face of the laser.

Figure 81 presents the results of the laser damage resistance tests on the alumina QWP, depending on the environment as well as the corresponding substrate of the coatings. The dashed lines show the fit of each measurement to an empirical sigmoid function. The damage probabilities resulting from this fit are summarized in Table 6.

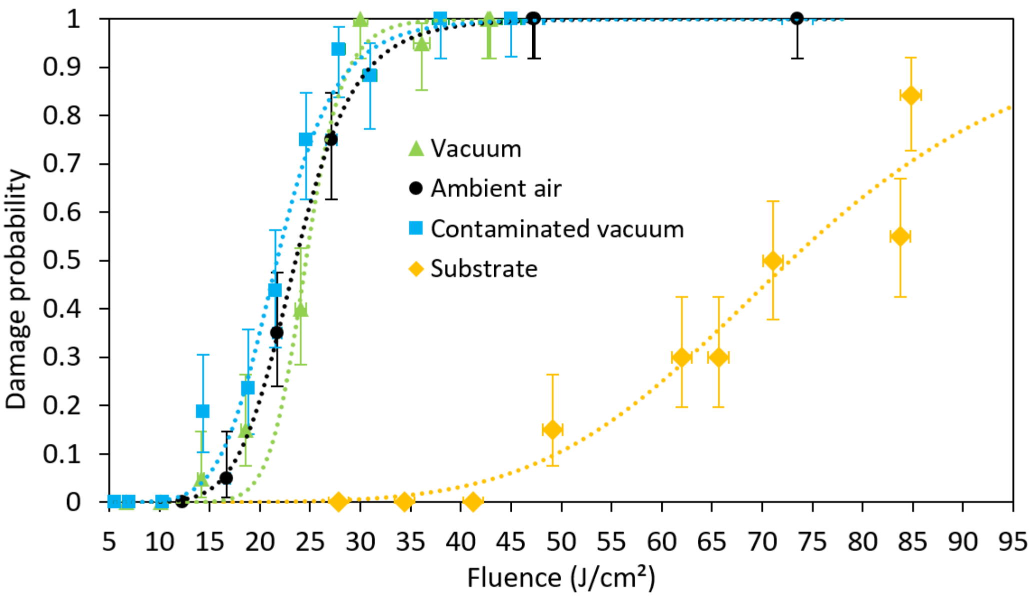

Figure 81. Laser damage resistance of the alumina QWP depending on the environment. Dashed lines are a fit between measurement and empirical sigmoid function.

In all environments, damage was consistently observed on the coating side. As described in Chapter 3, the error in the damage probability (vertical axis) depends on the number of sites tested. The fluence error (horizontal axis) is around ± 2.1 %; 2.2 %, 2.1%, and 1.9 % for the tests; in air, vacuum, and contaminated vacuum, respectively; and for the substrate. This error considers the energy calculus and the surface. Table 10 summarizes the thresholds for 25 % and 50 % damage probabilities.

Table 10. Results of the laser damage resistance tests depending on the environment (ambient air, vacuum and DMP contaminated vacuum). Laser functioning at 355 nm, with ps pulse length train in a ns window and $S_{eq} = 9.3 \times 10^{-5}$ cm²

Sample	Polarization	LIDT at 25 %	LIDT at 50 %
Al_2O_3 QWP	Ambient air	21 ± 0.4 J/cm²	24 ± 0.5 J/cm²
	Vacuum	23 ± 0.5 J/cm²	25 ± 0.5 J/cm²
	Contaminated vacuum	19 ± 0.4 J/cm²	22 ± 0.5 J/cm²
SiO_2 substrate	Ambient air	60 ± 1.1 J/cm²	73 ± 1.4 J/cm²

As illustrated in Figure 81 and outlined in Table 10, the bare substrate exhibits a considerably higher threshold compared to the alumina coatings. When examining the results in different environments, there is no significant discrepancy in the values obtained. The vacuum and the contaminated vacuum don’t seem to impact the laser resistance of the coatings in alumina. In summary, it appears that all positions for the alumina GLAD device could work. Furthermore, the values are comparable to those of silica (Table 7). While the use of this laser does not permit the determination of the threshold for the LMJ, it is reasonable to hypothesize that the laser resistance will be similar to or slightly lower than silica.

To conclude, alumina demonstrates promising optical properties, making it suitable for use in both ambient air and contaminated vacuum conditions. However, work is still required to improve the transmittance of the multilayer, and it is essential to perform more LIDT tests on the CEA testbed, which exhibits characteristics analogous to those of the LMJ and was previously utilized to ascertain the threshold of silica in Chapter 3.

4. Summary of Chapter 5

In this chapter, an analysis of the deposition of alumina at glancing angles ranging from 68° to 82° was conducted. We found that the optimal deposition angle is ± 76° in order to yield the maximum birefringence of 0.053.

We evaluated the number of layers required for the QWP design by characterizing a bilayer composed of the chosen anisotropic layer and an isotropic layer to avoid broadening and to increase the mechanical strength. The optimized design consists of seven anisotropic-isotropic layer pairs and an antireflective layer (α ± 86°) as top layer.

A uniform retardance of the QWP coating was calculated at 88 nm with the ellipsometric model and measured at 89 nm using the birefringence mapper. The transmittance of the coating is 91.6 % and losses were estimated at 2.4 %. Improving the performance of the last antireflective layer could reduce losses.

The retardance of the QWP has been followed for a period exceeding a year, during which time the QWP has demonstrated stability, exhibiting an increase of only 3 %. Alumina demonstrates promising laser damage resistance properties in all environments (ambient air, vacuum, and contaminated vacuum). The retardance and the transmittance are, also, not impacted by the vacuum.

This all-alumina GLAD wave plate appears to be a promising solution for optical smoothing in the LMJ.

General conclusion and perspectives

1. Conclusion

The Laser MégaJoule (LMJ) requires smoothing the intensity profile of its 176 beams. Polarization Smoothing (PS) is the optical smoothing technique that has been selected. To achieve this objective, it is proposed to generate circular polarizations with opposite handedness which, given the linear polarization of the LMJ, requires the fabrication of quarter-wave plates (QWPs). Among the various techniques allowing the creation of QWPs, GLancing Angle Deposition (GLAD) technique, using Serial BiDeposition (SBD) substrate motion algorithm was selected. In addition to high laser resistance, several challenges were identified for the GLAD component including: achieving specified retardance and transmittance values, as well as, good spatial homogeneity. The LMJ application imposed the materials of the coating to maintain long-term stability in the LMJ environment. The objective of the thesis was to assess the feasibility of a full-scale GLAD coating providing consistent optical performance for the optical smoothing of the LMJ laser beams.

First, a comprehensive study of a state-of-the-art sample from the Laboratory for Laser Energetics (LLE) enabled us to understand how such an optical function can be achieved. We studied an existing multilayer GLAD QWP in silica that was designed and fabricated by S. MacNally *et al.* A uniform retardance was measured. The silica matrix was found hydroxylated, however, accelerating the aging of the silica QPWs by exposing them to a 70 °C and 60 % relative humidity (RH), seemed to stabilize the retardance and decreased its sensitivity to moisture. Transmission was too low but that should be reduced thanks to refinement on the last antireflective layer. Coating's laser resistance demonstrated threshold significantly lower than the bare substrate's threshold and below the LMJ specification. Coating defects are believed to be responsible for damage initiation. Considering a location in a contaminated vacuum, the impact of Dimethyl Phthalate (DMP) was characterized. It affects the optical properties by lowering the transmission and the laser resistance. The impact appeared to be irreversible or a very slow desorption over time. Based on these findings, the location in ambient air was determined to be the optimal choice.

Next, I have investigated the creation of a new design using alumina. Alumina was partly selected for its chemical inertness and higher refractive index. The analysis of the deposition of single anisotropic layers of alumina at glancing angles was conducted. We found that the optimal deposition angle is ± 76° in order to yield the maximum birefringence. The optimized design consists of seven anisotropic-isotropic layer pairs and an antireflective layer as top layer. This less-layer design is an improvement compared to silica. The QWP coating demonstrated stable and uniform retardance over a year. However, the transmittance of the coating is too low and more work is required on the last AR layer. Changing the environment did not seem to impact the laser damage resistance, the retardance and the transmittance of the alumina QWPs. This all-alumina GLAD wave plate appears to be a promising solution for the optical smoothing in the LMJ in all environments.

Table 11 presents a comparison of the main properties of both silica and alumina QWPs based on my work. We demonstrated the feasibility of GLAD QWP coatings that would ensure consistent optical performance for the optical smoothing of LMJ laser beams. Silica QWPs would be preferred for use in ambient air after being artificially aged. The newly developed alumina QWPs have shown great potential in all of the tested environments. The transmission of both samples can be enhanced by implementing improvements to the AR layer.

Table 11. Comparison of the main properties of the silica QWP and the alumina QWP

	Silica QWP	**Alumina QWP**
QWP homogeneous function	🙂 100-mm diameter sample	🙂 50-mm diameter sample
Retardance stability over time	With accelerated aging 🙂	🙂
Transmission	😐	😐
Proposed location (based on laser damage resistance tests)	- Ambient air	- Ambient air - Vacuum - Contaminated vacuum

2. Future works and perspectives

In the short term, the following complementary works could be considered.

For silica samples:

- The climate chamber exposure appears to be a viable solution. However, further testing is required to ascertain the laser resistance of these aged samples.
- As discussed in Chapter 4.2, understanding the variation of retardance between ambient air and nitrogen, could allow for the separation of mesoporosity and microporosity using the CompleteEASE model.

For alumina samples:

- It is essential to study the impact of the contamination on the retardance and the transmittance on the alumina QWPs.
- As previously indicated in Chapter 5.3, further characterizations are necessary on the testbed ELAN, which exhibits parameters analogous to those of the LMJ.
- Improving the last AR layer for the alumina QWP may be achieved by selecting a smaller deposition angle, as observed with the evolution of the curves presented in Figure 73 (Chapter 5.1).

In the longer term, for the fabrication of larger optics, several key factors must be considered. First, size and weight will impact the holder and its movements during the SBD process. Additionally, the source size and the e-beam pattern may need modifications. Indeed, the uniformity depends on the size of the plume and source-to-substrate distance. Sectioning the deposition process by coating through an aperture and translating it might help [13], [20], [24], [124]. A rotary cylindrical sputtering target might be an approach to test.

Additionally, this device has the potential for adaptation to **other applications**. The LMJ contains two quartz components with a half-wave plate optical function. The latter components are after the pre-amplifier module (MPA) which is annotated in (2), in Figure 4. These are in a controlled ambient air environment and operate in transmission at 1053 nm. The design can be adapted to alumina, with the number of layers adjusted as needed. The vacuum window and the main debris shield (Figure 7), have a sol gel antireflective layer. This AR layer could be produced using a GLAD coating in alumina, which would have the advantage of being non-sensitive to contamination. These components could be utilized in other high-power laser facilities or equipped in polarization-manipulating devices.

Appendices

Appendix 1. Relation between the Jones matrix and the elements of the Mueller matrix [125] . With * referring to conjugated complex.

m11 = $\frac{1}{2}\left(\left|J_{pp}\right|^2 + \left|J_{sp}\right|^2 + \left|J_{ps}\right|^2 + \left|J_{ss}\right|^2\right)$

m12 = $\frac{1}{2}\left(\left|J_{pp}\right|^2 - \left|J_{sp}\right|^2 - \left|J_{ps}\right|^2 + \left|J_{ss}\right|^2\right)$

m13 = $Re(J_{pp}J_{ps}^{*} + J_{sp}J_{ss}^{*})$

m14 = $Im(J_{pp}J_{ps}^{*} + J_{sp}J_{ss}^{*})$

m21 = $\frac{1}{2}\left(\left|J_{pp}\right|^2 - \left|J_{sp}\right|^2 + \left|J_{ps}\right|^2 - \left|J_{ss}\right|^2\right)$

m22 = $\frac{1}{2}\left(\left|J_{pp}\right|^2 - \left|J_{sp}\right|^2 - \left|J_{ps}\right|^2 + \left|J_{ss}\right|^2\right)$

m23 = $Re(J_{pp}J_{ps}^{*} - J_{sp}J_{ss}^{*})$

m24 = $Im(J_{pp}J_{ps}^{*} - J_{sp}J_{ss}^{*})$

m31 = $Re(J_{pp}J_{sp}^{*} + J_{ps}J_{ss}^{*})$

m32 = $Re(J_{pp}J_{sp}^{*} - J_{ps}J_{ss}^{*})$

m33 = $Re(J_{pp}J_{ss}^{*} + J_{ps}J_{sp}^{*})$

m34 = $Im(J_{pp}J_{ss}^{*} - J_{ps}J_{sp}^{*})$

m41 = $-Im(J_{pp}J_{sp}^{*} + J_{ps}J_{ss}^{*})$

m42 = $-Im(J_{pp}J_{sp}^{*} - J_{ps}J_{ss}^{*})$

m43 = $-Im(J_{pp}J_{ss}^{*} + J_{ps}J_{sp}^{*})$

m44 = $Re(J_{pp}J_{ss}^{*} - J_{ps}J_{sp}^{*})$

Appendix 2. Schematic of the bench of the CEA: ELAN, used for the determination of LIDT of the silica QWP coatings [126].

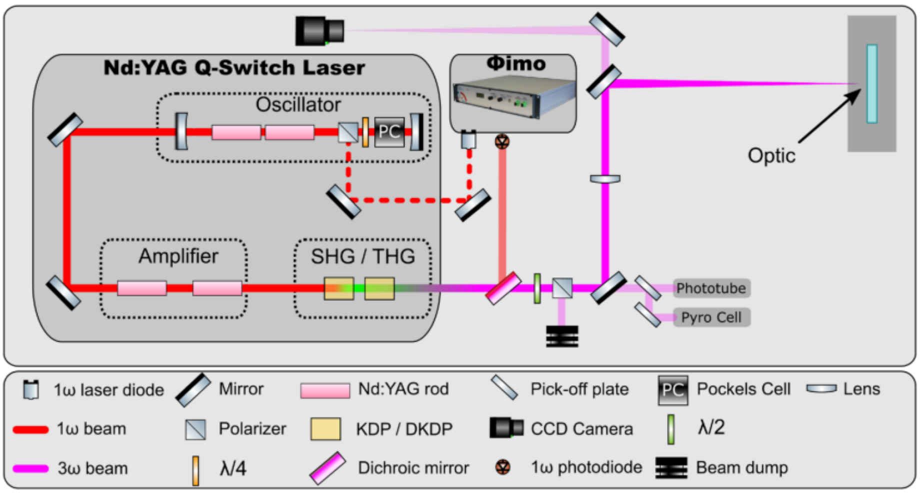

Appendix 3. Schematic of the bench at the Fresnel Institute used for the determination of LIDT of silica and alumina coatings in contaminated environment.

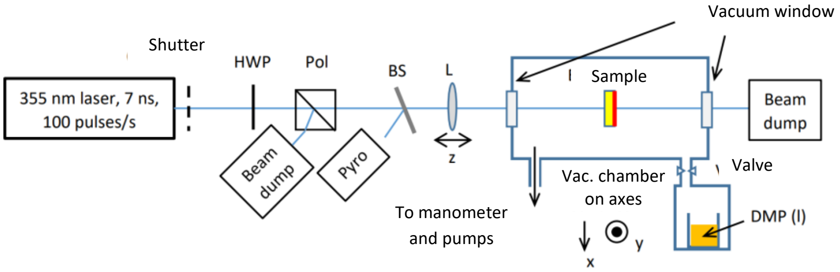

Appendix 4. Measured Mueller matrix elements by the ellipsometer for the multilayer QWP; before climate chamber (full line) and after 14 days in the climate chamber (dashed line), for three azimuthal orientations (0°, 45° and 90°).

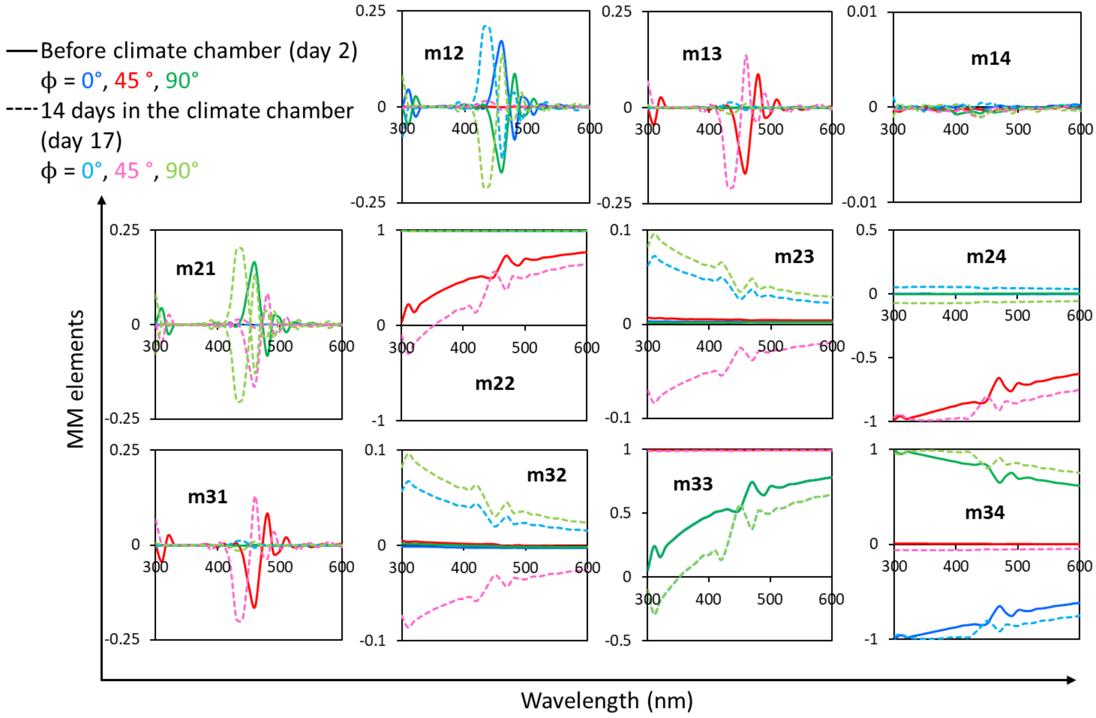

Glossary

AR	AntiReflective
ABEMA	Anisotropic Bruggeman Effective Medium Approximation
BEMA	Bruggeman Effective Medium Approximation
BM	Birefringence Mapper
B	Birefringent
CC	Climate Chamber
DMP	DiMethyl Phthalate
D-T	Deuterium-Tritium
EMA	Effective Medium Approximation
EM	ElectroMagnetic
FTIR	Fourier Transform InfraRed spectroscopy
GLAD	GLancing Angle Deposition
GD-OES	Glow Discharge Optical Emission Spectrometry
ICF	Inertial Confinement Fusion
IR	InfraRed
I	Isotropic
LEH	Laser Entrance Hole
LLE	Laboratory for Laser Energetics
LMJ	Laser MégaJoule
LIDT	Laser Induced Damage Threshold
MM	Mueller Matrix
MSE	Mean Squared Error
ns	nanosecond
PETG	PolyEthylene Terephthalate Glycol
ps	picosecond
PVD	Physical Vapor Deposition
QWP	Quarter Wave Plate
Ref	Reference
RH	Relative Humidity
SBD	Serial Bideposition
SEM	Scanning Electron Microscope
SSD	Smoothing by Spectral Dispersion
SZM	Structure Zone Model
UV	UltraViolet
WP	Wave Plate

References

[1] R. Betti *et al.*, “Inertial-confinement fusion with lasers,” *Nat. Phys.*, vol. 12, no. 5, Art. no. 5, May 2016, doi: 10.1038/nphys3736.

[2] O. A. Hurricane *et al.*, “Present understanding of ignition and gain using indirect-drive inertial confinement fusion target designs on the U.S. National Ignition Facility,” Feb. 11, 2025.

[3] J. G. Moreau *et al.*, “Stimulated Brillouin scattering dependence on polarization state, speckle shape, and polarization smoothing implementation,” *Phys. Plasmas*, vol. 32, no. 3, p. 032102, Mar. 2025, doi: 10.1063/5.0238070.

[4] M. Duluc, “Étude des propriétés statistiques d’une tache focale laser lissée et de leur influence sur la rétrodiffusion brillouin stimulée,” PhD Thesis, Bordeaux, 2019.

[5] N. Bonod *et al.*, “Full-silica metamaterial wave plate for high-intensity UV lasers,” *Optica*, vol. 8, no. 11, pp. 1372–1379, Nov. 2021, doi: 10.1364/OPTICA.434662.

[6] 405nm, “What is laser speckle?,” 405nm.com. Accessed: Sept. 22, 2025. [Online]. Available: https://405nm.com/laser-speckle/

[7] R. H. Lehmberg *et al.*, “Theory of induced spatial incoherence,” *J. Appl. Phys.*, vol. 62, no. 7, pp. 2680–2701, Oct. 1987, doi: 10.1063/1.339419.

[8] S. Skupsky *et al.*, “Improved laser-beam uniformity using the angular dispersion of frequency-modulated light,” *J. Appl. Phys.*, vol. 66, no. 8, pp. 3456–3462, Oct. 1989, doi: 10.1063/1.344101.

[9] E. M. Epperlein, “LLE Review (Quarterly Report, October-December 1990, Volume 45),” Univ. of Rochester, NY (United States), DOE/DP/40200-149-Vol.45, Mar. 1991. doi: 10.2172/6094362.

[10] E. Lefebvre *et al.*, “Reduction of laser self-focusing in plasma by polarization smoothing,” *Phys. Plasmas*, vol. 5, no. 7, pp. 2701–2705, July 1998, doi: 10.1063/1.872957.

[11] J. E. Rothenberg, “Polarization smoothing for the National Ignition Facility,” in *Third International Conference on Solid State Lasers for Application to Inertial Confinement Fusion*, SPIE, July 1999, pp. 980–990. doi: 10.1117/12.354250.

[12] S. Grosjean, “Étude de l’endommagement laser UV des optiques en silice dans le cadre du LMJ : rôles du nombre de tirs et de la polarisation,” PhD Thesis, Aix-Marseille, 2024.

[13] J. B. Oliver *et al.*, “Electron-beam–deposited distributed polarization rotator for high-power laser applications,” *Opt. Express*, vol. 22, no. 20, pp. 23883–23896, Oct. 2014, doi: 10.1364/OE.22.023883.

[14] S. N. Dixit *et al.*, “Random phase plates for beam smoothing on the Nova laser,” *Appl. Opt.*, vol. 32, no. 14, pp. 2543–2554, May 1993, doi: 10.1364/AO.32.002543.

[15] K. L. Marshall *et al.*, “Multiparameter laser performance characterization of liquid crystals for polarization control devices in the nanosecond regime,” *Sci. Rep.*, vol. 12, no. 1, p. 10969, June 2022, doi: 10.1038/s41598-022-14974-5.

[16] Y. Wang *et al.*, “Polarization smoothing for single beam by a nematic liquid crystal scrambler,” *Appl. Opt.*, vol. 56, no. 29, pp. 8087–8091, Oct. 2017, doi: 10.1364/AO.56.008087.

[17] H. Huang *et al.*, “Modeling of transverse stimulated Raman scattering in KDP/DKDP in large-aperture plates suitable for polarization control,” *High Power Laser Sci. Eng.*, vol. 11, p. e54, Jan. 2023, doi: 10.1017/hpl.2023.43.

[18] N. Bonod *et al.*, “Linear-to-circular polarization conversion with full-silica meta-optics to reduce nonlinear effects in high-energy lasers,” *Nat. Commun.*, vol. 14, no. 1, p. 5383, Sept. 2023, doi: 10.1038/s41467-023-40709-9.

[19] T. Z. Kosc *et al.*, “Angular dependence of the transverse Raman scattering in KDP and DKDP in geometries suitable for beam polarization control,” *Opt. Express*, vol. 30, no. 8, pp. 12918–12928, Apr. 2022, doi: 10.1364/OE.448388.

[20] T. Motohiro *et al.*, “Thin film retardation plate by oblique deposition,” *Appl. Opt.*, vol. 28, no. 13, pp. 2466–2482, July 1989, doi: 10.1364/AO.28.002466.

[21] S.-H. Woo *et al.*, “Optical Anisotropy of TiO2 and MgF2 Thin Films Prepared by Glancing Angle Deposition,” *J.-KOREAN Phys. Soc.*, vol. 49, no. 5, p. 2136, 2006.

[22] X. Xiao *et al.*, “Structure and optical properties of Nb2O5 sculptured thin films by glancing angle deposition,” *Appl. Surf. Sci.*, vol. 255, no. 5, Part 1, pp. 2192–2195, Dec. 2008, doi: 10.1016/j.apsusc.2008.07.071.

[23] Y. J. Park *et al.*, “Linear polarization-discriminatory state inverter fabricated by oblique angle deposition,” *Opt. Express*, vol. 17, no. 13, pp. 10535–10541, June 2009, doi: 10.1364/OE.17.010535.

[24] J. B. Oliver *et al.*, “Glancing-angle–deposited magnesium oxide films for high-fluence applications,” *Opt. Mater. Express*, vol. 6, no. 7, pp. 2291–2303, July 2016, doi: 10.1364/OME.6.002291.

[25] L. Grinevičiūtė *et al.*, “Highly Resistant Zero-Order Waveplates Based on All-Silica Multilayer Coatings,” *Phys. Status Solidi A*, vol. 214, no. 12, p. 1770175, 2017, doi: 10.1002/pssa.201770175.

[26] S. MacNally *et al.*, “Glancing-angle-deposited silica films for ultraviolet wave plates,” *Appl. Opt.*, vol. 59, no. 5, Art. no. 5, Feb. 2020, doi: 10.1364/AO.59.00A155.

[27] T. Tolenis *et al.*, “Sculptured anti-reflection coatings for high power lasers,” *Opt. Mater. Express*, vol. 7, no. 4, Art. no. 4, Apr. 2017, doi: 10.1364/OME.7.001249.

[28] D. Franta *et al.*, “Wide spectral range optical characterization of tantalum pentoxide (Ta_2O_5) films by the universal dispersion model,” *Opt. Mater. Express*, vol. 15, no. 4, pp. 903–919, Apr. 2025, doi: 10.1364/OME.550708.

[29] A. Jolivet *et al.*, “Structural, optical, and electrical properties of TiO2 thin films deposited by ALD: Impact of the substrate, the deposited thickness and the deposition temperature,” *Appl. Surf. Sci.*, vol. 608, p. 155214, Jan. 2023, doi: 10.1016/j.apsusc.2022.155214.

[30] S. Sarkar *et al.*, “Hybridized Guided-Mode Resonances via Colloidal Plasmonic Self-Assembled Grating,” *ACS Appl. Mater. Interfaces*, vol. 11, no. 14, pp. 13752–13760, Apr. 2019, doi: 10.1021/acsami.8b20535.

[31] L. V. R. Marcos *et al.*, “Self-consistent optical constants of MgF_2, LaF_3, and CeF_3 films,” *Opt. Mater. Express*, vol. 7, no. 3, pp. 989–1006, Mar. 2017, doi: 10.1364/OME.7.000989.

[32] D. Franta *et al.*, “Universal dispersion model for characterization of optical thin films over wide spectral range: Application to magnesium fluoride,” *Appl. Surf. Sci.*, vol. 421, pp. 424–429, Nov. 2017, doi: 10.1016/j.apsusc.2016.09.149.

[33] R. A. Synowicki *et al.*, “Optical properties of bulk c-ZrO2, c-MgO and a-As2S3 determined by variable angle spectroscopic ellipsometry,” *Thin Solid Films*, vol. 455–456, pp. 248–255, May 2004, doi: 10.1016/j.tsf.2004.02.028.

[34] L. Gao *et al.*, “Exploitation of multiple incidences spectrometric measurements for thin film reverse engineering,” *Opt. Express*, vol. 20, no. 14, pp. 15734–15751, July 2012, doi: 10.1364/OE.20.015734.

[35] J. Kischkat *et al.*, “Mid-infrared optical properties of thin films of aluminum oxide, titanium dioxide, silicon dioxide, aluminum nitride, and silicon nitride,” *Appl. Opt.*, vol. 51, no. 28, pp. 6789–6798, Oct. 2012, doi: 10.1364/AO.51.006789.

[36] R. Boidin *et al.*, “Pulsed laser deposited alumina thin films,” *Ceram. Int.*, vol. 42, no. 1, Part B, pp. 1177–1182, Jan. 2016, doi: 10.1016/j.ceramint.2015.09.048.

[37] T. Amotchkina *et al.*, “Characterization of e-beam evaporated Ge, YbF_3, ZnS, and LaF_3 thin films for laser-oriented coatings,” *Appl. Opt.*, vol. 59, no. 5, pp. A40–A47, Feb. 2020, doi: 10.1364/AO.59.000A40.

[38] I. Hodgkinson *et al.*, “Serial bideposition of anisotropic thin films with enhanced linear birefringence,” *Appl. Opt.*, vol. 38, no. 16, Art. no. 16, June 1999, doi: 10.1364/AO.38.003621.

[39] L. Xu *et al.*, “Theoretical and experimental study on the electronic structure and optical absorption properties of P-doped TiO2,” *Appl. Surf. Sci.*, vol. 256, no. 9, pp. 2668–2671, Feb. 2010, doi: 10.1016/j.apsusc.2009.11.046.

[40] “Dimethyl Phthalate | C10H10O4 | CID 8554 - PubChem.” Accessed: May 27, 2025. [Online]. Available: https://pubchem.ncbi.nlm.nih.gov/compound/Dimethyl-phthalate#section=Use-and-Manufacturing

[41] T. Andjelković *et al.*, “Phthalates leaching from plastic food and pharmaceutical contact materials by FTIR and GC-MS,” *Environ. Sci. Pollut. Res.*, vol. 28, no. 24, pp. 31380–31390, June 2021, doi: 10.1007/s11356-021-12724-0.

[42] Y. Wu *et al.*, “Simple Method To Measure the Vapor Pressure of Phthalates and Their Alternatives,” *Environ. Sci. Technol.*, vol. 50, no. 18, pp. 10082–10088, Sept. 2016, doi: 10.1021/acs.est.6b02643.

[43] I. Thomas *et al.*, “Method for reducing the effect of environmental contamination of solgel optical coatings,” *PROCEEDINGS OF SPIE*, Lawrence Livermore National Laboratory, p. 11, July 23, 1999.

[44] M. Mireles *et al.*, “Distinctive molecular configuration of nanostructured silica deposited at a glancing angle,” *Opt. Express*, vol. 33, no. 4, Art. no. 4, Feb. 2025, doi: 10.1364/OE.551290.

[45] S. Rubeck *et al.*, “Effect of accelerated hydrothermal aging on the durability of Si-based dielectric thin films,” *Microelectron. Eng.*, vol. 264, p. 111858, Aug. 2022, doi: 10.1016/j.mee.2022.111858.

[46] R. Thielsch *et al.*, “Mechanical stress and thermal-elastic properties of oxide coatings for use in the deep-ultraviolet spectral region,” *Appl. Opt.*, vol. 41, no. 16, Art. no. 16, June 2002, doi: 10.1364/AO.41.003211.

[47] S. Dong *et al.*, “Interface and defects engineering for multilayer laser coatings,” *Prog. Surf. Sci.*, vol. 97, no. 3, Art. no. 3, Aug. 2022, doi: 10.1016/j.progsurf.2022.100663.

[48] X. Li *et al.*, “The stability of sol–gel silica coatings in vacuum with organic contaminants,” *J. Sol-Gel Sci. Technol.*, vol. 59, no. 3, Art. no. 3, Sept. 2011, doi: 10.1007/s10971-011-2524-6.

[49] R. H. Doremus, “Alumina,” in *Ceramic and Glass Materials*, Springer, Boston, MA, 2008, pp. 1–26. doi: 10.1007/978-0-387-73362-3_1.

[50] K. S. Kang *et al.*, “Reliable high temperature, high humidity flexible thin film encapsulation using Al2O3/MgO nanolaminates for flexible OLEDs,” *Nano Res.*, vol. 13, no. 10, pp. 2716–2725, Oct. 2020, doi: 10.1007/s12274-020-2915-5.

[51] Y.-Q. Yang *et al.*, “Realization of Thin Film Encapsulation by Atomic Layer Deposition of Al2O3 at Low Temperature,” *J. Phys. Chem. C*, vol. 117, no. 39, pp. 20308–20312, Oct. 2013, doi: 10.1021/jp406738h.

[52] J.-H. Choi *et al.*, “Highly conformal SiO2/Al2O3 nanolaminate gas-diffusion barriers for large-area flexible electronics applications,” *Nanotechnology*, vol. 21, no. 47, p. 475203, Oct. 2010, doi: 10.1088/0957-4484/21/47/475203.

[53] F. Nehm *et al.*, “Breakdown and Protection of ALD Moisture Barrier Thin Films,” *ACS Appl. Mater. Interfaces*, vol. 7, no. 40, pp. 22121–22127, Oct. 2015, doi: 10.1021/acsami.5b06891.

[54] F. Berghmans *et al.*, “An introduction to radiation effects on optical components and fiber optic sensors,” in *Optical waveguide sensing and imaging*, Springer, 2008, pp. 127–165.

[55] C. Giuliano, “Laser-induced damage in transparent dielectrics: The relationship between surface damage and surface plasmas,” *IEEE J. Quantum Electron.*, vol. 8, no. 9, pp. 749–754, 1972, doi: 10.1109/JQE.1972.1077285.

[56] S. Papernov *et al.*, “Testing asymmetry in plasma-ball growth seeded by a nanoscale absorbing defect embedded in a SiO2 thin-film matrix subjected to UV pulsed-laser radiation,” *J. Appl. Phys.*, vol. 104, no. 6, p. 063101, Sept. 2008, doi: 10.1063/1.2980054.

[57] T. I. Suratwala, *Materials Science and Technology of Optical Fabrication*. John Wiley & Sons, 2018.

[58] F. Bonneau *et al.*, “Study of UV laser interaction with gold nanoparticles embedded in silica,” *Appl. Phys. B*, vol. 75, no. 8, pp. 803–815, Dec. 2002, doi: 10.1007/s00340-002-1049-7.

[59] K. Bien-Aimé *et al.*, “Impact of storage induced outgassing organic contamination on laser induced damage of silica optics at 351 nm,” *Opt. Express*, vol. 17, no. 21, pp. 18703–18713, Oct. 2009, doi: 10.1364/OE.17.018703.

[60] K. Bien-Aimé *et al.*, “Laser induced damage of fused silica polished optics due to a droplet forming organic contaminant,” *Appl. Opt.*, vol. 48, no. 12, pp. 2228–2235, Apr. 2009, doi: 10.1364/AO.48.002228.

[61] H. Bercegol *et al.*, “Filamentation and surface damage in fused silica with single-mode and multi-mode pulses,” in *Laser-Induced Damage in Optical Materials: 2005*, SPIE, Feb. 2006, pp. 613–620. doi: 10.1117/12.638480.

[62] N. Kaiser *et al.*, *Optical Interference Coatings*. Springer, 2013.

[63] C. Marsal, “Couches nanostructurées élaborées par dépôt en incidence oblique pour l’optimisation des performances optiques dans le visible et le proche infrarouge,” PhD Thesis, Poitiers, 2022.

[64] M. Losurdo *et al.*, *Ellipsometry at the Nanoscale*, vol. 268. Springer, 2013.

[65] M. Born *et al.*, *Principles of Optics: 60th Anniversary Edition*, 7th ed. Cambridge: Cambridge University Press, 2019. doi: 10.1017/9781108769914.

[66] C. Langlois, “Reconnaissance des minéraux,” 2007.

[67] “Ellipsoïde des indices [Minéralogie].” Accessed: Jan. 05, 2026. [Online]. Available: https://minweb.univ-lille.fr/res/cours.eWeb/co/chap04_01.html

[68] “Biréfringence,” *Wikipédia*. Nov. 18, 2024. Accessed: Aug. 08, 2025. [Online]. Available: https://fr.wikipedia.org/w/index.php?title=Bir%C3%A9fringence&oldid=220401593

[69] “Calcite,” Geology is the Way. Accessed: Aug. 13, 2025. [Online]. Available: https://geologyistheway.com/minerals/calcite/

[70] "Double Refraction | Harvard Natural Sciences Lecture Demonstrations." Accessed: Aug. 11, 2025. [Online]. Available: https://sciencedemonstrations.fas.harvard.edu/presentations/double-refraction

[71] O. Arteaga *et al.*, "Pseudopolar decomposition of the Jones and Mueller–Jones exponential polarization matrices," *J. Opt. Soc. Am. A*, vol. 26, no. 4, pp. 783–793, 2009.

[72] R. M. A. Azzam, "Propagation of partially polarized light through anisotropic media with or without depolarization: a differential 4× 4 matrix calculus," *J. Opt. Soc. Am.*, vol. 68, no. 12, pp. 1756–1767, 1978.

[73] V. M. Shalaev, Ed., *Optical Properties of Nanostructured Random Media*, 1st ed. Springer Berlin, Heidelberg, 2002.

[74] L. A. Golovan *et al.*, "Optical properties of porous-system-based nanocomposites," *Phys.-Uspekhi*, vol. 50, no. 6, p. 595, June 2007, doi: 10.1070/PU2007v050n06ABEH006257.

[75] J. C. M. Garnett, "VII. Colours in metal glasses, in metallic films, and in metallic solutions.—II," *Philos. Trans. R. Soc. Lond. Ser. Contain. Pap. Math. Phys. Character*, vol. 205, no. 387–401, pp. 237–288, Jan. 1906, doi: 10.1098/rsta.1906.0007.

[76] R. W. Boyd *et al.*, "Nonlinear optical properties of nanocomposite materials," *Pure Appl. Opt. J. Eur. Opt. Soc. Part A*, vol. 5, no. 5, p. 505, Sept. 1996, doi: 10.1088/0963-9659/5/5/005.

[77] D. a. G. Bruggeman, "Berechnung verschiedener physikalischer Konstanten von heterogenen Substanzen. I. Dielektrizitätskonstanten und Leitfähigkeiten der Mischkörper aus isotropen Substanzen," *Ann. Phys.*, vol. 416, no. 7, pp. 636–664, 1935, doi: 10.1002/andp.19354160705.

[78] D. Schmidt *et al.*, "Anisotropic Bruggeman effective medium approaches for slanted columnar thin films," *J. Appl. Phys.*, vol. 114, no. 8, p. 083510, Aug. 2013, doi: 10.1063/1.4819240.

[79] P. Kfoury *et al.*, "Orientation and shape distributions effective medium theory (OSDEMT): Applications in plasmonic nanocomposites," *Optik*, vol. 312, p. 171972, Sept. 2024, doi: 10.1016/j.ijleo.2024.171972.

[80] S. Berthier, *Optique des milieux composites*. Polytechnica, 1999.

[81] M. Karakaya, "Characterization of molecular beam epitaxially grown CdTe layers over GaAs by spectroscopic ellipsometry," PhD Thesis, Turkey, 2014.

[82] F. Bernoux *et al.*, "Ellipsométrie Théorie," *Tech. Ing.*, 2003, doi: 10.51257/a-v1-r6490.

[83] B. A. Movchan *et al.*, "Structure and properties of thick condensates of nickel, titanium, tungsten, aluminum oxides, and zirconium dioxide in vacuum," *Fiz Met. Met. 1969*.

[84] J. A. Thornton, "The microstructure of sputter-deposited coatings," *J. Vac. Sci. Technol. A*, vol. 4, no. 6, Art. no. 6, Nov. 1986, doi: 10.1116/1.573628.

[85] M. M. Hawkeye *et al.*, *Glancing angle deposition of thin films: engineering the nanoscale*. John Wiley & Sons, 2014.

[86] I. Hodgkinson *et al.*, “Vacuum deposition of biaxial films with surface-aligned principal axes and large birefringence Δn,” in *Optical Interference Coatings*, Optica Publishing Group, 1998, p. TuA.3. doi: 10.1364/OIC.1998.TuA.3.

[87] M. Mireles *et al.*, “Direct-write laser-assisted patterning of form birefringence in wave plates fabricated by glancing-angle deposition,” *Optica*, vol. 10, no. 6, pp. 657–662, June 2023, doi: 10.1364/OPTICA.487263.

[88] J. Barbillat *et al.*, “Raman spectrometry,” *Tech. Ing.*, 2019.

[89] A. Brunet-Bruneau *et al.*, “Infrared ellipsometry study of evaporated SiO2 films: Matrix densification, porosity, water sorption,” *J. Appl. Phys.*, vol. 82, no. 3, Art. no. 3, Aug. 1997, doi: 10.1063/1.365906.

[90] A. Brunet-Bruneau *et al.*, “Change of TO and LO mode frequency of evaporated SiO2 films during aging in air,” *J. Appl. Phys.*, vol. 87, no. 10, pp. 7303–7309, May 2000, doi: 10.1063/1.372984.

[91] R. Dorka *et al.*, “Investigation of SiO2 layers by glow discharge optical emission spectroscopy including layer thickness determination by an optical interference effect,” *J. Anal. At. Spectrom.*, vol. 15, no. 7, pp. 873–876, 2000, doi: 10.1039/B000905I.

[92] Z. Wĕiss *et al.*, “Elemental depth profiling of coated and surface-modified materials by GD-OES: hard coatings on cutting tools,” *Thin Solid Films*, vol. 308–309, pp. 382–388, Oct. 1997, doi: 10.1016/S0040-6090(97)00586-5.

[93] V. F. G. Soares *et al.*, “Structure, mechanical properties and oxidation resistance of iso and non-iso architected TiN/Cr multilayers coatings deposited by magnetron sputtering,” *Mater. Res.*, vol. 24, p. e20200315, 2021, doi: 10.1590/1980-5373-MR-2020-0315.

[94] K. Scherer *et al.*, “Optical and mechanical characterization of evaporated SiO_2 layers. Long-term evolution,” *Appl. Opt.*, vol. 35, no. 25, Art. no. 25, Sept. 1996, doi: 10.1364/AO.35.005067.

[95] W. A. Pliskin, “Comparison of properties of dielectric films deposited by various methods,” *J. Vac. Sci. Technol.*, vol. 14, no. 5, Art. no. 5, Sept. 1977, doi: 10.1116/1.569413.

[96] A. Alessi *et al.*, “Raman and IR investigation of silica nanoparticles structure,” *J. Non-Cryst. Solids*, vol. 362, pp. 20–24, Feb. 2013, doi: 10.1016/j.jnoncrysol.2012.11.006.

[97] H. J. Lee *et al.*, “The mechanical properties of the SiOC(H) composite thin films with a low dielectric constant,” *Surf. Coat. Technol.*, vol. 171, no. 1, Art. no. 1, July 2003, doi: 10.1016/S0257-8972(03)00289-5.

[98] B. B. Burton *et al.*, “SiO2 Atomic Layer Deposition Using Tris(dimethylamino)silane and Hydrogen Peroxide Studied by in Situ Transmission FTIR Spectroscopy,” *J. Phys. Chem. C*, vol. 113, no. 19, pp. 8249–8257, May 2009, doi: 10.1021/jp806638e.

[99] H. F. W. Dekkers *et al.*, "Infrared molar absorption coefficient of H2O stretching modes in SiO2," *Thin Solid Films*, vol. 542, pp. 8–13, Sept. 2013, doi: 10.1016/j.tsf.2013.05.151.

[100] L. T. Zhuravlev, "The surface chemistry of amorphous silica. Zhuravlev model," *Colloids Surf. Physicochem. Eng. Asp.*, vol. 173, no. 1, pp. 1–38, Nov. 2000, doi: 10.1016/S0927-7757(00)00556-2.

[101] A. E. Geissberger *et al.*, "Raman studies of vitreous SiO2 versus fictive temperature," *Phys. Rev. B*, vol. 28, no. 6, pp. 3266–3271, Sept. 1983, doi: 10.1103/PhysRevB.28.3266.

[102] R. J. Hemley *et al.*, "Raman Spectroscopy of SiO2 Glass at High Pressure," *Phys. Rev. Lett.*, vol. 57, no. 6, pp. 747–750, Aug. 1986, doi: 10.1103/PhysRevLett.57.747.

[103] H. Liu *et al.*, "Vibrational spectroscopy analysis of silica and silicate glass networks," *J. Am. Ceram. Soc.*, vol. 105, no. 4, pp. 2355–2384, 2022, doi: 10.1111/jace.18206.

[104] S. K. Sharma *et al.*, "Raman investigation of ring configurations in vitreous silica," *Nature*, vol. 292, no. 5819, pp. 140–141, July 1981, doi: 10.1038/292140a0.

[105] C. Smith *et al.*, "Ellipsometric modeling of serially bi-deposited glancing-angle-deposition coatings," *Appl. Opt.*, vol. 59, no. 5, Art. no. 5, Feb. 2020, doi: 10.1364/AO.59.000A26.

[106] S. Bertet *et al.*, "All-alumina quarter-wave plate coatings fabricated by glancing angle deposition using serial bideposition," *Appl. Surf. Sci.*, vol. 710, p. 163957, Nov. 2025, doi: 10.1016/j.apsusc.2025.163957.

[107] L. Lamaignère *et al.*, "Parametric study of laser-induced surface damage density measurements: Toward reproducibility," *J. Appl. Phys.*, vol. 107, no. 2, p. 023105, Jan. 2010, doi: 10.1063/1.3282704.

[108] B. C. Stuart, "Laser-Induced Damage in Dielectrics with Nanosecond to Subpicosecond Pulses," *Phys. Rev. Lett.*, vol. 74, no. 12, pp. 2248–2251, 1995, doi: 10.1103/PhysRevLett.74.2248.

[109] J. Osswald *et al.*, "FTIR spectroscopic study on liquid silica solutions and nanoscale particle size determination," *J. Mater. Sci.*, vol. 41, no. 5, pp. 1335–1339, Mar. 2006, doi: 10.1007/s10853-006-7327-8.

[110] G. Nageswari *et al.*, "Molecular analyses using FT-IR, FT-Raman and UV spectral investigation; quantum chemical calculations of dimethyl phthalate," *J. Mol. Struct.*, vol. 1195, pp. 331–343, Nov. 2019, doi: 10.1016/j.molstruc.2019.05.098.

[111] L. Ji *et al.*, "Density functional theory and surface-enhanced Raman spectroscopy studies on endocrine-disrupting chemical, dimethyl phthalate," *Vib. Spectrosc.*, vol. 79, pp. 44–51, July 2015, doi: 10.1016/j.vibspec.2015.05.002.

[112] M.-C. Wu *et al.*, "Ag/SiO2 surface-enhanced Raman scattering substrate for plasticizer detection," *Jpn. J. Appl. Phys.*, vol. 57, no. 4S, p. 04FM07, Mar. 2018, doi: 10.7567/JJAP.57.04FM07.

[113] T. Takenaka *et al.*, "Raman Spectra of Benzene, Ethyl Benzene and Dimethyl Phthalate Solubilized in Aqueous Solutions of Surface-Active Agents," *Bull. Inst. Chem. Res. Kyoto Univ.*, vol. 53, no. 2, pp. 173–179, 1975.

[114] Q. Ma *et al.*, "Spectral shift response of optical whispering-gallery modes due to water vapor adsorption and desorption," *Meas. Sci. Technol.*, vol. 21, no. 11, p. 115206, Oct. 2010, doi: 10.1088/0957-0233/21/11/115206.

[115] H. Zhao *et al.*, "Research on the degradation mechanism of dimethyl phthalate in drinking water by strong ionization discharge," *Plasma Sci. Technol.*, vol. 20, no. 3, p. 035503, Jan. 2018, doi: 10.1088/2058-6272/aa97d1.

[116] G. J. Young, "Interaction of water vapor with silica surfaces," *J. Colloid Sci.*, vol. 13, no. 1, pp. 67–85, Feb. 1958, doi: 10.1016/0095-8522(58)90010-2.

[117] *ISO 9022-2:2015 Optics and photonics — Environmental test methods — Part 2: Cold, heat and humidity*, 2015.

[110] A. Soutenain *et al.*, "Long-term aging of SiO_2/HfO_2 PIAD-deposited Laser Mégajoule polarizer coatings," *Opt. Express*, vol. 33, no. 20, pp. 43116–43127, Oct. 2025, doi: 10.1364/OE.564390.

[119] A. Soutenain, "Impact des propriétés physico-chimiques des revêtements SiO2/HfO2 sur les performances optiques et le vieillissement des composants des lasers de puissance," PhD Thesis, Limoges, 2024.

[120] S. L. Warring *et al.*, "Surficial Siloxane-to-Silanol Interconversion during Room-Temperature Hydration/Dehydration of Amorphous Silica Films Observed by ATR-IR and TIR-Raman Spectroscopy," *Langmuir*, vol. 32, no. 6, pp. 1568–1576, Feb. 2016, doi: 10.1021/acs.langmuir.5b04506.

[121] T. Takamura *et al.*, "Infrared characteristic bands of highly dispersed silica," *Kolloid-Z. Z. Für Polym.*, vol. 195, no. 1, pp. 12–16, Mar. 1964, doi: 10.1007/BF01500878.

[122] M. Stehlik *et al.*, "Investigation of damage initiation and damage growth of dielectric mirrors under 351-nm, nanosecond laser pulses," in *Laser-Induced Damage in Optical Materials 2024*, SPIE, Dec. 2024, p. PC1319003. doi: 10.1117/12.3032761.

[123] C. J. Stolz *et al.*, "Evaluation of alumina and silica coating materials for the NIF final turning mirrors," in *Laser-Induced Damage in Optical Materials 2021*, SPIE, Dec. 2021, pp. 57–66. doi: 10.1117/12.2598577.

[124] J. B. Oliver *et al.*, "Development of a Glancing-Angle–Deposited Distributed Polarization Rotator," in *Advanced Photonics 2015 (2015), paper NS4B.1*, Optica Publishing Group, June 2015, p. NS4B.1. doi: 10.1364/NOMA.2015.NS4B.1.

[125] T. Brakstad *et al.*, "Dispersion of polarization coupling, localized and collective plasmon modes in a metallic photonic crystal mapped by Mueller Matrix Ellipsometry," *Opt. Express*, vol. 23, no. 17, pp. 22800–22815, Aug. 2015, doi: 10.1364/OE.23.022800.

[126] C. Bouyer *et al.*, “Phase-modulated injection seeding for testing laser-induced damage of thick optics with Q-switch lasers,” *Rev. Sci. Instrum.*, vol. 96, no. 6, p. 063004, June 2025, doi: 10.1063/5.0257868.

Abstract

To improve the laser-matter interaction, it is necessary to homogenize the intensity of the focal spots of the LMJ laser beams. One possible approach is Polarization Smoothing (PS), which can be implemented in the LMJ using 351 nm quarter-wave plates (inducing a phase difference of $\pi/2$). The purpose of this PhD thesis is to study the feasibility of a quarter-wave plate coating, deposited using the GLancing Angle Deposition (GLAD) technique, which would ensure consistent optical performance in terms of retardance, transmission, and laser-induced damage resistance. Two approaches have been explored: one involving a silica coating, the other one an alumina coating. Both types of coatings are multilayers, alternating anisotropic and isotropic layers, that achieve the desired retardance at the LMJ wavelength. The silica coatings consist of either 21 or 31 layers, while the alumina coatings are reduced to 15 layers. Thorough physicochemical analyzes, ellipsometric modeling, and a study of the impact of ambient environments (air, vacuum, and DMP organic contamination) on component performance were conducted. Silica coatings are suitable for ambient air use after an artificial aging that has been elaborated during this thesis work. Alumina coatings, developed for this work, exhibit great potential in all tested environments.

Key words: GLAD, Thin film, Quarter-wave plate, Optical smoothing, Anisotropy, Ellipsometry, Silica, Alumina

Etude des revêtements GLAD pour le lissage optique des lasers de puissance

Résumé

Afin d'améliorer l'interaction laser-matière, il est nécessaire d'homogénéiser l'intensité des taches focales des faisceaux du LMJ. Une des voies possibles est le lissage par double polarisation, qui peut être mis en place sur le LMJ, par l'usage de lames quart d'onde à 351 nm (induisant un déphasage de $\pi/2$). L'objectif de la thèse est d'étudier la faisabilité d'un revêtement de fonction optique quart d'onde, déposé avec la technique GLancing Angle Deposition (GLAD), qui garantirait des performances optiques constantes de retard, de transmission et de résistance au flux laser. Deux approches ont été explorées : l'une utilise un dépôt en silice, et l'autre, un dépôt en alumine. Les dépôts sont des multicouches, alternant des couches anisotropes et isotropes, permettant d'obtenir le retard souhaité à la longueur d'onde du LMJ. Les dépôts sont composés de 21 ou 31 couches pour le composant en silice, et peuvent être réduits à seulement 15 couches pour le composant en alumine. Des analyses physico-chimiques approfondies, des modélisations ellipsométriques, ainsi qu'une étude de l'influence de l'environnement ambiant (air, vide, pollution organique-DMP) sur les performances des composants ont été réalisées. Les dépôts en silice ont des performances optiques adaptées à une utilisation à l'air ambiant, moyennant une étape de vieillissement artificiel, dont l'élaboration s'est réalisée lors de cette thèse. Les dépôts en alumine, développés dans ce travail, présentent un fort potentiel dans tous les environnements.

Mots clés : GLAD, Couches minces, Lame quart d'onde, Lissage optique, Anisotropie, Ellipsométrie, Silice, Alumine